공학박사 학위논문

Fabrication of Nanostructure via Localized Focused Ion Beam-Chemical Vapor Deposition (FIB-CVD)

국소영역 집속이온빔 화학기상증착을 이용한 나노구조물 제작

2018 년 2 월

서울대학교 대학원

기계항공공학부

이 강 인

국소영역 집속이온빔 화학기상증착을 이용한 나노구조물 제작

Fabrication of nanostructure via localized focused ion beam-chemical vapor deposition(FIB-CVD)

지도교수 안 성 훈

이 논문을 공학박사 학위논문으로 제출함

2017 년 10 월

서울대학교 대학원

기계항공공학부

이 강 인

이강인의 공학박사 학위논문을 인준함

2017 년 11 월

위 원 장 : 박 희갑

부위원장 : 안 성훈

위 원 : 차 석 원

위 원 : 강 도 연

위 원 : 천 두 만

Abstract

Fabrication of Nanostructure via Localized Focused Ion Beam-Chemical Vapor Deposition (FIB-CVD)

Kang-In Lee

Department of Mechanical and Aerospace Engineering

The Graduate School

Seoul National University

In the time since focused ion beam-induced chemical vapor deposition (FIB-CVD) process was first introduced in the 1980s, it has become widely used not only for repair of semi-conductors, but also in the fabrication of various micro/nano structure devices including electronic components, sensors/actuators, and even nanomaterials. As the usability of the process increases, many researchers have studied the fundamentals of the process to improve process performances such as precision, efficiency, and purity of the deposited material. Despite these studies, however, due to the sensitive process parameters, and the complicated deposition mechanisms interacting with ions, electrons, precursor gases and a solid substrate,

the fundamental mechanism of the process has not been yet clearly defined. The FIB-CVD process is a process in which some components of a precursor compound are deposited on the substrate by chemical reaction of the precursor gas. In general, temperature condition is an important factor in determining the chemical reaction rate. The temperature is inevitably one of the crucial process parameters. Previous studies on the effect of temperature on the process have been reported on the deposition characteristics according to the temperature of the precursor reservoir and the substrate temperature. However, even though the temperature of the precursor gas is directly related to the chemical reaction, little research on this has been done. This is mainly due to the fact that it is difficult to construct an experiment in which only the temperature of the precursor gas is used as a dependent variable at a gas injection system (GIS) responsible for supplying precursor gas.

In this study, the effect of precursor gas temperature on FIB-CVD process was investigated from the viewpoint of deposition rate. In order to experimentally explore the influence of the gas temperature, a GIS which can independently control the precursor gas temperature was developed. With the developed GIS, the effect of the precursor gas temperature on the deposition rate of $C_{14}H_{10}$ precursor in FIB-CVD process was investigated. In addition, to theoretically understand the experimental results, a numerical model of the FIB-CVD deposition mechanism was developed. In order to solve the difficulties of the distance calculation between the deposition surface evolved in real time and the emitted electrons, which was difficult to consider in the conventional numerical methods, the Hausdorff distance concept generally used for object recognition in image processing was firstly

adapted. Finally, the shape memory (SMA) based micro bending actuator was fabricated by modifying the deflection behavior of a SMA linear actuator with a localized carbon block deposited via FIB-CVD process using optimized precursor gas temperature.

Keywords: Focused ion beam, Precursor gas temperature, Micro actuator, Shape memory alloy, Chemical vapor deposition, Hausdorff distance

Student Number: 2014-31040

Table of Contents

List of Figures

List of Tables

Chapter 1. Introduction

1.1 Technologies for micro/nanoscale structure prototyping

Advances in science and manufacturing have complemented and evolved. In recent years, manufacturing techniques have been emerging that enable the accuracy and complexity of disassembling and assembling DNA-sized objects beyond the molecular size of the animal's basic unit. These technologies enable the convergence of nanotechnologies in various fields such as physics, chemistry, biology, electronics, and communication, creating new fields that have never existed and once again providing the basic power for the development of science and technology. Focused ion beam (FIB) machining is based on field emission technology and is used to focus particles with high energy. It is known that the system was first developed in 1970's [1]. As can be seen in Figure 1, FIB technology is suitable for machining features from several micrometers to tens of nanometers in scale. Another advantage is that additive machining can be done on one platform in addition to subtractive machining if auxiliary devices are used to supply precursor gas. Through this complex machining, complicated shapes including undercut as well as general three-dimensional shapes can be machined, where is enable to be utilized in various fields where nanoscale machining is required.

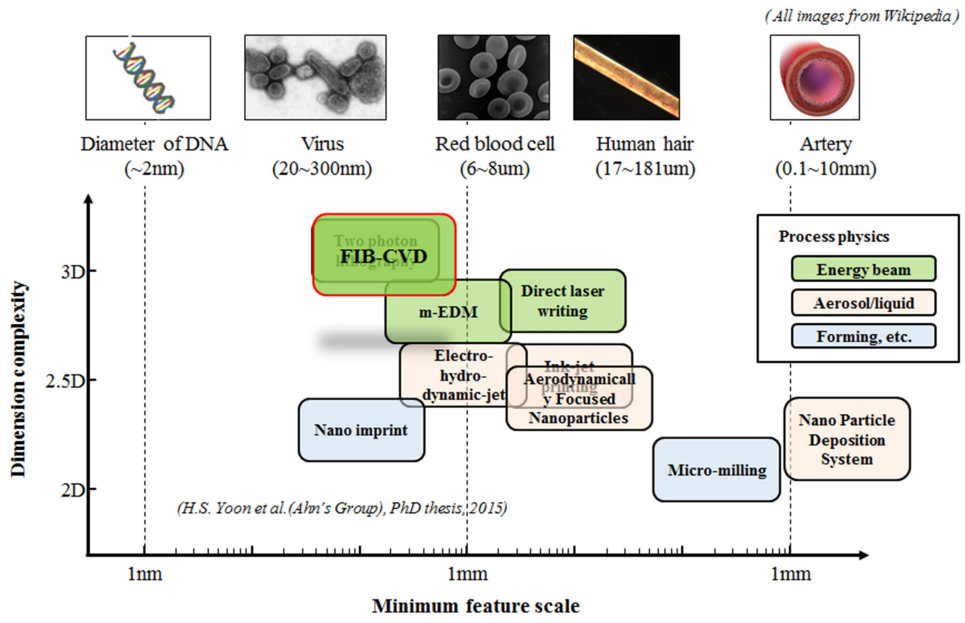

Figure 1 Performance map of micro/nanoscale prototyping

1.2 Focused ion beam induced chemical vapor deposition

The FIB-based chemical vapor deposition process (FIB-CVD) is an additive process for depositing non-metal materials such as carbon and SiO_2 as well as metals such as tungsten and platinum using FIB. Electron beam induced CVD has a similar deposition mechanism but differs in accuracy and growth rate because the source of the energy that decomposes the precursor molecule is ion rather than electron. In general, the deposition rate of FIB-CVD is known to be more efficient [2, 3]. Figure 2 illustrates the behavior of the precursor gas molecules on the substrate surface used in FIB-CVD process. The red particle in the middle represents the ion particle emitted from the ion gun. The ions are focused to the target point under control by the electrostatic lens. The precursor gas molecules pass through the space of the vacuum chamber and reach the target surface of the

substrate from the nozzle tip of a gas injection system (GIS), which feeds precursor gas molecules to the substrate in the vacuum chamber. Some of the precursor molecules are adsorbed on the surface, and the adsorbed precursor molecules become the source material of the deposition. Some adsorbed precursor molecules are decomposed by the FIB, and some are desorbed naturally, and also move by diffusion on a surface.

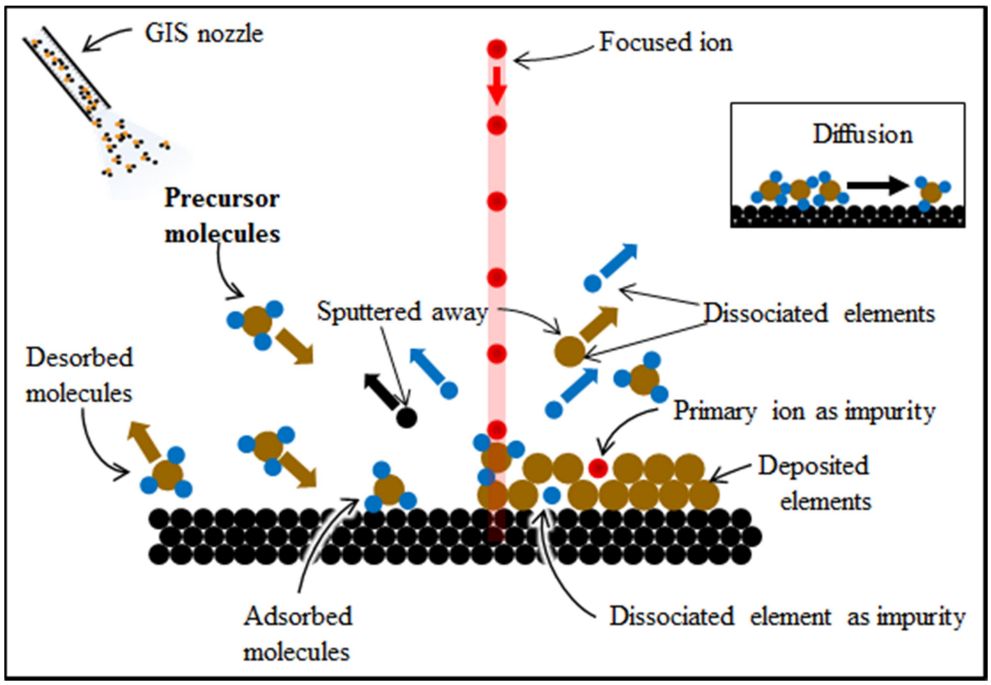

Figure 2 Behavior of precursor molecules on a substrate

Various kinds of precursor materials are utilized in FIB-CVD process such as organometallic, carbonyl, and alkoxide depending on the deposit material. The process mechanism has not been clearly defined yet, but it is explained by widely accepted two models. First, there is an analytic method based on the collision cascade model. This model explains that the nuclei of the substrate material are excited by the incident ion energy and the energy is transferred to the atoms on the surface by the collision cascade of the nuclei collision, and the atoms cause

decomposition of the precursor molecules in adjacent itself. This model consequently leads to explains that the stopping power of the incident ion is closely related to the deposition rate and is relatively less related to the generated secondary electron (SE) [4]. On the other hand, the other model explains that secondary electrons generated by incident ions are closely related to deposition [5]. This method can also explain the mechanism of deposition by primary electrons. Introduced ions are scattered inside the substrate material and generate electrons from the atom of the substrate material. Some of the electrons emitted to the surface evoke the decomposition of the precursor molecule. The non-volatile part of the decomposed component is deposited on the surface and the volatile part is pumped out of the chamber. Figure 4 is a schematic depiction of the trajectories of an incident ion and the generated SE.

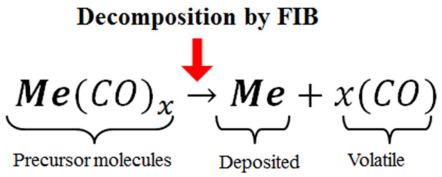

Figure 3 Example of chemical reaction induced by FIB

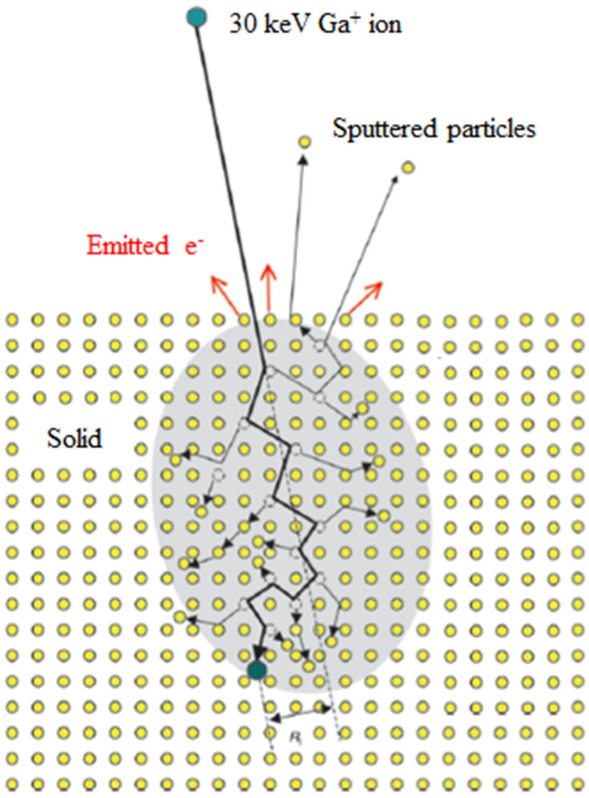

Figure 4 Schematic illustration of trajectories of incident ion and generated electrons[6]

The researches related to the FIB-CVD processes can be roughly classified into three categories; the research on process mechanism itself, the research on process performance such as deposition rate and topography, and the research on manufacturing functional structure using process. The FIB-CVD process is a complicated process that involves incident ion, solid, electron and molecule in the high vacuum chamber of 10^{-7} ~ 10^{-4} Torr. Therefore, it is difficult to measure the phenomenon and it is not easy to verify accurate process mechanism. Utke et al. have extended their research on electron beam induced deposition (EBID) to FIB-CVD and have made many research achievements on primary ion (electron), secondary electron, precursor gas molecule dynamics, etc. and published studies on

various applications using this process [7-10]. Winkler et al. studied the topography variation of the deposition according to the scan direction in the EBID process through experiments and simulations [11], C.S. Kim et al. (Ahn's Group) demonstrated the relationship between step parameter, growth rate and topography in carbon pillar laminates using FIB-CVD process [12], Yonggi Fu et al. Conducted experiments on beam spot size, beam current dwell time, and refresh time for the dependency of the deposition characteristics [13]. In addition, several reviews have been introduced on the subject of process [14-16].

Studies on the fabrication of functional devices using FIB milling and deposition have widely been carried out. Jaesam Sim et al. fabricated a tungsten nanowire-to-electrode structure using a FIB-CVD process to demonstrate the tungsten nanowire's resistance to humidity changes [17], Jiyung Chang et al. We have studied the fabrication of bimorph actuators using the thermal expansion difference between two materials by laminating carbon and tungsten layer by layer [18]. To improve the accuracy of μ-ECDM, Dengji Guo et al was deposited platinum microelectrode on a needle using a FIB-CVD process to improve accuracy [19].

Researches that explore and understand the mechanism itself have also been conducted by many researchers. Since the FIB-CVD process is similar to the EBID process in terms of the principle that a precursor molecule is dissociated into the energy of the emitted electron to be deposited. The study of modeling with reference to the interpretation of EBID has been generally carried out. The modeling method of CVD process using incident ions or electrons are divided into two categories: continuous model and discrete model. Continuous modeling

method defines deposition rate as differential equation and solution in steady state, and the discrete model includes the electron scattering in the modeling based on Monte Carlo method [20-22]. The continuum model basically analyzes the deposition mechanism by calculating the adsorption rate equation based on Langmuir adsorption as follows.

$$\frac{dN(t)}{dt} = sJ\left(1 - \frac{N(t)}{N_0}\right) - \frac{N(t)}{\tau_D} - \sigma N(t) f - D\left(\frac{\partial^2 N}{\partial r^2} + \frac{1}{r}\frac{\partial N}{\partial r}\right) \quad (1)$$

Where *N(t)* is the number of precursor molecules absorbed on the surface. The number of precursor molecules on the substrate is basically changed by the phenomenon that the molecule absorbed by the surface by physisorption or chemisorption is naturally desorbed or consumed by dissociation and the position is changed by diffusion. In order to solve this model, the sticking coefficient (s), the precursor gas flux (J), the residence time (τ_D), the dissociation cross section (σ), the ion or primary electron flux distribution (f) must be defined. These constants are generally regarded as unclear parameters and many researchers have defined them as specific values under certain conditions in their study [23, 24]. Numerical simulation of FIB-CVD using Monte Carlo method has been developed from EBID modeling. This is because the models have in common that the generation and emission of secondary electrons that cause deposition and the behavior of the precursor molecules adsorbed on the surface of the substrate are regarded as important phenomena in determining the results of the simulation. The phenomena that occur when an electron beam collides with a solid surface have been studied steadily since the early 20th century. A typical example of using this phenomenon is secondary electron detector (SED). It is a sensor that detects secondary electrons

and converts them to image signal, and is widely used as a typical imaging technology with nanoscale resolution. Based on these results, many simulations have been carried out to date to help understand the phenomena in EBID's atomic scale [25-29]. A simulation package called Transport of Ions in Matter (TRIM), stopping and Range of Ions in Matter (SRIM) developed by Ziegler et al. has been extensively used for the studies about deposition mechanism using ion scattering [30-32]. Recently, based on these results, the results of the simulation about the milling and deposition process using FIB process have been published. However, a clear understanding of the fundamental deposition mechanism caused by complex interactions between ions, electrons, solid surfaces, and precursor gas molecules is not yet sufficient [33-35].

1.3 Thesis motivation and framework

The FIB-CVD process is a useful tool for fabricating complex features with the accuracy of nanoscale. As described above, many researchers have been conducted on process parameters and fundamental mechanism of the process. Temperature is also a critical factor to change the kinematic characteristic of the precursor gas molecule as well as to control the interaction property between surface and molecule. Many researches have been therefore conducted on the influence of temperature on the FIB-CVD process. As the representative research related to temperature, there is a study on the heating temperature to evaporate the precursor [36, 37] and the effect of the substrate temperature [38-40]. Friedli et al. showed that heating the precursor reservoir subsequently increases the evaporation rate of a

precursor material, which increases the amount of precursor gas flux. The increase in precursor gas flux leads to a higher adsorption rate, which finally improves the deposition rate. Conversely, when the substrate temperature rises, the deposition rate increases or decreases depending on the material and deposition regime (mass transfer limited regime) due to changes in parameter values such as residence time, sticking coefficient, and diffusion coefficient [41]. However, there has been little research on the effect of the precursor gas temperature on the deposition characteristics directly. Increasing the reservoir temperature not only raises the temperature of a precursor gas but also increases the amount of gas flux Therefore, it is difficult to directly analyze the effect of precursor gas temperature on the process under the condition of changing the temperature of the reservoir. Instead, experiments on specific materials have been conducted in part on the effects of temperature on residence time, sticking coefficient, and diffusion coefficient on the adsorption rate of precursor molecules [42]. If the temperature of the precursor gas is increased while the temperature of the reservoir temperature is fixed, the sticking coefficient (s), the residence time (τ_D), and the diffusion coefficient (D) in Eq. (1) might be influenced. Sticking coefficient is known to be related to surface temperature, local pressure and kinetic energy of the impinging molecule [24]. The effect of very small precursor gas with high temperature on the surface thermalization for a short time is known to be insignificant. Therefore, it is expected that the effect on the sticking coefficient is dominated by the local pressure change due to the thermal energy of the precursor molecules rather than the surface temperature. In addition, in the previous studies, the sticking coefficient was assumed to be the unity value in most cases. Residence time is also known to

exponentially decrease with increasing surface temperature, but the effect on the temperature of the precursor gas is not clearly known. Therefore, this study intends to investigate the effect of precursor gas temperature on the deposition characteristics in FIB-CVD process and to make micro scale actuator based on the result. The study was carried out in the following order.

1. The gas injection system (GIS) that can control only nozzle temperature individually so that only temperature of precursor gas can be used as an experimental parameter in FIB-CVD process has been developed. The developed gas injection system is designed to control the temperature of the nozzle tip where the precursor gas is injected while the temperature of the reservoir and system is fixed. Experiments were conducted to investigate the effect of precursor gas temperature on the FIB-CVD process using the developed GIS. First, preliminary experiments were conducted to evaluate the feasibility of the developed GIS. Based on preliminary experiments, an experiment was conducted to analyze the effect of precursor temperature on the deposition characteristics.

2. Process modeling and simulation were conducted for the theoretical analysis of experimental results. Simulation included precursor gas transfer, primary ion and secondary electron scattering, and precursor molecule behavior on surface. In the implementation of the simulation, a new numerical method adapting image processing technology was proposed to effectively deal with the interaction between the precursor gas molecule on the evolving deposit surface and the emitted electron, which was a problem in previous studies. The results of the simulation are verified by comparing with the measured values by the

experiment.

3. Based on the FIB-CVD process, microscale shape memory alloy (SMA) based composite actuator was fabricated. Here, the FIB-CVD process was not utilized in the conventional manner, but was applied in a way that deposited the localized regions using the optimal precursor gas temperature. In addition, to verify the deformation characteristics of the actuator, microscale tensile tests were performed to compare the stiffness of SMA and SMA composite.

Chapter 2. System Integration

2.1 Development of a gas injection system (GIS)

2.1.1 Design

The gas injection system (GIS) in the FIB process has the role of supplying the precursor gas used as the deposition material and transporting the gas to the working area of the target substrate inside the FIB chamber. Precursor materials are present in solid powder, liquid, and gas form at room temperature. The materials used for deposition are mainly carbonyl, organometallic and alkoxide compounds, most of which are present in the solid state at room temperature. Therefore, an evaporation process of the precursor material is required for deposition. The amount of precursor gas flux used for deposition is very small, generally within the range of 10^{-3} ~ 10^{3} SCCM [2]. Since a small amount of flux is used, uniform temperature control of the GIS is essential so that the evaporated precursor gas does not recrystallize as it travels through the conduit in the system to the target location. If recrystallization occurs inside the system, the amount of gas flux is not uniformly supplied, which causes problems in the quality of the deposition, and in some cases, the internal channel is clogged. In addition, when the kind of precursor material is changed, the residual material becomes impurity and adversely affect the quality. The position of the nozzle from which the precursor gas is ejected is

also an important factor in determining the process quality. Normally, the nozzle is fixed at a height of several hundred μm from the surface. Therefore, it is necessary to pay considerable attention and move to a safe position when not working. The most important goal of the GIS developed in this study is to realize the function of controlling the temperature while maintaining the flow rate of the precursor gas constantly.

The GIS system is roughly divided into three parts: a reservoir unit, a gas control module, and an actuating module. The reservoir unit is where the precursor material evaporates. Precursor material is stored in a glass vial to prevent impurity and oxidation. Since the reservoir is the place where the precursor material is evaporated at high temperatures, critical mechanical and chemical properties must be taken into account in the material selection. First, the corrosion resistance must be high and high tensile stiffness should be obtained at high temperature. In addition, it must have a high thermal conductivity so that heat can be efficiently transferred to the precursor material. Generally, stainless steel (SUS316) or copper are used as reservoir material. A heater is installed outside the reservoir to indirectly heat the precursor material. It is important to note that flow direction is a crucial design consideration to make the gas flow from top to bottom in order to prevent the residue of the precursor gas. It is also important to minimize the dead volume through the shortest possible path.

The advantages and disadvantages of each part design by comparing the types of commercial GIS were shown in Table 1. Commercial GIS can be divided into three types based on external geometry. First, the GIS can be separated by the position of a reservoir where the precursor material is contained. In the case of a

multi-material GIS, a nozzle may be designed to be separated according to the material, or may be designed to use one nozzle for various kinds of precursor materials. Finally, depending on the type of actuator to move the nozzle, it can be divided into electric motor type and air operated cylinder type. In this study, the reservoir was designed using the external type for the location of reservoirs, the integrated type for the number of nozzle, and the air operating cylinder for the actuating the nozzle.

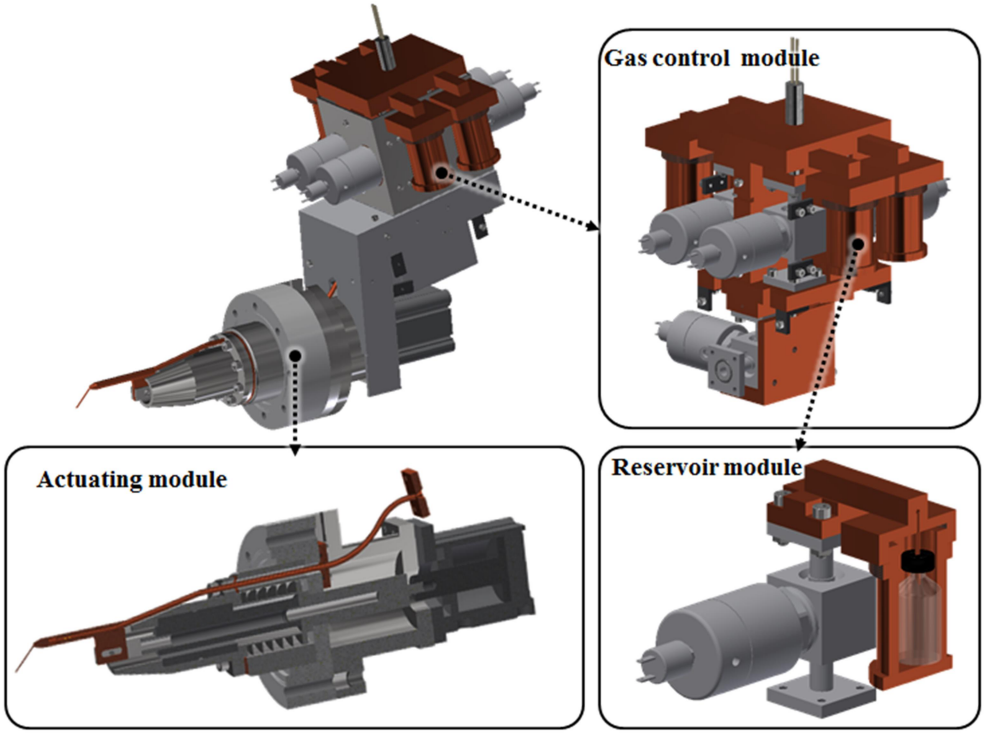

Figure 5 3D design of a gas injection system (GIS)

Table 1 Alternative designs for the GIS components

Internal	Strength	. Enable to make compact system . Reduce dead volume zone.
	Weakness	. Difficult to exchange or refill . Strongly need to concern high reaction resistivity
External	Strength	. Easy to exchange or refill the precursor materials . Easy configuration of Pneumatic, electric harness
	Weakness	. Relatively large dead volume zone . Strongly need to concern re-crystallization

(a) The position of the reservoir

Integrated	Strength	. Easy to produce mixed gas . Increase the repeatability of the nozzle position . Relatively simple pneumatic line
	Weakness	. The conduit contamination by using the different precursor material . Strongly need to concern purging system
Separated	Strength	. Conceptually protected from the contamination from the used gas
	Weakness	. Relatively complicated gas lines . Need extra unit to mix the two or more gases . Highly cost to get a repeatability

(b) Nozzle separation by material

Pneumatic	Strength	. Simple mechanism . Relatively cost effective
	Weakness	. low position repeatability (~ 10s um)
Motorized	Strength	. high position repeatability (+/- 1s um)
	Weakness	. Relatively complicated mechanism . need more space to set up

(c) Driven method of the actuator

A value is a basic device that controls the precursor gas flow. The GIS developed in this study is designed to supply precursor gas via two valves as shown in Figure 6. The first valve is a valve that controls the supply of gas to the reservoir. A valve at the bottom is a shut-down valve that manages the entire precursor gas. The available operating temperature of the valve should include the temperature range of the precursor gas to be used in the experiment and a valve with a sealant capable of operating at 10^{-9} Torr or higher should be selected to prevent vacuum leakage. In addition, materials that do not produce chemical reactions when contacted with precursor gases should be used. Use a Viton ring, gasket, or flange on the joint to prevent vacuum leakage in the entire path. Actuating module in Fig. 5 is a driving part that linearly moves the nozzle. It is important to design the vacuum leakage prevention of the drive part because it is mounted in the FIB chamber. In this development, vacuum leakage was prevented by using metal bellows and gasket, and it was designed to have a 30 mm stroke within a tolerance of 10 μm using a linear guide and a pneumatic cylinder. In general, the use of a electric motor as a drive for repetitive motion of a nozzle is not preferred except in certain cases, because the electromagnetic field disturbs the path of the precursor gas. The feature of the nozzle and its position are critical factors determining the quality of the flux distribution. There are a few considerable design factors for the optimized nozzle feature. First, material properties must be considered. Because the various types of precursor materials are ejected from the tip of the nozzle, the chemical resistance, i.e., the non-reactivity between the precursor gas and the nozzle material, is required. And, as well as gas-tightness, it is required to be mechanically firm enough to fix without any flipping by the gas pressure.

Moreover, the nozzle tip is closely located in the ionized particles, so that the non-magnetization property is also necessary. The length and the diameter of the nozzle is also crucial factor. They are directly related to the phase of the gas flow. Friedli V. et al. reported the effects of nozzle height, angle, inner diameter size and shape on deposition rate and topography in the EBID process [38].

Thermal management over the entire system is an important issue. The thermal energy supplied by external heating system must be low enough to avoid the premature thermal deposition through the gas flow conduit including manifold and tube, even the nozzle. And the temperature of the supply manifold must be at least the same degree with the reservoir to avoid the precursor condensation. In case of low-volatile solid or liquid precursor, the heating system onto the precursor reservoir is essential. And even for a gas type precursor, the heating system is very useful to produce a sufficient gas pressure. As a heating method, electrically resistive heating through the metal wire or metal film is generally used. As for heating cables, the materials which have a low resistive temperature coefficient such as Constantan, and Manganin are used. The metal wire is embedded in an insulating cladding. Especially inside of the vacuum chamber, only materials with low outgassing rate at elevated temperatures must be used. Often Kapton or special polymer is used as insulating material.

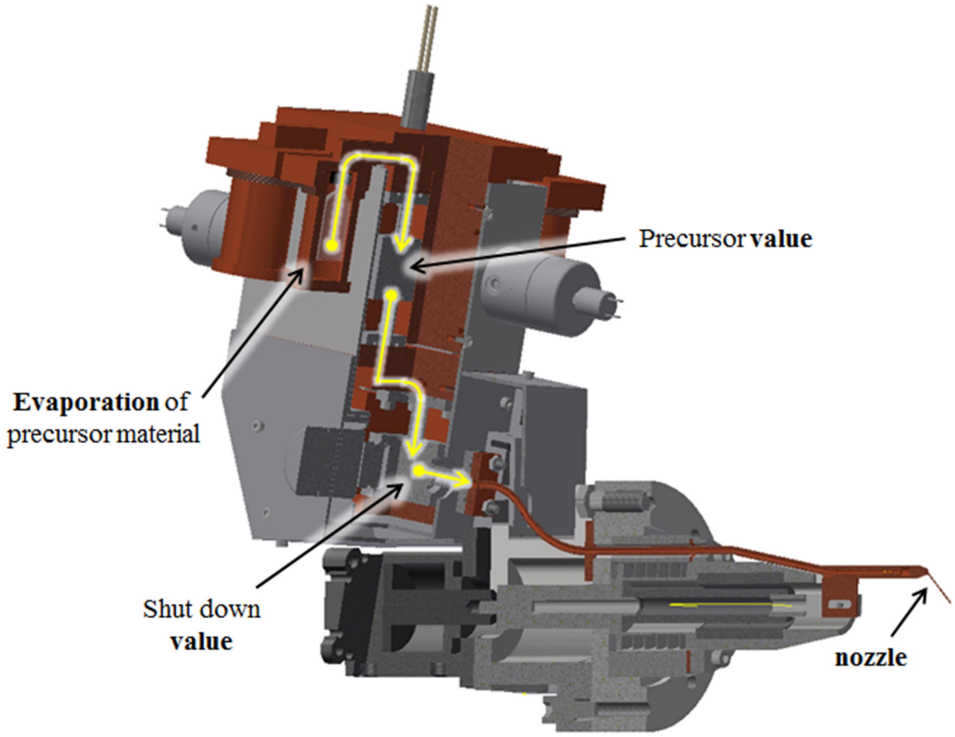

Figure 6 Schematic illustration of precursor gas flow

As well as outgassing property, the corrosion resistivity must be considered for the heaters. The heating jacket is a few bunches of heating wire and thermal sensor insulated by thermal jacket. For the stable thermal supply, thermal controllers with a variable analogue out are advisable [2]. Figure 7 shows an exploded view of the GIS. As shown in the figure, all of the paths through the precursor gas are made of copper to efficiently transfer the heat generated from the heater, and the PTFE plate is used as an insulation material inside the cover of the SUS material to prepare for heat loss and safety.

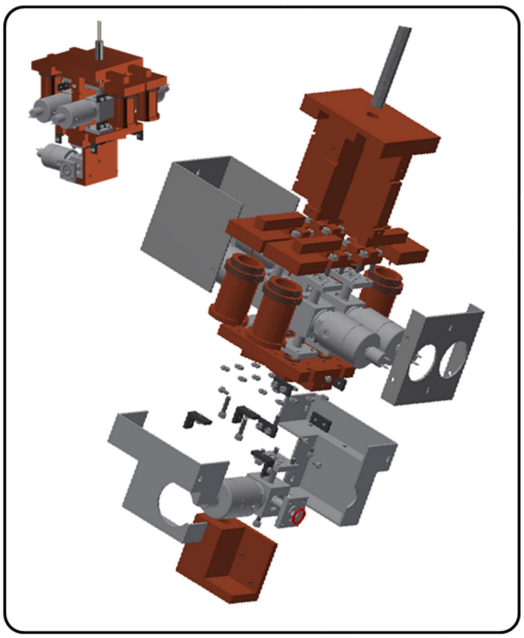

(a) Gas control module

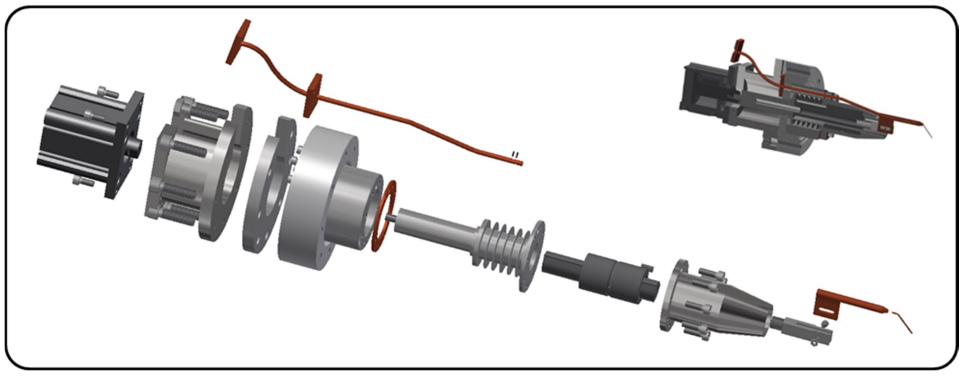

(b) Nozzle position control module

Figure 7 Assembly design of a gas injection system

Table 2 summarizes the sensors and actuators used in the developed GIS. The temperature and gas flow were controlled by using eight valves, seven heaters and pneumatic cylinders. In addition, six K-type T / C wires, pressure gauge and mass flow meter (MFM) were installed to acquire temperature, pressure and flux data. Since the flow rates used for deposition were only a few tens to several

hundred SCCMs, it was considered effective to reduce the dead volume by not using the pressure gauge and MFM rather than precisely controlling the flow with them. Figure 8 shows the thermal analysis results for the heater design to keep the system temperature uniform. For the boundary conditions, the room temperature was set at 20 °C, the reservoir temperature for evaporation was defined as 60 °C, and the cartridge heater for heating the entire system were defined as a surface heat source with 80 °C. From the experiment, it was found that the heat transfer was weak in the reservoir cap and valve inlet and outlet. These results can be confirmed by thermal analysis using FEM as shown in the Fig 8. Therefore, additional coil heaters were installed in the corresponding part for supplementation.

Table 2 Sensors and actuators/heaters for a GIS

No	Name	Purpose
1	Valve-air	On/off control for the air for the purge process
2	Valve#1	On/off control of precursor gas from reservoir #1
3	Valve#2	On/off control of precursor gas from reservoir #2
4	Valve#3	On/off control of precursor gas from reservoir #3
5	Valve#4	On/off control of precursor gas from reservoir #4
6	Regulator	To keep the precursor gas at the adequate pressure
7	Valve-purge	On/off control of the purged gas
8	Valve-gas	Shut down valve for the precursor gas
9	Valve-manual	Manual Shut off valve
10	Pneumatic Cylinder	Linear motion device for moving the position of the nozzle
11	Heater#1	To heat the reservoir #1
12	Heater#2	To heat the reservoir #2
13	Heater#3	To heat the reservoir #3
14	Heater#4	To heat the reservoir #4
15	Heater-manifold	To heat the manifold
16	Heater-jacket	To heat the precursor gas flowing into the chamber
17	T/Couple #1	Temperature measurement of reservoir #1
18	T/Couple #2	Temperature measurement of reservoir #2
19	T/Couple #3	Temperature measurement of reservoir #3
20	T/Couple #4	Temperature measurement of reservoir #4
21	T/Couple-Manifold	Temperature measurement of manifold
22	T/Couple-Jacket	Temperature measurement of the jacket heater
23	Pressure gauge	To measure the pressure the precursor gas
24	Mass Flow Meter	To measure the flux of the precursor gas

I / O diagrams for the H / W modules for heater, valve, and cylinder control and sensor modules that collect temperature and mass flow data are shown in Figure 9. Figure 10 shows the pneumatic diagram of the condensed air line for driving the value and cylinder. The final prototype of the developed GIS is shown in Fig 11. The assembly of the prototype required 178 parts including the actuator sensor and 73 fasteners.

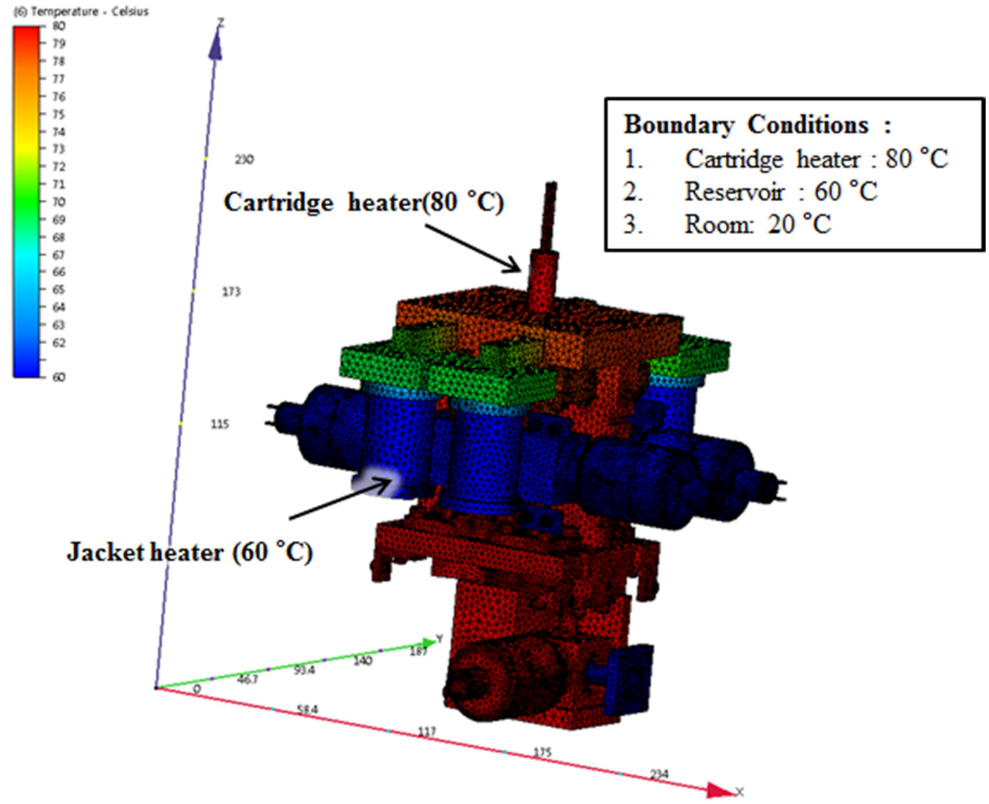

Figure 8 Thermal analysis of a GIS

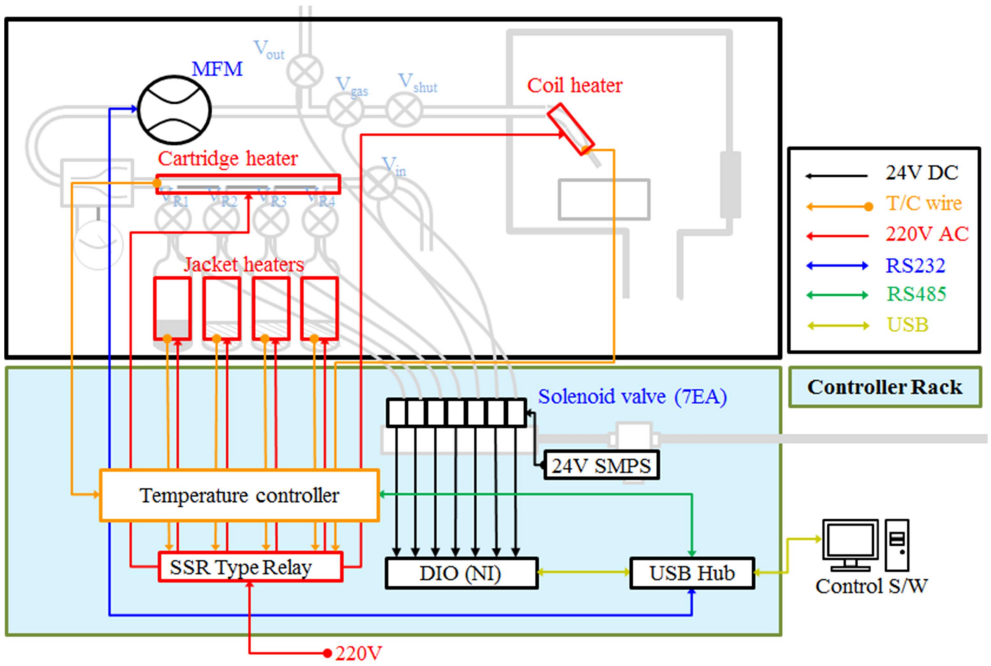

Figure 9 Schematic diagram of I/O for GIS controller

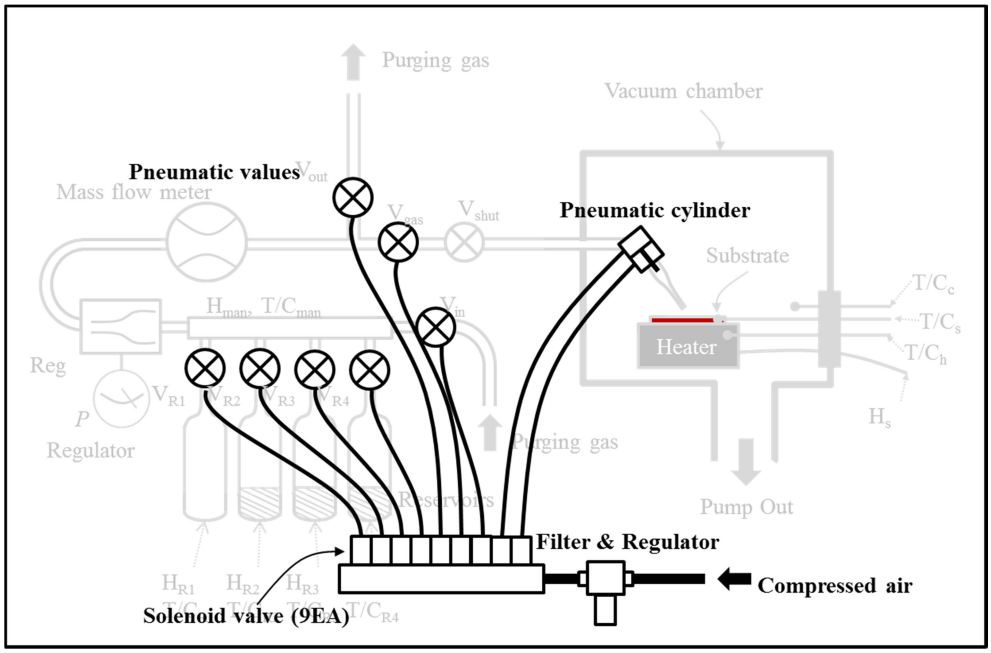

Figure 10 Schematic diagram of pneumatic actuator for GIS controller

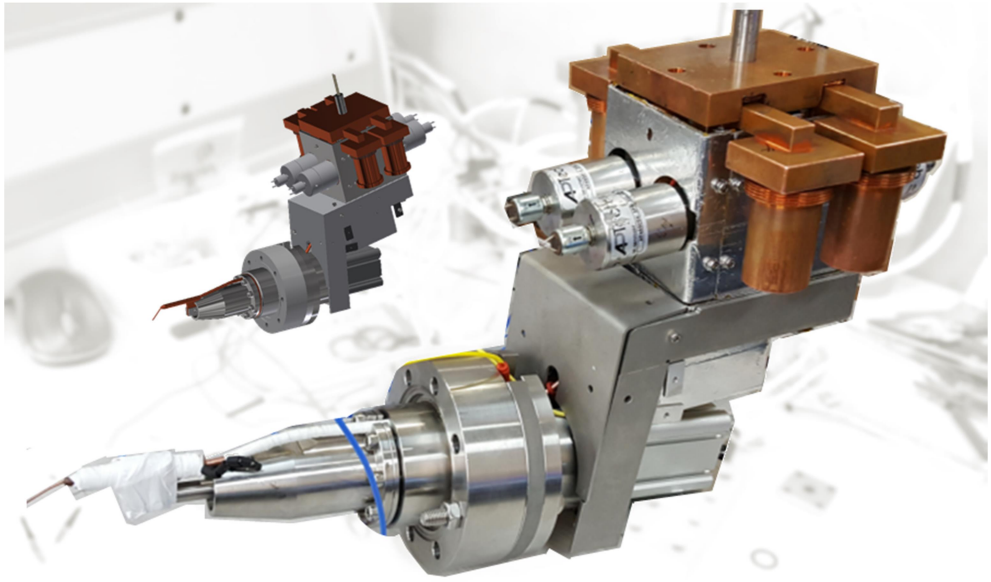

Figure 11 Prototype of developed gas injection system (GIS)

2.1.2 Evaluation

Prior to applying the developed GIS to the FIB-CVD process, the individual performance of the GIS must be evaluated first. To be installed in the FIB chamber, the GIS must be validated for several important issues. The most important issue is to check whether the temperature control can be uniformly applied to the whole system. Figure 12 shows the GIS connected to a vacuum chamber for evaluation. A total of five heaters were used for temperature control. The temperature written in red indicates the position where the temperature can be controlled with the heater, and the temperature written in blue indicates the temperature at the position indirectly heated by the heater. As shown in the figure, the temperature distributions of eight locations were evaluated. In the deposition experiment for evaluation, phenanthrene ($C_{14}H_{10}$), which is mainly used for carbon deposition, was used. Figure 13 is the picture showing the recrystallization problem of the

precursor gas in the preliminary experiment. As the temperature is not maintained uniformly and if there is a place where the temperature goes down below the evaporation temperature, the recrystallization problem of the gas occurs as shown in the figure. Additional silicon heaters were supplemented to solve the problem. $W(CO)_6$ deposition experiments were performed again with the addition of heaters. Figure 14 is a SEM image of deposits of $W(CO)_6$ deposited on a substrate. This deposition is not a deposition of tungsten by CVD but a deposition of $W(CO)_6$ gas evaporated in GIS recrystallized on a Si substrate in a vacuum chamber.

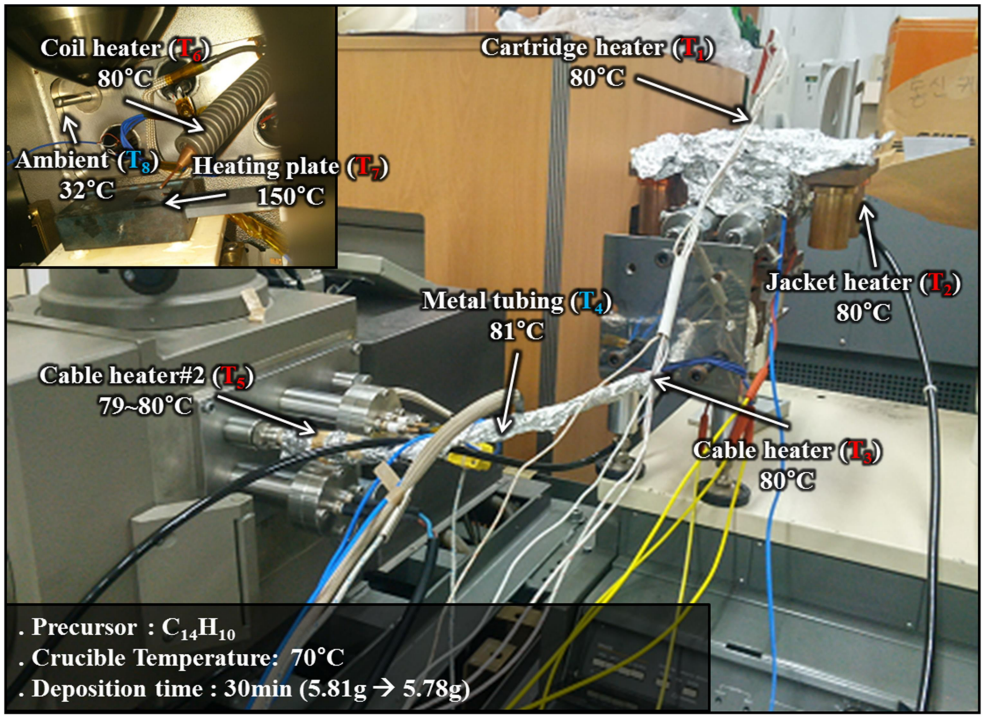

Figure 12 Setup for deposition experiment using developed GIS

Table 3 Temperature conditions of the GIS in deposition experiment

T/C	Range (°C)
T1 (Cartridge heater)	60~80
T2 (Valve)	60~80
T3 (Feedthrough)	65~85
T4 (Coil heater)	70~85
T5 (Copper pipe)	55~70
T6 (Jacket heater)	55~60
T7 (inside chamber)	30~33
T8 (System body)	60~70

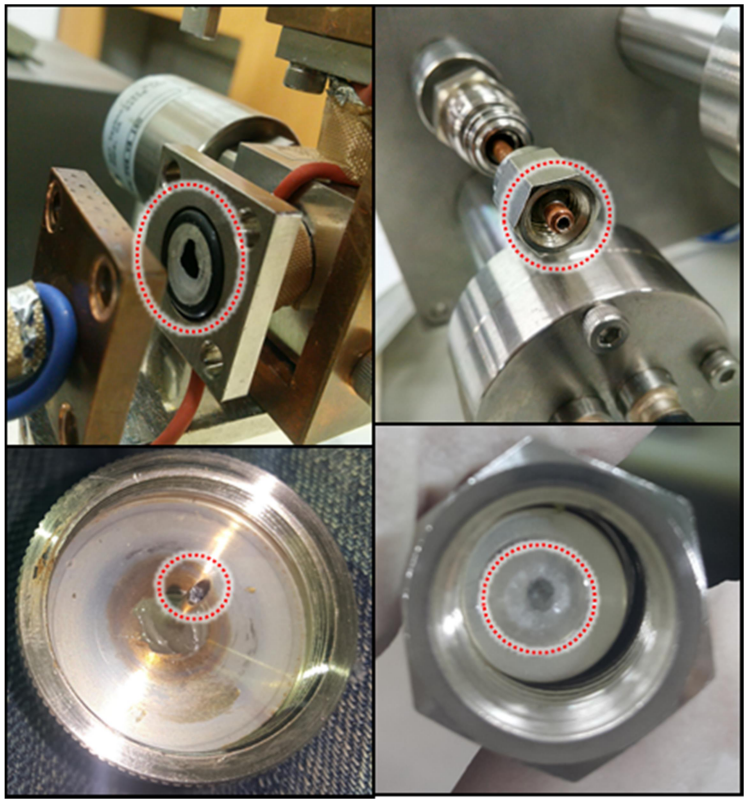

Figure 13 Recrystallizations of precursor gas inside the GIS

The EDX results in Fig. 15 show that W, C, and O atoms are all distributed in the deposit. Although it is difficult to confirm the formula of the deposited material as a result of the constituent analysis of the EDX, it can be indirectly estimated that the material is $W(CO)_6$.

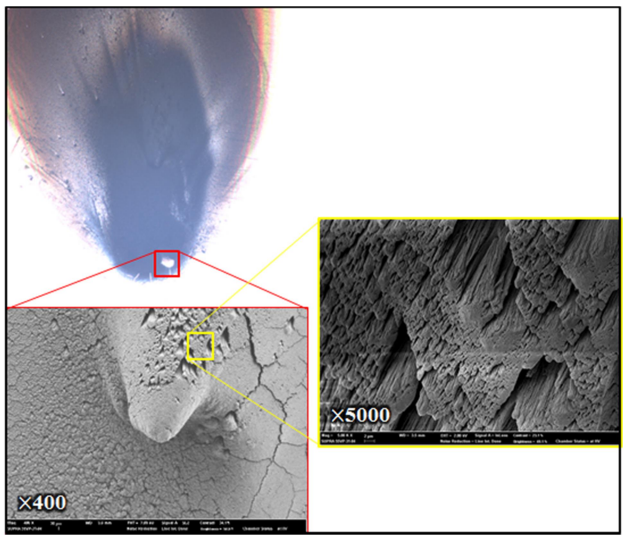

Figure 14 $W(CO)_6$ deposition on a Si substrate using the GIS

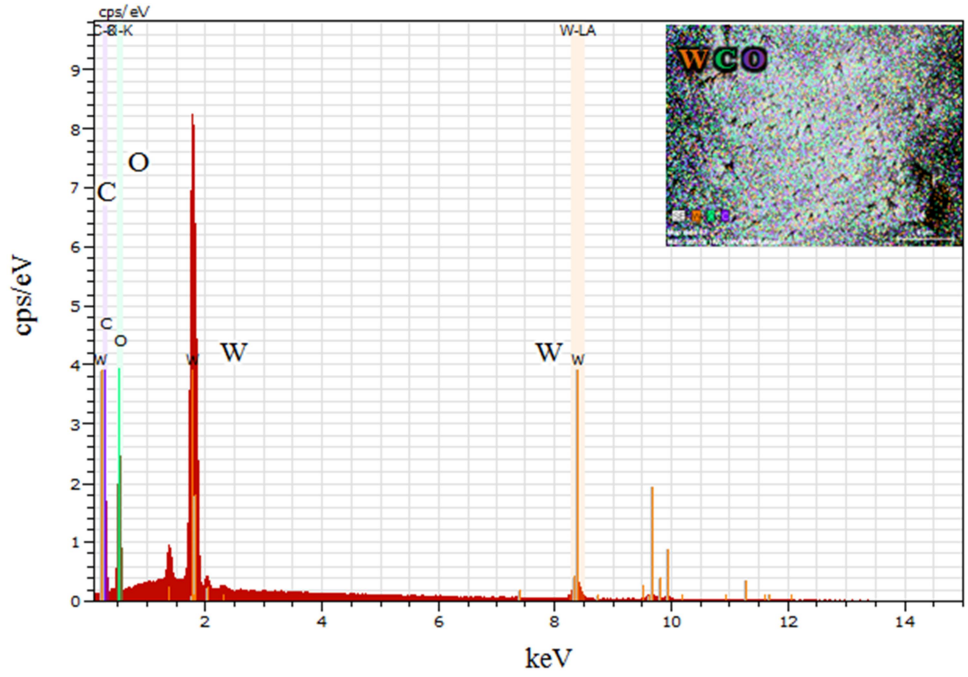

Element	Series	unn. [wt.%]	C norm. [wt.%]	C Atom. [at.%]	C Error (3 Sigma) [wt.%]
Tungsten	L-series	69.90	58.34	9.42	7.97
Oxygen	K-series	24.18	20.18	37.46	10.11
Carbon	K-series	25.74	21.48	53.12	11.24
Total:		119.82	100.00	100.00	

Figure 15 EDX analysis of $W(CO)_6$ deposition

In previous experiments, we could investigate the function of the developed GIS to evaporate solid precursor materials and transfer the precursor gas to the substrate in a vacuum chamber without vacuum leakage. In this step, a preliminary experiment is carried out to investigate the how the deposition characteristics changes according to the temperature change of the precursor gas which is the main subject of this study. The temperature of the reservoir was maintained at 68 °C to fix the amount of gas flux. For the precursor gas temperature change, only the temperature of the nozzle was maintained at 75 °C, 83 °C, and 92 ~ 95 °C.

Figure 16 (a) shows the optical images of the deposited materials with varying the nozzle temperature. These images were analyzed by image processing and the deposited areas were expressed in Fig. 16 (b). From the experiment result, it was confirmed that the deposition area increases as the temperature of the nozzle rises. In addition, as the temperature increased, it was confirmed that water vapor was deposited together in the deposit. Water vapor is an important external factor in CVD processes using high vacuum conditions and is mentioned as a factor affecting the quality of lamination in many CVD related literature. The water vapor is also absorbed in the inner wall of the ultra-high vacuum chamber, and sometimes comes from polymer materials used for the GIS, or oxidized precursor material. In some cases, external air is absorbed through fine pressure leakage. Precursor molecules and water molecules compete for adsorption on the substrate surface, affecting the deposition rate and purity [43]. It was later confirmed that the main cause of the water vapor in this study was due to the fine vacuum leakage of the GIS.

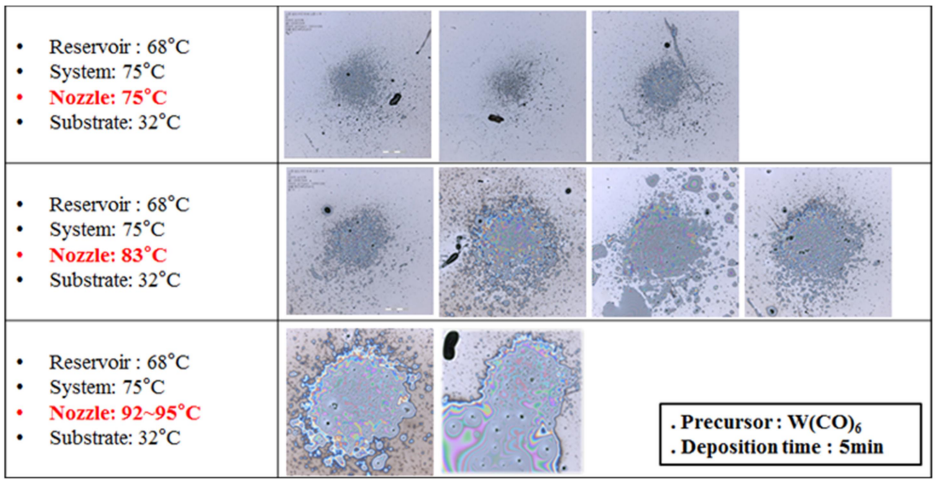

(a) Pictures of $W(CO)_6$ deposited materials according to the nozzle temperature

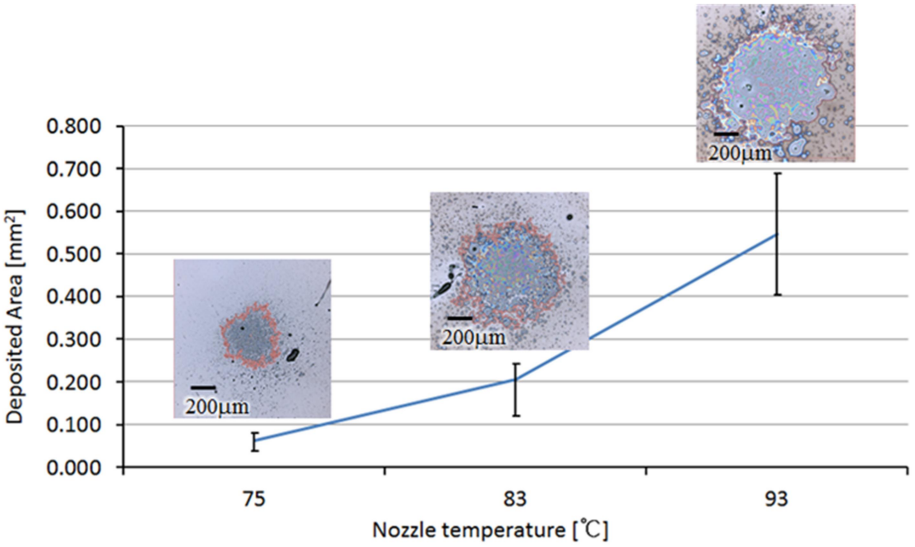

(b) Deposited area with nozzle temperature variation

Figure 16 (a) Images of $W(CO)_6$ deposited material on Si substrate and (b) the tendency of deposited area according to the nozzle temperature

2.2 Experimental setup of FIB-CVD process

The Figure 17 shows the focused ion beam system used in this experiment. At the custom manufactured chamber, FIB column (COBRA, Orsay Physics, France),

high precision 5-axis eucentric stage (UST-5100, E. Fjeld, USA) and vacuum systems were installed. The developed GIS was evaluated by using a separate vacuum chamber, and the FIB-CVD experiment was conducted by attaching the evaluated GIS to the FIB chamber. Figure 18 is a conceptual design depicting the installation of the developed GIS in a FIB chamber. The reservoir containing the precursor material is located outside the chamber and the actuating part with the nozzle was equipped using a gasket to prevent the vacuum leakage into the port of the chamber. The tube through which the precursor gas passes is made of copper material and connected to the inside of the vacuum chamber through the feedthrough. To separately heat the nozzle, the power line and the T/C wire data line were connected inward through the feedthrough. Figure 19 shows the internal predicted image when the GIS is installed. The substrate is placed on a stage capable of three-axis control and is located directly under the FIB column. FIB column was Cobra FIB column model and gallium was used as LMIS ion source. The secondary electron detector (SED) detects secondary electrons generated during real-time processing and displays processed images. Micro force sensor and micro gripper were installed to handle microscale devices and to measure mechanical properties. For the temperature control, a controller capable of 6 channel programmable temperature control was fabricated. GIS nozzles were designed to be able to move repeatedly at idle and working positions by 30mm intervals. The IDLE position is a home position, where the nozzle stays when the work is not in progress, and the working position is the position where the FIB-CVD operation is performed when the precursor gas is supplied to the target position. As mentioned earlier, the position of the nozzle is an crucial parameter

affecting the quality of the FIB-CVD process, and the results of the study on the effect of the EBID or FIB-CVD process on the position and shape have been published [10, 44]. Generally, the nozzle is used at a height of a few hundreds of micrometers from the surface. The distance from the center of the ion gun also affects a significant effect on the local pressure, which, like the height, is located a few hundred micrometers from the center. In this study, the distance from the center to the nozzle tip was set to maintain a spacing of about 720 μm.

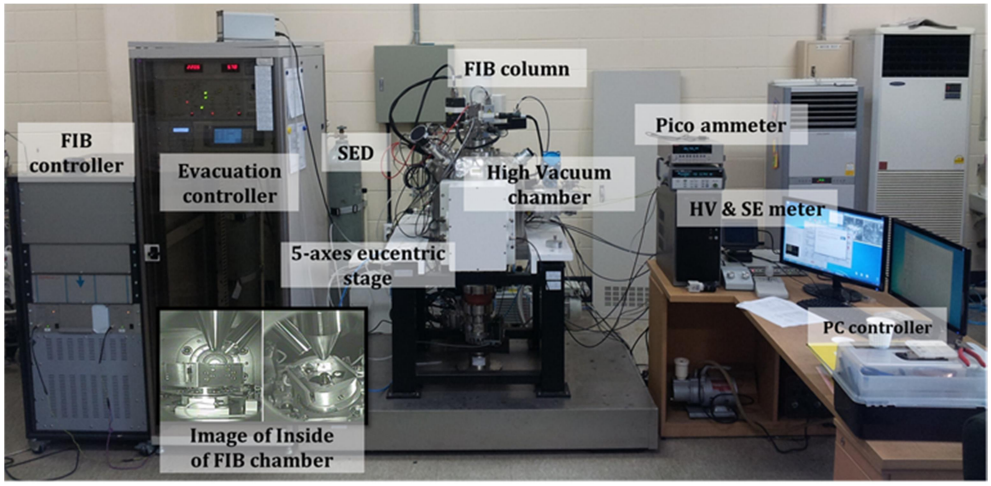

Figure 17 Equipment for the FIB-CVD process

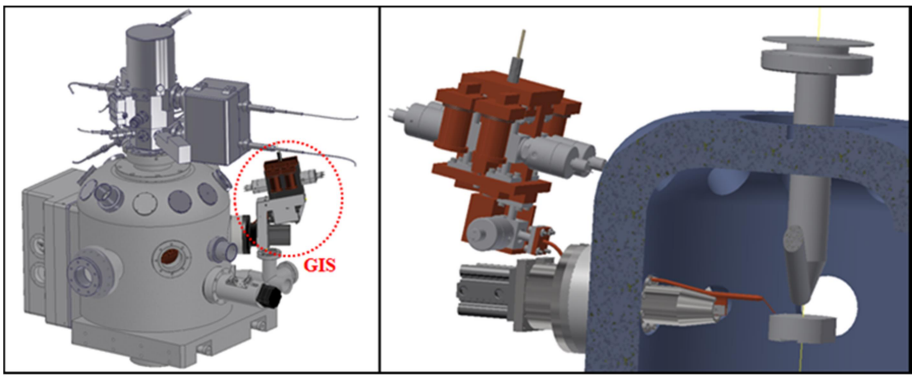

(a) An illustration of the GIS installation for the outside

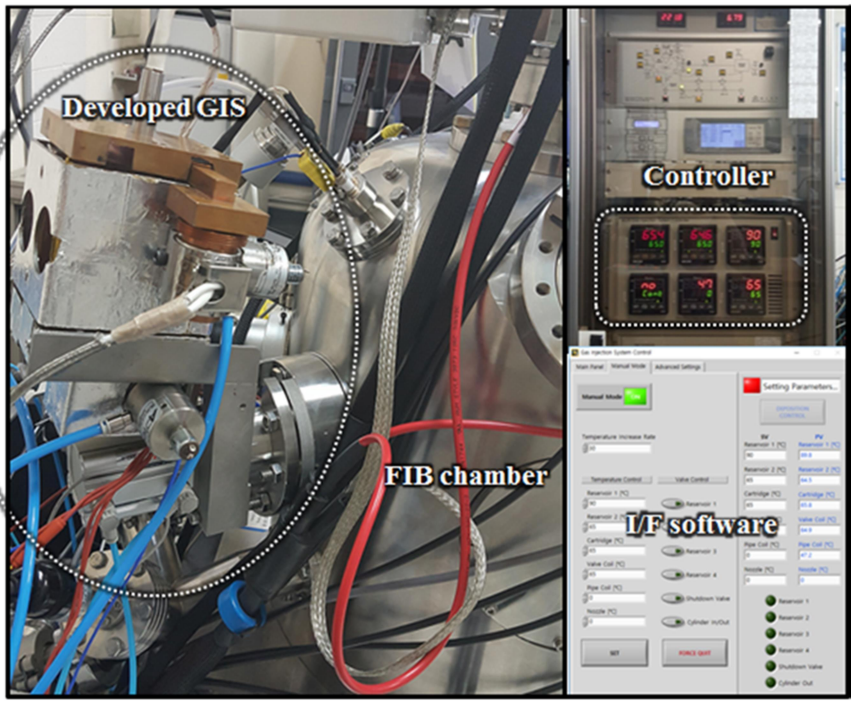

(b) The GIS installation view from the outside

Figure 18 Appearance of FIB chamber installed with the GIS

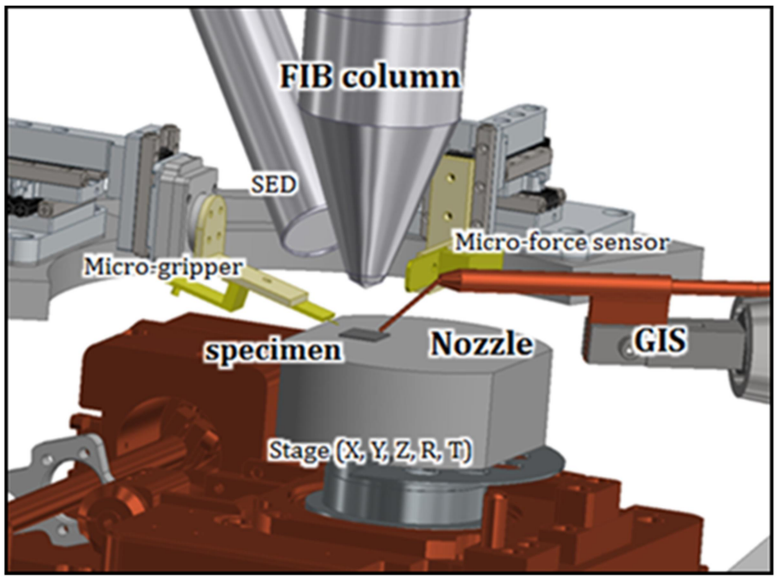

(a) An illustration of the GIS installation for the inside

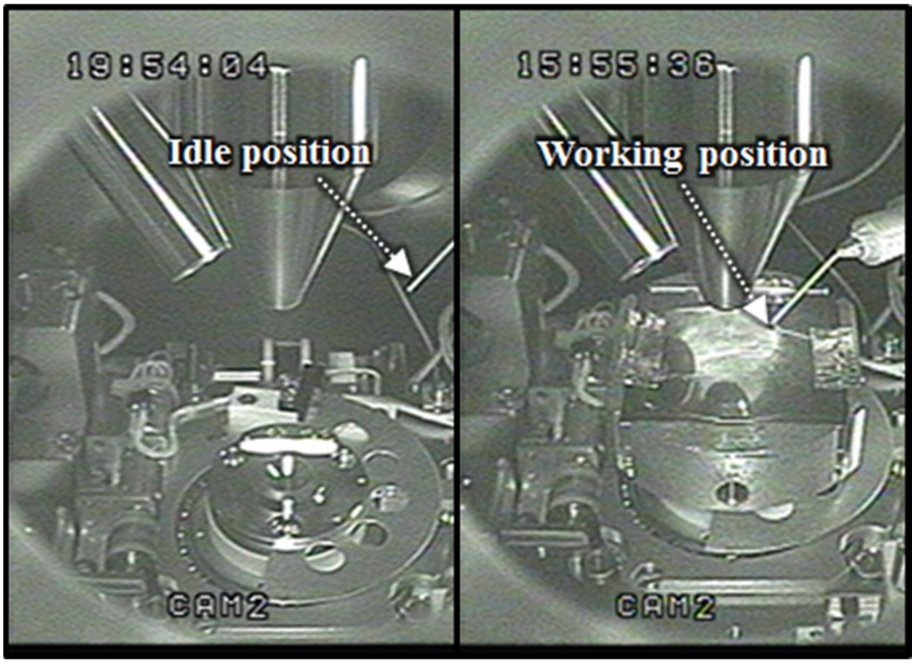

(b) The GIS installation view from the inside

Figure 19 Inside view of FIB chamber installed with the GIS

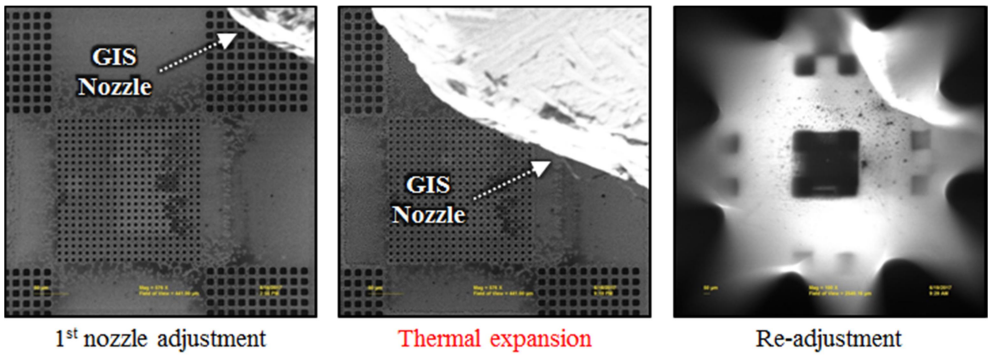

Figure 20 Adjustment of the nozzle of the GIS

Figure 20 shows the process of positioning the nozzle when installing the GIS in the FIB chamber. After the first GIS installation, the position of the nozzle was measured to be about 300 μm away from the center when confirmed by SEM image. However, after heating the nozzle, it approaches within 100um from the center due to thermal expansion. This is a distance that limits the deposition feature size and needs to be readjusted. Therefore, it was reinstalled considering the thermal expansion, so that the distance was adjusted to about 800um away from the center. Several critical problems occurred during the evaluation of the installed GIS in the FIB chamber. Figure 21(a) shows the blurred image of SEM caused by the electrical ground trouble of the nozzle part. Noise in the SEM image was generated due to the floating ground when power was applied to the installed heater to independently control the nozzle temperature. Figure 21(b) shows a recrystallization problem caused by temperature drop while precursor gas flow passes through a thick chamber wall. In order to solve the problem, the thermal insulator was reinforced between the GIS and the FIB chamber. Figure 22 is a SEM image showing unexpected deposits generated during FIB-CVD deposition

experiments. The FIB-GIS should keep the internal pipeline clean to ensure the purification of the deposit. To avoid such problem, therefore, it is necessary to remove the residue used in the previous operation. In order to do such a work, a process called purging and degassing must be executed before use. By the result of composition analysis for overspray deposit through EDX, it was confirmed that the main component of the unintended deposit was carbon, which was estimated to be due to the residue of gas used in the previous work.

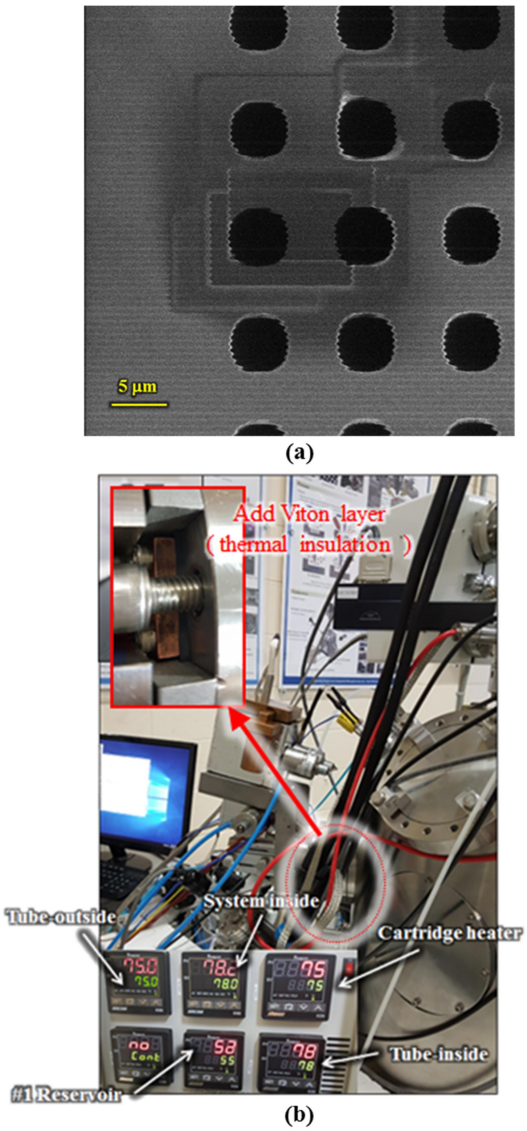

Figure 21 (a) SEM image showing blurred problem due to electric noise and recrystallization at the connection area by the heat loss

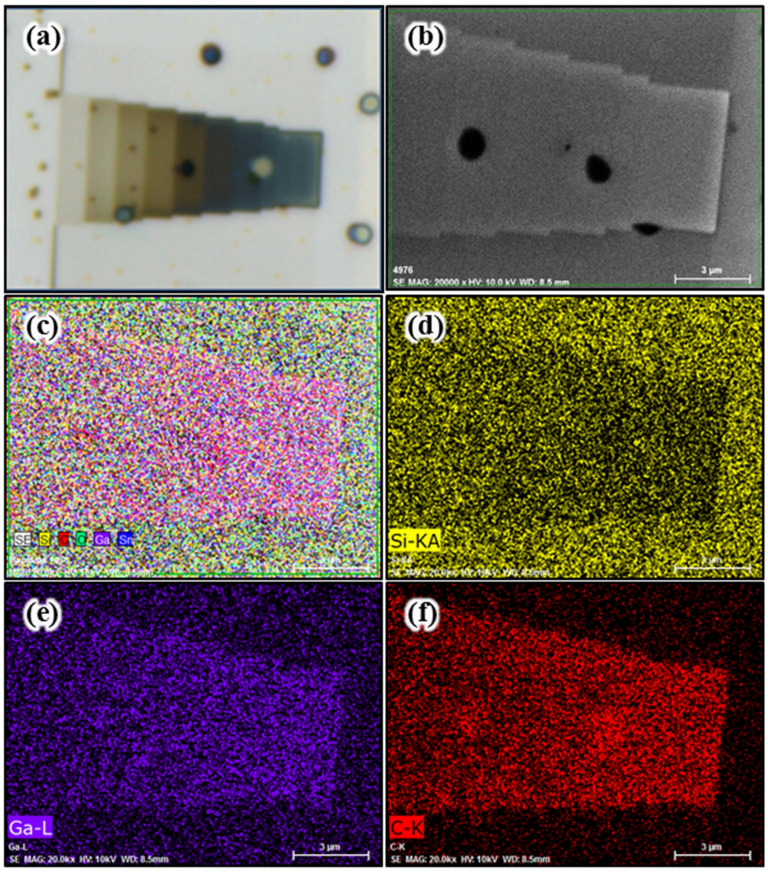

(a) Map data of constituents

Element	Series	unn. C [wt.%]	norm. C [wt.%]	Atom. C [wt.%]	Error (3σ) [wt.%]
Silicon	K-series	86.61	82.02	67.18	10.63
Carbon	K-series	17.02	16.12	30.87	6.47
Oxygen	K-series	1.27	1.20	1.73	0.65
Gallium	L-series	0.69	0.66	0.22	0.20
Total		105.59	100.00	100.00	

(b) Spectrum of constituents

Figure 22 EDX analysis of the contamination deposit during FIB-CVD process

Chapter 3. Experiment

3.1 Preliminary experiment

The FIB-CVD process is known as a mechanism in which a non-volatile component is deposited on a substrate in the process of decomposing precursor gas molecules adsorbed on the surface by emitted electrons generated by the incident ion beam energy. Based on this mechanism, the deposition environment of FIB-CVD can be roughly divided into two regimes. The first regime is a gas-limited regime (mass transport-limited regime) in which the precursor adsorbate is sufficient but the reaction is insufficient due to the lack of electrons that cause decomposition. On the contrary, the electron-limited regime (reaction rate-limited regime) lacks the emitted electrons involved in the reaction and the depletion occurs due to the lack of precursor adsorbate [24, 45]. If the limited regime is different, the deposition will vary even if the same operating parameters are used. The deposition rate is one of the representative qualities in FIB-CVD process. Deposition rates can be subdivided into vertical, lateral and volumetric growth rates as shown in Figure 23. As described above, the deposition characteristic of the FIB-CVD process is closely related to the operating temperature. Studies related to temperature have been reported that analyzed the effect of reservoir temperature and substrate temperature on deposition characteristics, respectively.

As the reservoir temperature rises, not only the temperature of the precursor gas but also the amount of flux increases, so that the deposition rate increases. Studies have shown that as the substrate temperature rises, the adhesion coefficient of the molecules changes directly, and in the case of cobalt deposition, the purity of the deposition rate increases [41]. However, the influence of precursor gas temperature on the deposition characteristics of FIB-CVD has not been studied yet. In this study, we conducted an experiment to analyze the influence of the precursor gas temperature on the deposition, especially in terms of deposition rate. For the experiment, the precursor material was phenanthrene ($C_{14}H_{10}$) was used. The base pressure of the FIB chamber was around 4.7~4.9×10^{-6} Torr, and the pressure when the precursor gas was supplied was maintained at 5.9~6.0×10^{-6} Torr. The reservoir temperature was maintained at 54 ~ 56 °C, and the GIS body was maintained at 72 °C over the entire body of the GIS. The nozzle temperature was set at 68 °C and 75 °C. In previous studies, the researchers have used slightly different operating temperatures due to the different FIB-CVD process environment and facility. For example, in a FIB-CVD experiment using the same phenanthrene, Jun Dai et al. Used a reservoir temperature of 60 °C, 70 °C, and 80 °C [46], Masahiko Ishida et al. conducted in 65°C ~ 85°C [47], and Fujita et al. used a reservoir temperature of 85 °C to 100 °C in their study on the resonant characteristics of amorphous carbon pillar [48].

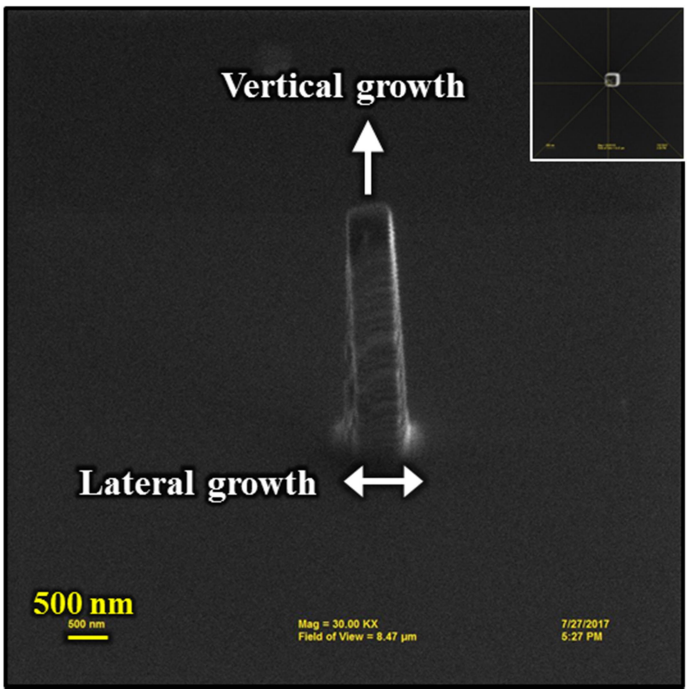

Figure 23 Definition of Growth rates in pillow deposition by FIB-CVD

In order to observe the influence of the temperature change of the precursor gas in the deposition experiment, the temperature of the reservoir and the substrate temperature were maintained at the same value. The results were shown in Fig. 24. From the experimental results, it was confirmed that the shape of the deposition varies depending on the temperature change. When the precursor temperature is 75 °C, other deposit material other than the intended deposit structure was adsorbed. This undesired deposition, which is represented by overspray, halo, etc. in previous studies is known to be due to the tail or back scattered electron of the FIB and similar images can be found in several papers [24, 39, 49]. In addition, there was the study that this unexpected deposit does not affect the electric properties of the deposition [50].

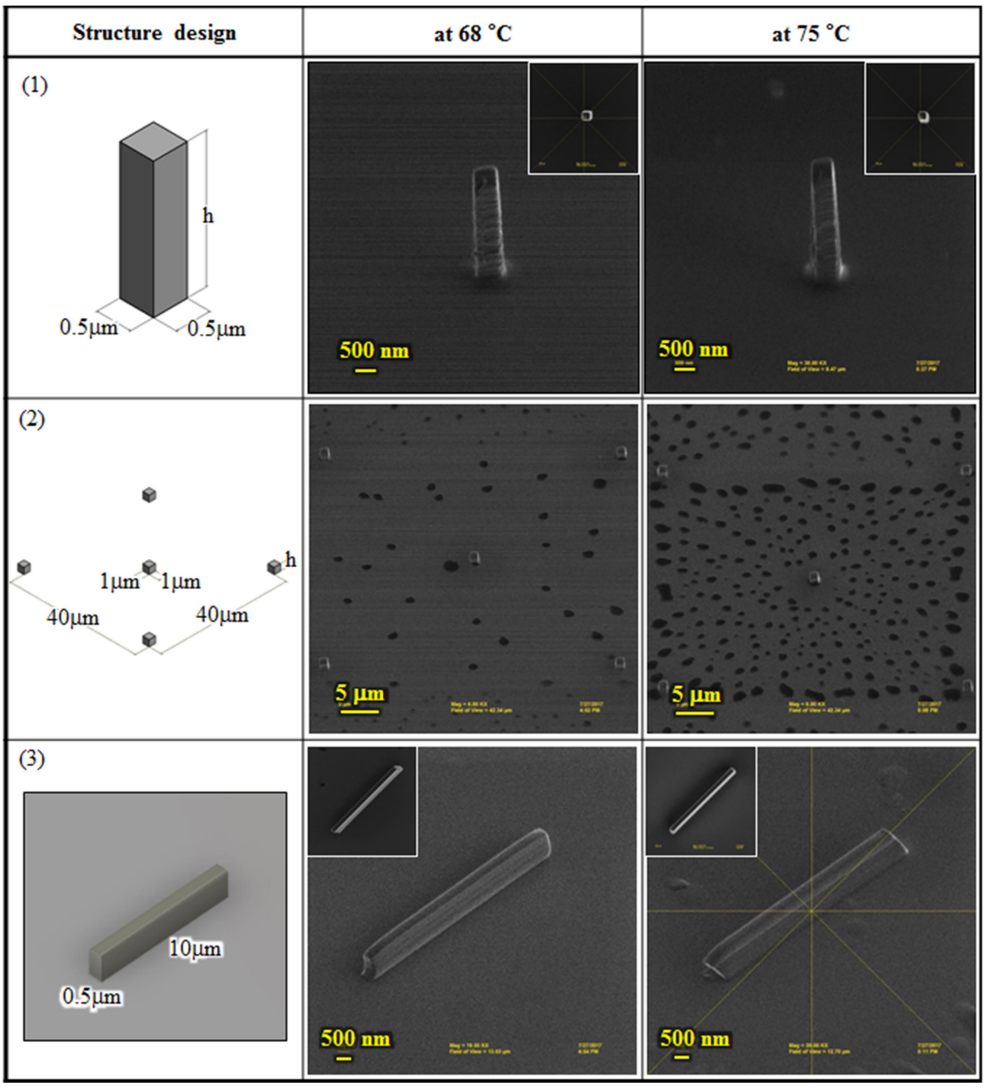

Figure 24 Deposited structures by FIB-CVD

The second deposition experiment was carried out with reference to the preliminary experiment. Deposition structures are shown in Fig. 25. The first structure is designed to be obliquely deposited in the vertical direction, and the second structure is designed to deposit a plurality of wall-shaped structures. This structure is designed to observe how effectively the precursor gas can be supplied to the locally deficient region of the precursor gas supply. Experimental conditions

were the same as in the previous experiment, that only the nozzle temperature was increased from 60 °C to 85 °C in 5 °C increments. Figure 26 shows SEM images of the results of deposit with temperature change. As can be seen from the results, it can be observed that the change in the deposited structure is caused by the change in the precursor temperature.

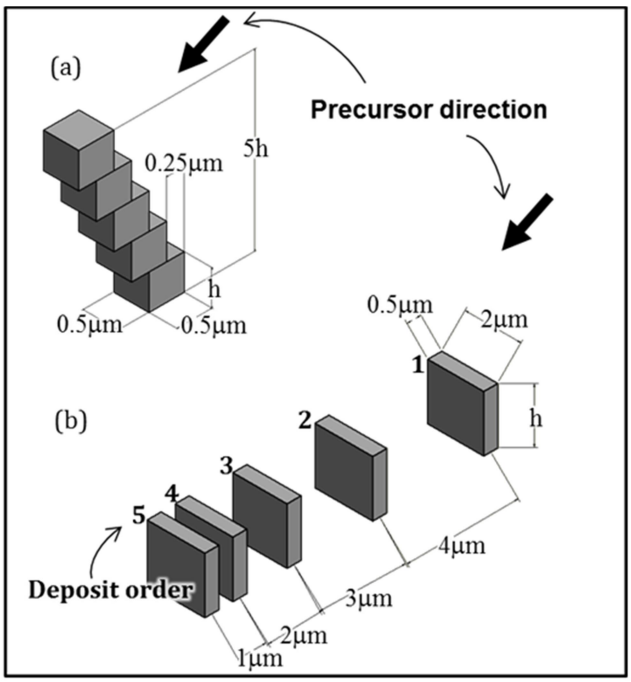

(a) Structure designs

Precursor	$C_{14}H_{10}$	
Ion Beam	Ion energy (keV)	30
	Ion Dose (pA)	10
Temperature (℃)	Reservoir	60~62
	System	70
	Nozzle	**65, 70, 75, 80, 85**
Pressure (Torr)	Base	4.8~4.9 x 10^{-6}
	Supplement	6.1~6.3 x 10^{-6}

(b) Experimental conditions

Figure 25 Deposited structures and experiment conditions

The lateral growth through the atomic concentration of constituent material and image processing tool through EDX analysis is shown in Fig. 27. The change in precursor temperature is not closely related to the change in the composition of the deposited material, but the deposition rate especially the lateral growth rate is closely related. In Eq. (1), the diffusion coefficient is increased and the lateral growth rate is increased with increasing temperature. The result is a good agreement with the results of other researches. In recent years, researches have been published that analyzes the characteristics of electrons affecting vertical growth rate and lateral growth rate through simulation [51]. Smith et al. reported the simulation results that the vertical growth rate in the EBID process is affected by the primary electrons and their secondary electron, and the lateral growth rate is influenced by the backscattered electron and the secondary electrons generated by them. There was also a study that analyzed the topography changes with temperature change. When the lateral growth rate is large, it can be seen that the deposition topography changes due to local depletion on the surface as shown in the image. This phenomenon is known to be due to the non-uniformity of the consumption rate of the precursor adsorbate generated in each region, and it can reduce the problem by optimizing the beam scan pattern [12, 52]. As the precursor temperature rises, the lateral deposition rate increases. The increase of lateral deposition rate means that the supply of precursor gas has proceeded smoothly by the diffusion in the region where the supply of precursor gas is insufficient. Therefore, it can be seen that the increase of precursor gas temperature activates the diffusion of gas molecules on the substrate.

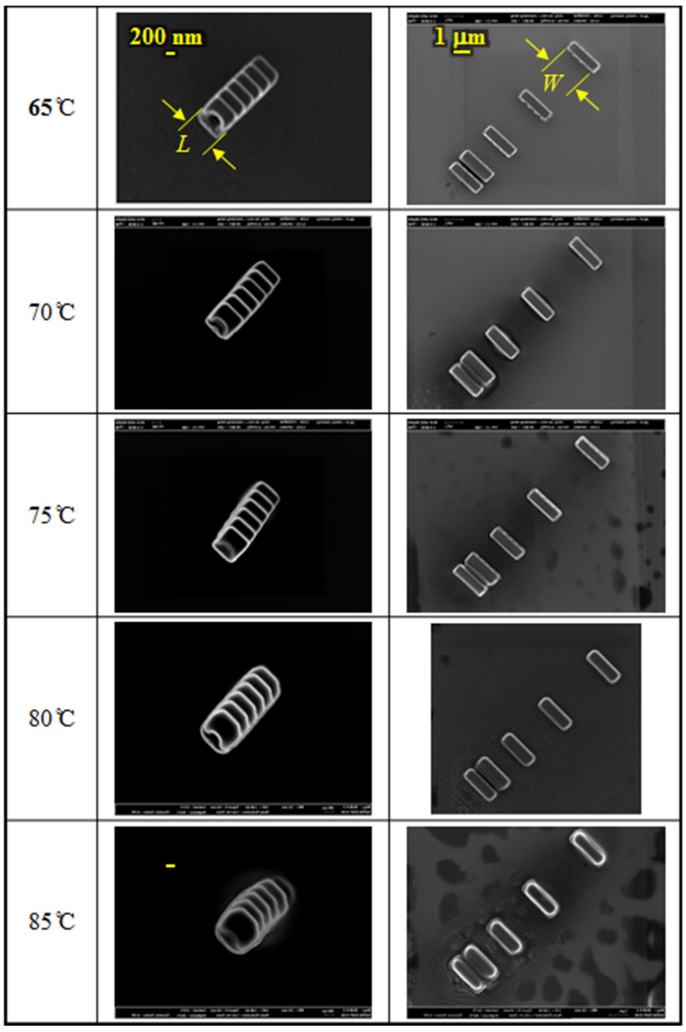

Figure 26 SEM images of Stepwise beveled structure and planar cuboids according to the temperature variation

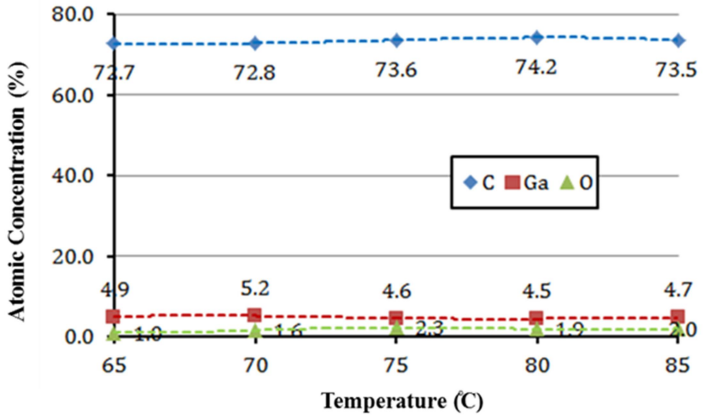

(a) Atomic concentration according to the temperature variation

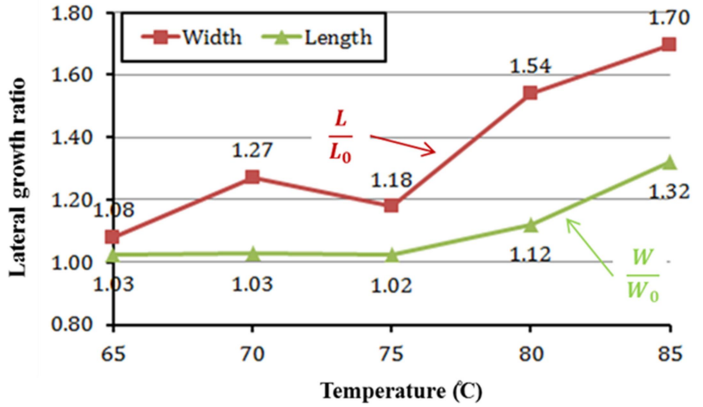

(b) Tendency of lateral growth rates according to the temperature

Figure 27 Tendency of atomic concentration and lateral deposition rate according to the precursor gas temperature

3.2 Surface diffusion and precursor gas temperature

In the preliminary experiment, it was observed that the lateral growth rate of the deposition material changes with the change of the precursor temperature. That is, the lateral growth rate increased while the temperature of the precursor rose from 65 °C to 85 °C. However, since 2D SEM images have limitations in the analysis of

vertical growth rate, additional experiments were performed to measure the change in total growth rate. Table 4 shows the experimental conditions.

Table 4 Experiment conditions for pillar deposition

Ion beam	Energy [keV]	30
	Current [pA]	20
	Spot size [nm]	50
	Pattern	Spot
	Dwell time [second]	10^{-5}
	Refresh time [second]	0
	Scan count [times]	$1x10^5$, $3x10^5$, $5x10^5$, $1x10^6$, $2x10^6$, $3x10^6$
Precursor	Material	Phenanthrene
	Reservoir temperature [°C]	68~70
	System temperature [°C]	73
	Nozzle temperature [°C]	70, 75, 80, 85
Vacuum	Base pressure [Torr]	4.5~4.7 x 10^{-6}
	processing pressure [Torr]	6.1~6.2 x 10^{-6}

During the entire experiment, the temperature of the reservoir was adjusted between 68 and 70 °C to keep the amount of precursor flux uniform. Nozzle temperature increased from 70 °C to 80 °C in 5 °C increments. Deposition was performed by changing the scan count and precursor gas temperature while keeping the position of ion beam fixed. If the scan count is increased with the same temperature condition, the deposition evolution with time can be observed. In addition, the influence of temperature on the stacking can be analyzed by deposition while changing the temperature in the same scan count. The scan count

is a value entered in the FIB operating software, and is generally based on the amount of ion dose when comparing the deposition rate. The scan counts are calculated to the values of 1.25×10^8, 3.75×10^8, 6.25×10^8, 1.25×10^9, and 3.75×10^9 ions respectively by converting to the number of ions using the conditions of Table 4. In order to increase the reliability of the experimental results, experiments were repeatedly conducted three times under the same conditions. The AFM measurement results for the deposit at the gas temperature of 80°C are shown in Fig. 28. From this data, it can be observed that the lateral and vertical growth rates increase as the precursor temperature rises even under the same amount of precursor gas supply.

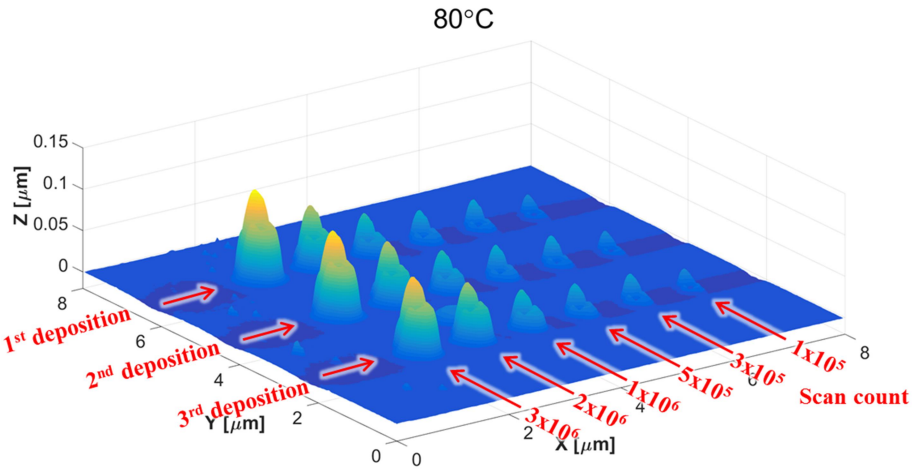

Figure 28 Deposition topography at 80 °C precursor gas temperature measured by AFM

The Fig. 29 (a) shows the results of AFM measurement of the deposited results at precursor gas temperatures of 70 ° C to 85 ° C. Figure 29 (b) shows the cross section of the deposit according to temperature when 3.75×10^9 ions are

introduced. It can be seen that the results of three experiments are almost similar. From the chart, as the precursor gas temperature rises, it can be seen that the amount of deposition increases both in the lateral and the vertical direction. In addition, the cross sections of the deposited material at each temperature commonly show that the central part of the beam is depressed regardless of temperature. It is considered that incident ions cause not only deposition but also material removal by sputtering mechanisms and redeposition of the sputtered particles to the surface [6, 53]. Generally, as the energy of the ion beam increases, the growth rate increases, but at the same time, the material removal rate increases simultaneously. FIB-milling as well as FIB-CVD has been actively studied by many researchers. However, this study considers only lateral and vertical directional growth of the deposit without consideration of milling phenomena

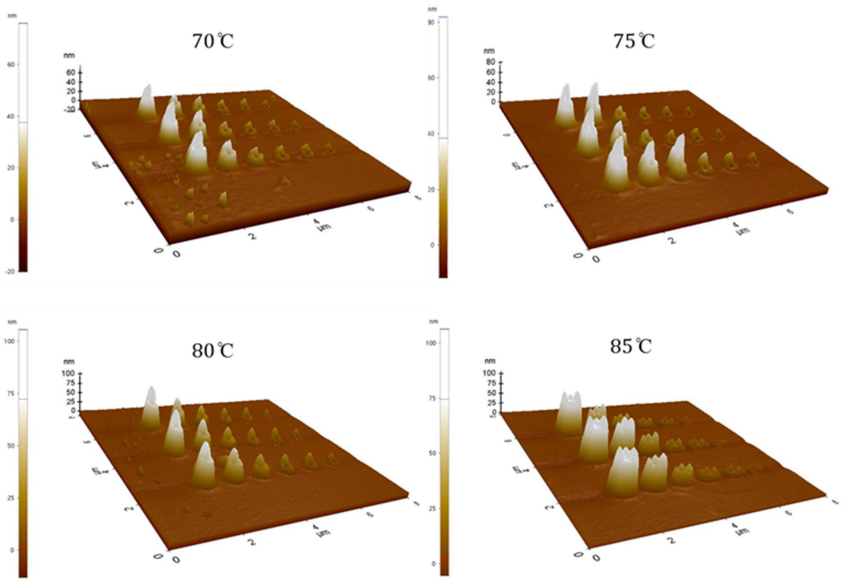

(a) Deposition topography analysis using AFM

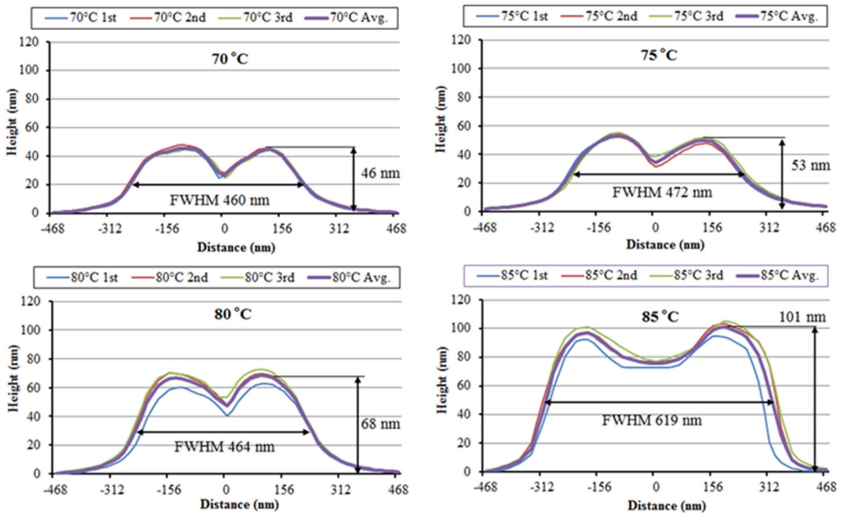

(b) Cross sections of pillars deposited with various temperatures at 3×10^6 scan counts

Figure 29 AFM analysis of deposited pillars according to the variation of precursor gas temperature

Figure 30 shows the comparison results of the vertical, the lateral, and the volumetric growth rate of the cross section of the deposits that vary with precursor temperature. The result shows that as the temperature rises, the growth rate

increases in all directions. This phenomenon is generally similar to the increase in the amount of precursor gas flux in the gas-limited regime and the increase in the dose of ion or primary electron in the electron-limited regime [54]. However, this result shows a slightly different phenomenon from previous studies related to temperature. In general, as the substrate temperature increases, the lateral growth rate increases, but the vertical growth rate is different from the tendency to decrease due to the limit of the overall deposit rate. As the gas temperature rises, we can see that the side, vertical, and volumetric growth ratios all rise, which means that it affects other physical phenomena mentioned in Eq. (1) besides diffusion. Identification of these phenomena was verified through theoretical analysis through simulation in the following chapter.

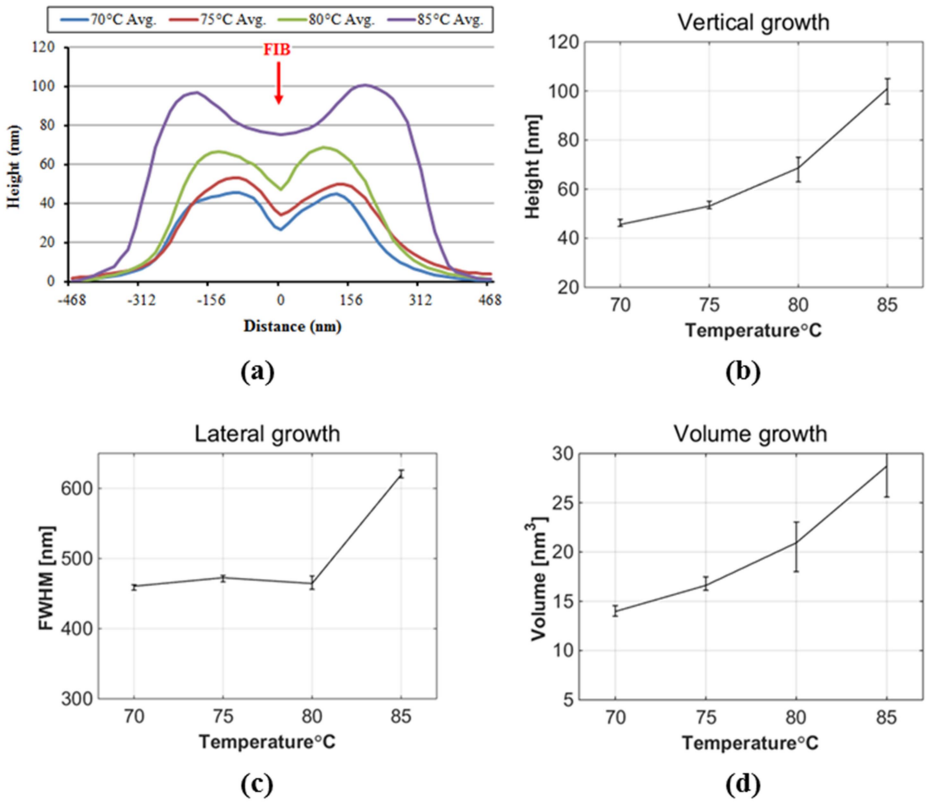

Figure 30 Growth rates of pillars according to the precursor gas temperature

Chapter 4. Modeling and Simulation

In the time since focused, ion beam-induced, chemical vapor deposition (FIB-CVD) was first introduced in the 1980s, it has become widely used not only for repair of semi-conductors, but also in the fabrication of various micro-/nano-structure devices including electronic components, sensors/actuators, and even nanomaterials [14, 15, 55-59]. Such work generally falls into one of three categories. First, the process is used to fabricate complicated 3D structures or functional devices [60-64]. For example, as the process permits direct metal writing with an accuracy of several tens of nanometers, Puers et al. fabricated microelectromechanical systems (MEMS) devices via vacuum encapsulation [64], and Zakharov et al. developed sub-micron-sized actuators made of TiNiCu shape memory alloy (SMA) ribbon [60]. Second, the process is used in an auxiliary capacity in various applications [65-68]. Shao et al. employed an FIB-CVD process to fabricate test structures from exfoliated graphene, and created Pt electrodes to investigate the relationship between temperature and graphene electrical resistance [67]. Also, Watanebe et al. fabricated photonic nanostructures resembling real morpho-butterflies; the optical characteristics were near-identical to those of real butterflies [68]. Third, FIB-CVD per se has been studied by several researchers [13, 24, 69-72]. An understanding of the process is essential to improve overall efficiency and reproducibility. Two major interpretative approaches are possible. One is to elucidate depositional characteristics experimentally under various

conditions. Fu et al. studied the effects of process parameters, such as the dwell time, beam spot size, and current on the deposition yield [13]. Igaki et al. compared the growth rates of pillars and the electrical conductivities of carbon wires fabricated via FIB-CVD and electron beam-induced deposition (EBID) [72]. Thus, the experimental approaches tend to focus on analysis of process parameters related to deposition characteristics [13, 47] or in-situ monitoring [70, 71], or compare process characteristics with those of alternative methods [24, 72]. The other approach is to build a plausible theoretical model interpreting the fundamental mechanism, which includes complicated interactions among ions, electrons, precursor molecules, and the solid surface. The theoretical models are generally separated into continuum and discrete models in terms of processing of depositional events. Continuum models feature deposition rate equations [20, 24, 73]; the distribution of precursor molecules adsorbed on the surface is defined by a continuous function of distance and time. Such models usefully estimate the effects of relatively large-scale parameters; the calculation costs are not high. On the other hand, discrete models treat deposition events as probabilistic interactions between precursor molecules and emitted electrons [34]. Such models afford significant advantages when analyzing mechanisms at atomic and molecular scales. In addition, they more appropriately reflect process coefficients representing adsorption, desorption, residence time, and diffusion under various conditions.

Recently, with realization of the infinite potential of artificial intelligence (AI), technologies closely related to human behavior are rapidly emerging. One such application is image-processing based on computational technology. Numerical methods used for image-processing basically operate on a finite discrete

domain consisting of unit elements termed pixels (or voxels), and are similar to those of computer-aided engineering (CAE) methods that seek to solve physical or mechanical problems of continuous space by converting such space into discretized grid domains. Therefore, numerical methods used in computer vision may potentially be used in CAE; interdisciplinary efforts would be worthwhile. The Hausdorff distance (HD) is a widely used image-processing technique in pattern-recognition and object tracking [74]. The HD quantifies the distance between, and similarity of, two objects by converting Euclidean distance to a numerically approximated distance in a discretized space.

In this chapter, we simulate the evolution of deposition induced by a focused ion beam. Although numerical methods can better describe the fundamental deposition mechanism, most previous works used continuum models, because numerical methods usually are difficult to adequately consider interactions between emitted electrons and adsorbed precursor molecules on the evolving depositional surface due to the heavy computational burden [20, 21, 24]. To avoid this difficulty, some previous studies using numerical models assumed that the electrons were emitted in a direction normal to the surface [34], or an additional continuum model was incorporated [23]. Another difficulty is associated with the intrinsic characteristics of Monte Carlo (MC) simulation. In numerical simulation of FIB-CVD or EBID, the MC method is widely used to model the trajectories of ions and electrons, and the behavior of precursor molecules on the substrate surface. Millions of molecules and electrons are generally included in MC simulation [23, 34, 51], which crucially describes the molecular kinetics and the electron trajectories, but at the cost of significant calculation time [75]. Moreover, if the

simulation includes dynamic deposition evolution (which is indispensable when calculating the distance between the deposition surface and the emitted electrons), the calculation time increases further. In this study, we used the HD concept to alleviate such difficulties. The dynamic surface boundary composed of the substrate and the evolving deposition was expressed as distance transform (DT) map containing information on the shortest distance to the surface; the distance from a traveling electron to the nearest surface can be directly calculated without involving Euclidean calculations. This method allows rapid evaluation of electron emission, and determination of emission position, without any additional assumptions. In addition, more electrons and ions can be included in the simulation than in previous studies.

4.1 Dynamics of precursor gas flow

The degree of rarefaction of a gas is generally expressed through the Knudsen Number, K_n which is the ratio of the mean free path to the characteristic length. Generally, the regime, $K_n < 10^{-3}$ is regarded as hydrodynamics regime or continuum flow regime in which the Euler Equations are available. The regime where $K_n < 10^{-1}$ is called slip flow regime where the Naiver-Stroke Equations which use the mass, momentum, and energy conservation law are valid. But, from the continuum-rarefied regime, $10^{-1} < K_n < 10$, the continuum assumption becomes invalid, yet the free molecular assumption is too early. In this regime, the Boltzmann Kinetic Equation or DSMC method can be useful. In the regime, $K_n > 10$, it is regarded that the mean free path of the molecules is larger than the size of the chamber or the

object under test. It means that there is almost no intermolecular collision. The behavior of the fluid can be just described as the average of the quantized molecular properties and as a analysis modeling methods, Molecular Dynamics (MD) which is deterministic approach modeling and the Direct Simulation Monte Carlo (DSMC) method which is probabilistic modeling are generally used.

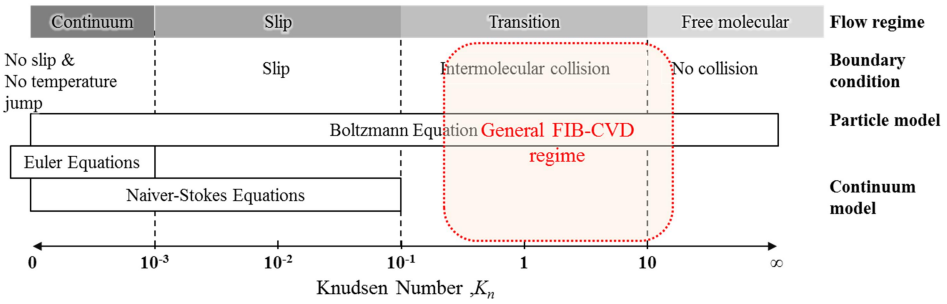

Figure 31Classification of rarefied flow regimes by Knudsen number

In the Focused Ion Beam (FIB) processing with gas-assisted, it is crucial to control the spatial distribution of precursor gas molecules on a substrate. Therefore, it is important to understand the characteristics of the gas molecules not just only to control the gas flow but also to design the feature of the nozzle and to get optimized position of the nozzle tip around the vicinity of the substrate. Usually the low pressure gas flow is injected into the FIB chamber to keep the background pressure at high level in chamber. As mentioned, the rarefication can be defined by the Knudsen Number Kn. In case of a cylindrical nozzle which has circular cross section, the Knudsen number is defined as:

$$K_n = \frac{\lambda}{d} \tag{2}$$

Where λ is a mean free path of gas molecules, d is inner diameter of the exit aperture of a nozzle. The mean free path λ is the average value of the distance a moving particle is expected to travel until a collision occurs after the collision. The λ of a gas molecule can be estimated from kinetic theory. If the molecules are modeled by hard spheres (HS) which have a diameter δ_m according to the Serway's approach, then the effective cross section of collision A becomes $\pi\delta_m^2$.

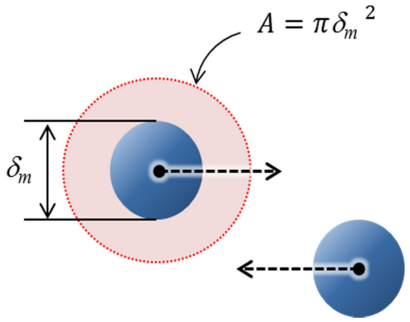

Figure 32 Illustration of effective collision cross section

$$\lambda = \frac{\bar{v}t}{A\bar{v}tn_v} \tag{3}$$

Since the rarefied gas is considered ideal gas, the velocity of the molecule is not defined as one value but has a value according to the Maxwell-Boltzmann distribution. Therefore the mean free path will be described by the following equation,

$$\lambda = \frac{1}{\sqrt{2}\pi\delta_m{}^2 n_v} \tag{4}$$

The number of molecules per unit volume, n_v, can be determined from Avogadro's number, N_A, then the calculation yields the result,

$$n_v = \frac{nN_A}{V} = \frac{nN_A}{nRT/_P} = \frac{N_A P}{RT} \tag{5}$$

Eq. (4) can be described with Boltzmann constant k,

$$\lambda = \frac{1}{\sqrt{2}\pi {\delta_m}^2 n_v} = \frac{kT}{\sqrt{2}\pi {\delta_m}^2 P} \tag{6}$$

As for the pressure at the exit of the nozzle, it is divided by static pressure and dynamic pressure. The static pressure, $P_{sta,}$ means the background pressure, i.e. the pressure of vacuum chamber. And the dynamic pressure, $P_{dyn,}$ is the pressure of the flow gas. Since typically P_{sta} << 10^{-4}~10^{-3} mbar, and P_{dyn} >> P_{sta}, the total pressure at the nozzle exit, P_{exit}, can be calculated as [24],

$$P_{exit} = P_{sta} + P_{dyn} \approx \frac{J_{tot}\sqrt{2\pi MRT}}{N_A} \tag{7}$$

Here, J_{tot} can be measured from the flow sensor, and M is a molar mass of the precursor gas. From Eq. (7), (2), and (3), the Knudsen Number at the nozzle exit can be derived as,

$$K_n = \frac{\sqrt{RT/\pi M}}{8{\delta_m}^2(\frac{Q}{d})} \tag{8}$$

4.2 Simulation of precursor gas transfer model

It is a fundamental purpose of GIS to supply the precursor gas to the substrate. Since the precursor gas is injected into the substrate from a nozzle positioned adjacent to the substrate, it is important to analyze the behavior of the injected gas molecules as they travel to the substrate. Even though analytic approaches for the

simulation of the flux trajectory from the exit of nozzle have been calculated, they were only for the restricted area and needed simpler modeling. Therefore, in order to simulate more complicated situation, numerical approaches have usually been used with the probability of the particles' trajectory ejected from the nozzle exit. The following assumptions were considered to treat the gas flow trajectory.

(a) Molecules are uniformly generated from the entrance surface. And the diffusion scattering concept of molecules against the inner surface of the nozzle is applied. It means that the desorption direction from the inner wall of the nozzle is independent of the direction of incident angle. Therefore, by the analogy of the light reflection, the differential velocity probability of the molecule can be calculated. Figure 33 depicts the surface element of the diffused surface about and, the polar angle with respect to normal to the entrance surface, and the azimuthal angle in each,

$$dA = r\,sin\,\theta\,d\phi \times rd\theta \tag{9}$$

$$p(d\omega) = \frac{sin\,\theta\,\cos\theta\,d\phi d\theta}{\pi} \tag{10}$$

Where *P(dω)* is the probability that a molecule enters within the solid angle dω is a solid angle of the surface element *dA*. In the process using strongly directed impinging precursor gases, the deposition uniformity within the ROI, and the growth rate are critical issues. Nevertheless, these have marginally addressed in the literature. In this study, the simulation tool will be developed to estimate the distribution profile and the growth rate.

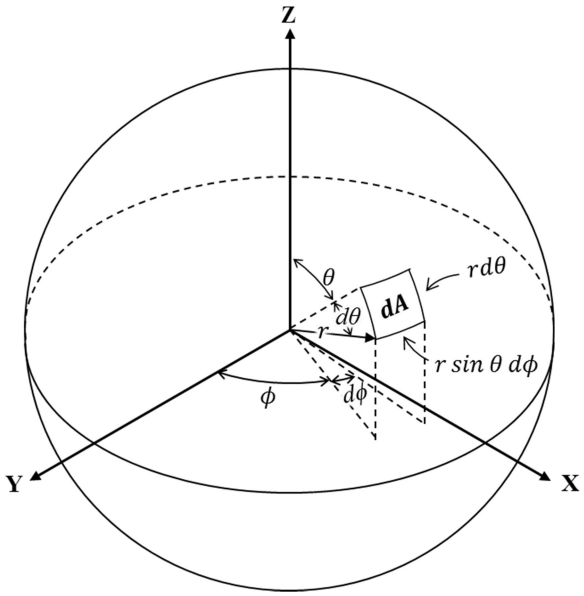

Figure 33 Illustration of molecule-surface collision model

(b) Adsorption of molecules at the inner wall is considered through the uptake coefficient which is practically defined as a probability of sticking onto the inner wall. Because there is no available data or study about the adsorption of molecules in the literature up to recently, and usually it is considered as a stochastic factor based on the experimental results. Therefore, in this research uptake coefficient factor will be manifested in the various values and evaluated the simulation results compared to the experiment

(c) Intermolecular collision within a nozzle is considered. The law of elastic collision model is used to simulate the properties of gas flow at the molecular level. The Hard Sphere (HS) model is an idealized model of the collision of molecular. It regards the gas molecules as hard elastic spheres of diameter (δ_m). Also, with respect to the random collision direction and the large number of collisions it is reasonable to assume polyatomic molecules of a spherically symmetric geometry.

In the HS model, total cross section σ_{tot} at temperature T and the deflection angle λ of the homogeneous gas collision are defined as [24],

$$\sigma_{tot} = \pi {\delta_m}^2 \tag{11}$$

$$\frac{b}{\delta_m} = \cos\left(\frac{1}{2}\lambda\right) \tag{12}$$

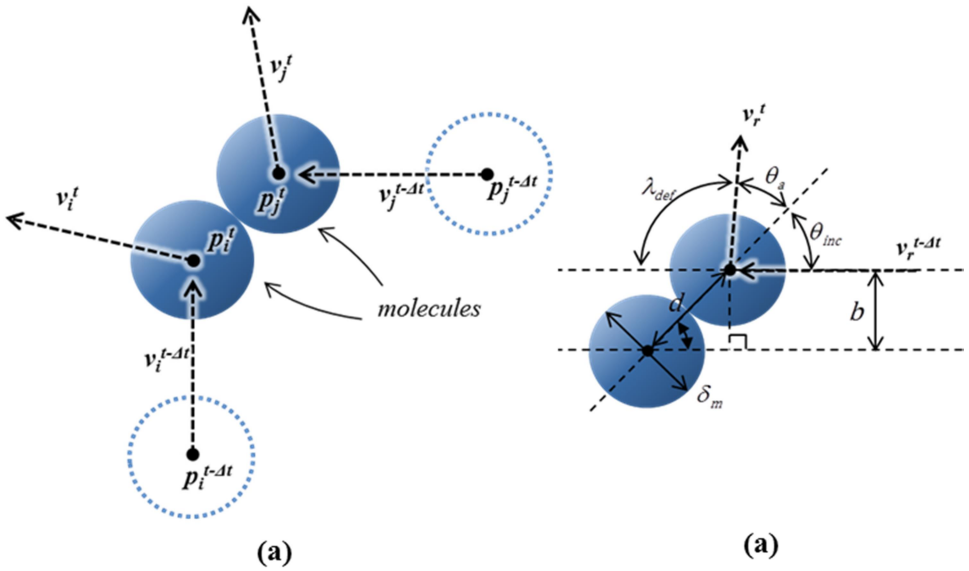

Figure 34 (a) Hard sphere (HS) model and (b) variable hard sphere (VHS) model for inter-molecular collision

In virtue of the assumptions of the HS model, the calculation of the intermolecular collision mechanics can be simple as considering isotropic scattering in the center of mass. However, as well as the calculation benefit, it causes a primary deficiency that the scattering law is not realistic in the real gas flow. In order to correct the primary deficiency of the HS model, Variable Hard Sphere (VHS) model was introduced by Bird. In the VHS model, molecular diameter is variable and defined as a function of v_r

$$d = d_{ref}\left(\frac{v_{r,ref}}{v_r}\right)^{\alpha} \tag{13a}$$

$$\sigma_{tot} = \sigma_{ref}\left(\frac{{v_r}^2}{{v_{r,ref}}^2}\right)^{-a} \tag{13b}$$

4.2.1 Parameter initialization

Based on the dynamics of the precursor gas as defined above, the Monte Carlo method was used to simulate the behavior of the precursor gas molecules from the GIS nozzle to the substrate surface. The flow chart of the precursor gas transfer simulation is shown in Fig. 35. First, we define the velocity distribution function of the participant gas molecule. The kinetic theory of gases is a theory that analyzes the behavior of a large number of small particles (or molecules) and deduces the properties of the whole gas from the results. All gas molecules are regarded to be randomly driven by the Maxwell Boltzmann distribution. The rapidly moving particles constantly collide with each other and with the inside wall of the nozzle. Kinetic theory describes the macroscopic properties of gases such as pressure, temperature and viscosity, taking into accounts the composition and motion of molecules. The Maxwell-Boltzmann distribution or Maxwell speed distribution describes particle speeds in idealized gases where the particle move freely inside of the stationary container without interacting with one another, except for very brief collisions in which they exchange energy and momentum with each other or with their thermal environment.

$$f(v) = \sqrt{\left(\frac{m}{2\pi kT}\right)^3}\, 4\pi v^2 e^{-\frac{mv^2}{2kT}} \tag{14}$$

Eq. (14) is the Maxwell-Boltzmann velocity function that is the basis of the kinetic theory of gas. From the above equation, the most probable velocity (C^*), mean velocity ($\bar{C}$), and RMS velocity (C_{RMS}) can be expressed by the following equations respectively.

$$C^* = \sqrt{\frac{2kT}{m}}, \quad \bar{C} = \sqrt{\frac{8RT}{\pi M}}, \quad C_{RMS} = \sqrt{\frac{3RT}{M}} \tag{15}$$

In general, the diameter of a molecule is not defined as a constant value but has different values depending on temperature and pressure. The radius of $W(CO)_6$, which is the precursor material used in this simulation, was covalent radius of W (146 pm), covalent radius of C (138 pm), covalent radius of O (73 pm), and Wan der Waals radius of O (152pm) were used. The molecular mass of $W(CO)_6$ was 5.84×10^{-25} kg. Mean free path (λ) and Knudsen number (K_n) were calculated using Eq. (6). The initial parameter values used in the simulation are shown in Table 5.

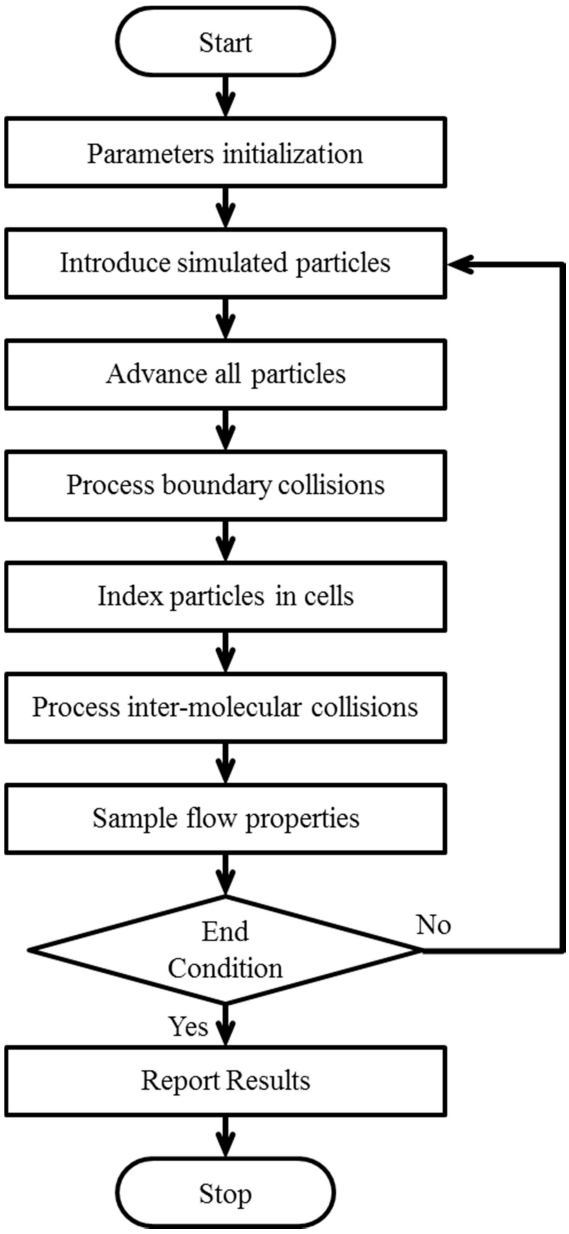

Figure 35 Flowchart of Monte Carlo simulation for precursor gas transfer in FIB-CVD process

Table 5 Definition of parameters for DSMC simulation

	Parameter		Dimension
Precursor	Name	$W(CO)_6$	
	Molecular diameter	1.29.E-09	m
	Molecular mass	5.84.E-25	kg/unit
	Flow Rate	1	g/Hour
		2.78.E-07	kg/sec
	Temperature	50	°C
		323	K
	Velocity	1.39.E+02	m/sec
	Density	1.01.E-02	kg/m^3
	Atomic density	1.74.E+22	$atoms/m^3$
	Mean free path	7.74.E-06	m
	Knudsen number(K_n)	1.55.E-02	-
Nozzle	Diameter	500	μm
	length	0.02	m
	Cross section	1.96.E-07	m^2
	inner volume	3.93.E-09	m^3
	Δvolume	1.52.E-12	m^3
	aspect ratio(L/d)	40	-
DSMC	FRACTION	1	
	scale X	7.74.E-06	m/cell
	scale Y	7.74.E-06	m/cell
	scale Z	3.87.E-05	m/cell
	cell number X	65	units
	cell number Y	65	units
	cell number Z	517	units
	time step	5.55.E-08	second
	No. of introduced at Δt	2.64.E+10	units
	proper # of particles in a cell	20	particles
	Expected # of particles in a cell	6.64.E+04	particles
	# representative	3.98.E+05	particles

4.2.2 Discretization of simulated space

In the simulation boundary, the inlet area of the nozzle into which particles are introduced is defined as a two-dimensional discretized space using a Cartesian grid. The physical coordinates representing the behavior of particles in the nozzle region and the discretized index coordinates for numerical computation are defined as shown in Fig. 36. The scale (δ) of a cell size is used as a fraction of λ, and generally values between 1/3 and 1/5 of λ are used. The Green-Kubo theory is used to evaluate the quadratic error of the cell size and time step. Time step, Δt, is $\frac{0.25 * \delta}{\bar{v}}$, which is the time at which the 25% distance of the cell can be moved at the average speed. The following equation is used to determine whether there is a collision between the molecule located at (x, y) on the physical space and the inner wall of the nozzle. Prior to the calculation, the position (x, y) in the physical coordinate system is transformed to the index coordinate system.

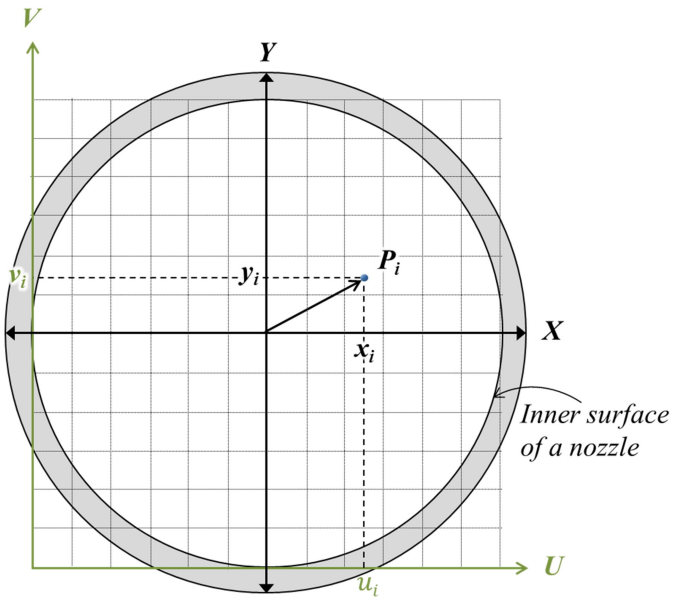

Figure 36 Discretized space for DSMC

$$I_x = (int)(\frac{x + radius}{\delta})$$
$$I_y = (int)(\frac{y + radius}{\delta}) \quad (16)$$
$$d = \sqrt{x^2 + y^2} > radius$$

4.2.3 Implementation of simulation

Once the discretized time and space domains have been defined for the location calculation of the participant particles in the physical space, define the number of particles introduced into the system at every time step. Since it is computationally impossible to simulate all precursor gas molecules as a single entity, it defines the number of precursor gas molecules (N_R) represented by a single simulation particle. In general, 20 particles in a cell are known as the rule of thumb. Therefore, if the

number of cells in the inlet of the nozzle is N_c, the number of simulated particles introduced at one time step can be calculated as follows.

$$n_s = \frac{20N_c}{\frac{\delta}{v\Delta t}} = \frac{20N_c v\Delta t}{\delta} \tag{17}$$

For example, assuming that the distance traveled during a time step at an average velocity of a particle is ¼ δ, there are five simulated particles entering each cell during one time step. Thus, the representative Number $\boldsymbol{N}_{\mathrm{R}}$ can be expressed as:

$$N_{in} = N_R n_s \quad \therefore \boldsymbol{N_R} = \frac{N_{in}}{n_s} \tag{18}$$

When the introduction operation for the simulated particles is completed in the step, boundary conditions must be defined. The type of boundary is defined as the exit boundary where the simulation particle is introduced, the surface boundary where the particle generates a collision while moving, and the tip part of the nozzle where the particle reaches the substrate through the ballistic motion inside the vacuum chamber.

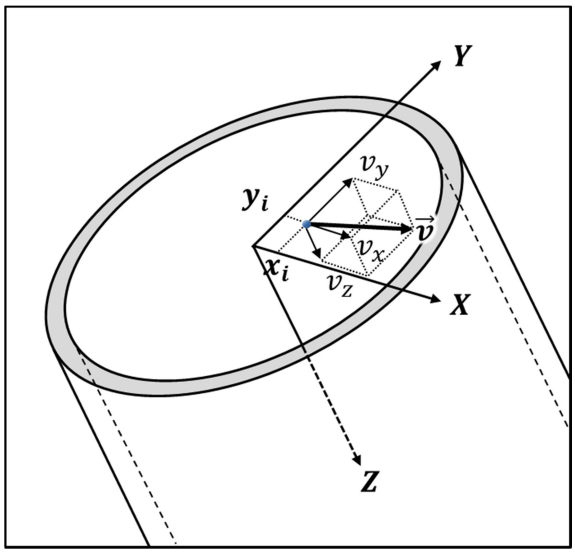

Figure 37 Illustration for the initial position and velocity of an introduced particle

The initial position and velocity of the particles introduced into the system are Eq. (16) and (17) using the Gaussian distribution. In the simulation, the following equation is used to assign the initial value of position and velocity of introduced particle.

$$\begin{aligned} \theta_p &= R_1 \times 2\pi R \\ r &= R_2 \times R \\ x &= r\cos\theta_p \\ y &= r\sin\theta_p \\ z &= 0 \end{aligned} \tag{19}$$

$$\begin{aligned} \theta_v &= R_3 \times 2\pi R \\ v_x &= R_4 \times \bar{C}\cos\theta_v \\ v_y &= R_5 \times \bar{C}\sin\theta_v \\ v_{z=}& \; 2R_5\bar{C} \end{aligned} \tag{20}$$

Here, R_1, R_2, R_3, R_4, and R_5 are random values having a value between 0 and 1. The simulated particles from the nozzle exit assume ballistic motion until it reaches the substrate past the inner space of the highly rarefied region of the FIB chamber.

With this assumption, in Fig. 35, four types of trajectories could be categorized. If the y-value (y_t) of the particle exceeds the nozzle length (l), it is considered to have come out of the nozzle. (3), (4) In this case, it is considered that there is no intermolecular collision in the vacuum chamber of high vacuum, (4) it is absorbed into the chamber or deposited on the substrate.

4.2.4 Results of the precursor gas transfer simulation

In this simulation, the behavior of the $W(CO)_6$ precursor gas until it reaches the surface through the nozzle is simulated. The parameters used in simulation are summarized in Table 5. The Knudsen value (K_n) of the precursor gas is 0.015. As a result, it was confirmed that the deposition is performed in the region of radius 700 μm based on the deposition peak as shown in Fig. 38. The simulation result was used for nozzle alignment of GIS.

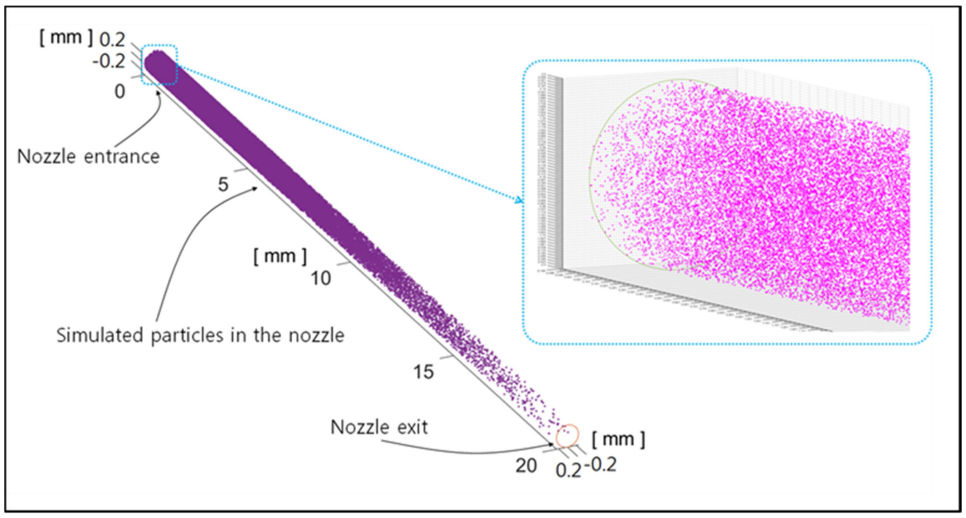

(a)

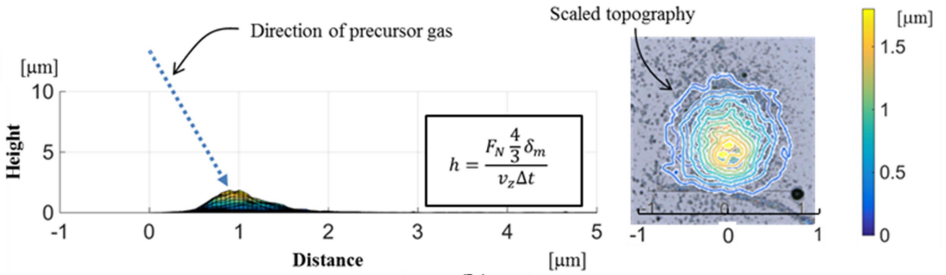

(b)

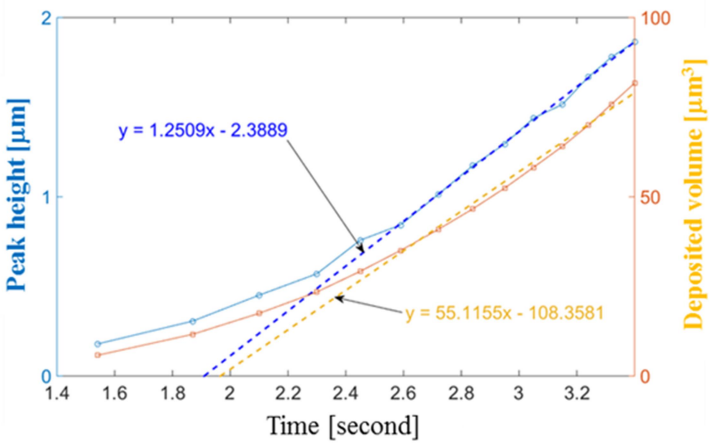

(c)

Figure 38 (a) The image showing the nozzle and the introduced particles while the simulation is running (b) the cross section and topography images of deposited material (c) Simulated results of peak height and deposited volume according to the deposition time

4.3 Simulation of FIB-CVD process

4.3.1 Simulation overview

The mechanisms of FIB-CVD and EBID are generally considered to reflect interactions between ions and solids, precursor molecules and the surface, and electrons and precursor molecules [23, 76]. Figure 2 illustrates the behavior of precursor gas molecules on the substrate surface used during FIB-CVD. Precursor gas molecules ejected from the nozzle tip of a gas injection system (GIS) reach their target surface on the substrate. Some precursor molecules are adsorbed to the surface, and these become the source of the deposition. Some adsorbed precursor molecules are decomposed by FIB, and some become naturally desorbed and move via surface diffusion.

As precursor molecules adsorbed on the surface constitute the depositional material, their distributions must be defined prior to analyzing the mechanism of deposition. Eq. (1) is the widely accepted distribution function for adsorbed precursor molecules and considers four physical phenomena affecting distribution. The terms on the right of Eq. (1) represent adsorption, desorption, dissociation, and diffusion, respectively. N(t,r) is the number of precursor molecules absorbed onto the surface; this depends on time and the distance from the center of the ion beam. The adsorption term is described by a sticking coefficient (s), the precursor gas flux (J), and the maximum number of molecules on the target surface. An adsorbed molecule spontaneously leaves the surface after a residence time (τD). The dissociation term, reflecting the consumption of molecules by deposition, is

defined by the dissociation cross-section (σ) and the ion flux distribution (f). Diffusion represents the movement of adsorbates along a density gradient on the surface. The diffusion coefficient D is related to the distance traveled by the adsorbates. All coefficients are dependent on process environmental parameters, such as temperature, local pressure, the precursor and substrate materials, and the operating conditions [23, 24]. Some authors have studied the effects of various experimental and simulated conditions on the coefficients [24, 73, 77-79]. As we here focus principally on simulation of evolutionary deposition over time, we do not discuss the characteristics of the coefficients in detail.

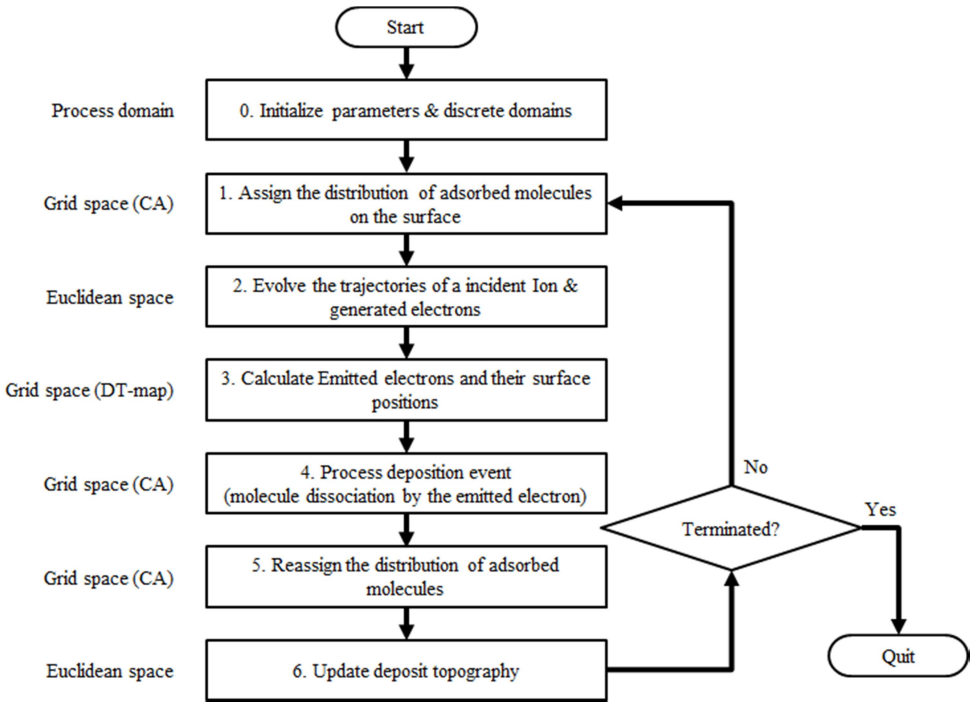

Figure 39 Overall flowchart of focused ion beam-induced chemical vapor deposition (FIB-CVD) simulation.

Figure 39 shows the overall flow chart of FIB-CVD simulation based on the direct simulation Monte Carlo (DSMC). First, the simulated region and the

coordinates of the physical and computational spaces are defined. In addition, the parameters and coefficients are initialized. The computational space is a discretized space with the same boundary as the physical space. Two grid spaces are defined in simulation. One is the cellular automata (CA) space used to identify the space occupied by the substrate and the dynamically evolving deposit in the system area. The other is the distance transform (DT) map. The DT map is a discretized space having the same size as the CA space. Each element of the DT map is associated with the Hausdorff distance (HD) reflecting the shortest distance to the surface. Once the discretization of the simulation space is complete, the next step is to distribute precursor molecules on the surface (thus, to model adsorption). In this step, the surface coverage (θ) is used as the reference when determining adsorption [24].

$$\theta = \frac{N}{N_0} = \frac{bJ}{1 + bJ} = \frac{\frac{sJ\tau_D}{N_0}}{1 + \frac{sJ\tau_D}{N_0}} \tag{21}$$

The trajectories of the incident ions and the generated electrons are simulated in the irradiation region. Numerical simulations of the FIB-CVD mechanism tend to employ EBID modeling because both models are often based on the hypothesis that reactions between emitted electrons and adsorbed, surface precursor molecules play essential roles in deposition. Electron collisions with solid surfaces have been continuously studied since the mid-20th century, creating the fundamental knowledge required to simulate electron trajectories in a given medium [25-29]. Simulation methods based on such fundamentals have been reported by a few authors. Representative simulation packages, namely SRIM/TRIM of Ziegler et al. [41, 42] and IONiSE of Ramchandra et al. [35], have

been widely used in FIB-CVD- and EBID-related research. To describe time-dependent deposition, real-time data on emitted electrons are required at every time step. Based on previous works [5, 26, 31, 34, 35], the simulation programs for charged particles, such as ions and electrons, have been customized to consider their trajectories. In this study, all simulations were implemented in C++.

To describe the trajectories of charged particles, scattering angle, step length, energy loss, and the number of electrons generated must be calculated for every scattering event. As the ions and electrons differ in terms of mass, energy, and charge, they move with different trajectories. Therefore, the trajectories must be simulated using different equations.

4.3.2 The trajectory of a primary ion

The ions injected into the substrate penetrate into the sample while colliding with the atoms of the substrate. When a collision occurs, the moving direction of an ion is changed and energy loss occurs. Some ions bounce out of the substrate due to collisions, and some ions penetrate into the substrate. The penetrating ions proceed by changing the path of travel by the continuous collision with the substrate atoms. When a collision occurs between the ions and the atoms of the specimen, the atoms may be sputtered or electrons emitted from the atoms depending on the energy of the ions. These phenomena become fundamental mechanism of subtractive process and additive process using FIB. When the energy of the ion is below a certain value, the trajectory of a ion is terminated. Since it is impossible to accurately describe the trajectory of the ion's progression, it is usually accessed in a probabilistic manner. Trajectories of ions moving inside the substrate are simulated using several

defined variables. First, we define a scattering angle that causes path changes when ion and atom of the substrate collide. Then, the energy lost in the collision and the energy transferred to the atom are defined. In addition, the average distance the ions travel before the next collision is described. These values are set to probability-based Gaussian random values to describe the overall trajectory of ion movement.

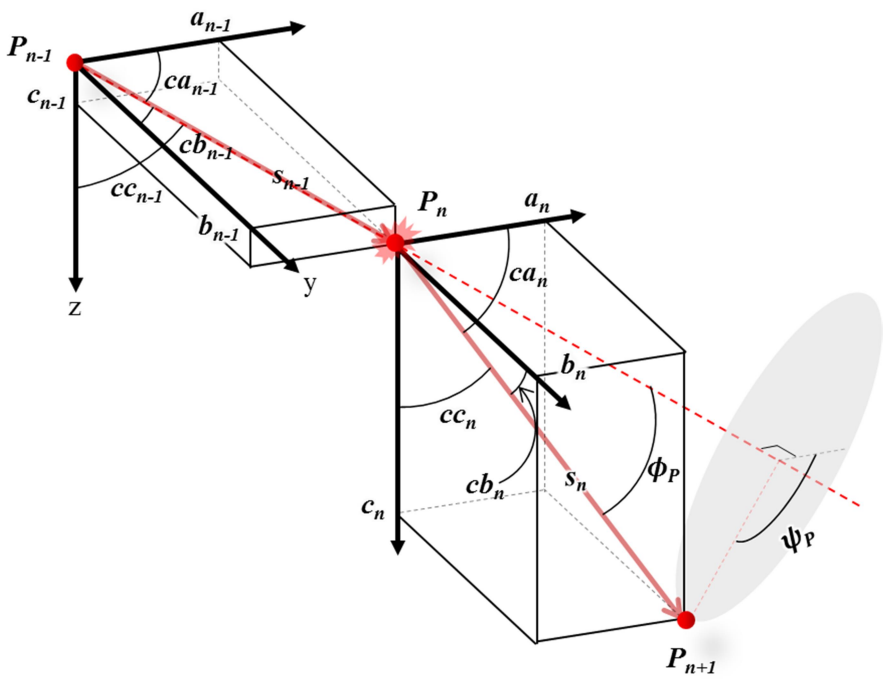

Figure 40 Illustration of an ion scattering inside the substrate[26]

4.3.2.1 Scattering of incident ion

Since the intensity of the ion beam depends on the Gaussian distribution having the maximum value in the center, it is assumed that the position of the primary ion on the surface of the substrate can be distributed according to the Gaussian distribution. In previous studies, the FWHM of the Ga + ion beam was set to 10 to

70 nm. Scattering angles are generally calculated using the unscreened Coulomb interatomic potential model or the Rutherford scattering model [24].

$$f(r) = f_0 e^{-\frac{r^2}{2a^2}} \tag{22}$$

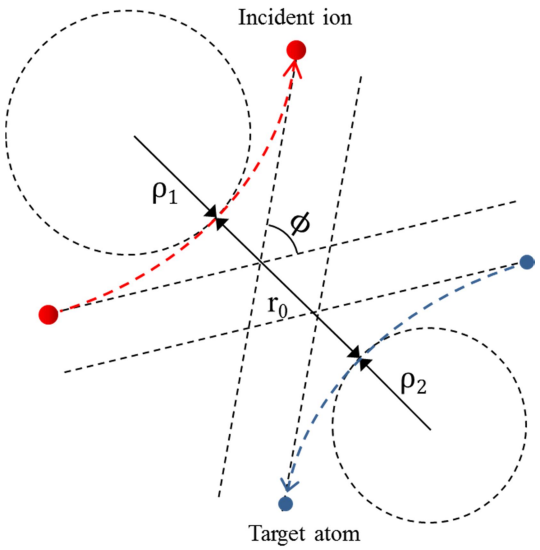

Figure 41 Schematic diagram of center mass scattering model [80]

As shown in Figure 41, the scattering between incident and target atoms is modeled as a collision between center mass objects. The scattering angle, ϕ, can be expressed as [28].

$$\cos\left(\frac{\phi}{2}\right) = \frac{B + R_C + \Delta}{R_0 + R_C} \tag{23}$$

In the above equation, B is a random variable, R_C, R_0 is a constant related to interatomic potential, and Δ is a fitting parameter. For convenience of calculation, the above equation is modified to be used as follows [28].

$$\sin^2\left(\frac{\phi}{2}\right) = \left[1 + (2\varepsilon B)^2\right]^{-1} \tag{24}$$

Where ε is a dimensionless value representing the energy that is reduced by the collision

$$\varepsilon = \frac{aE_c}{Z_1 Z_2 e^2} \tag{25}$$

Where Z_1 and Z_2 are the atomic number of incident ion and target atoms, a is the screening length, E_C is the energy available in the CM system, and e is the electronic charge. E_C can be expressed as atomic weight A_1, A_2 of incident ion and target material.

$$E_c = \frac{E}{1 + \frac{A_1}{A_2}} \tag{26}$$

Interatomic screening length, a, is defined as the atomic weight of collision atoms and the Bohr radius of hydrogen atom.

$$\begin{gathered} a = 0.8853 a_0 A^{-\frac{1}{3}} \\ A = (Z_1{}^{\frac{2}{3}} + Z_2{}^{\frac{2}{3}})^{\frac{3}{2}} \\ a_0 = 0.529 \times 10^{-8}\ [cm] \end{gathered} \tag{27}$$

Therefore, the value B related to the scattering conditions could be described by the impact parameter and the screening length as the following equation,

$$\begin{gathered} \mathrm{B} = \frac{P}{a} \\ \mathrm{P} = \left[\frac{RND}{\pi N^{\frac{2}{3}}}\right]^{\frac{1}{2}} \end{gathered} \tag{28}$$

Here N is the atomic density of the target material. The angle of azimuthal direction is determined by random value.

$$\psi = 2\pi \times RND \tag{29}$$

4.3.2.2 Scattering cross section of incident ion

The first thing to describe the scattering is to calculate the area of the scattering cross section where the incident ion is expected to collide as it passes through the

target material. This area uses the Lindhard, Nielson, Scharff (LNS) differential cross section model [29].

$$
\begin{gathered}
\mathrm{d}\sigma(\mathrm{E},\mathrm{T}) = \frac{1}{2}\pi a^2 \frac{E}{\gamma {E_L}^2} t^{-\frac{3}{2}} \mathrm{f}\left(t^{\frac{1}{2}}\right) dT \\
t = \frac{E^2}{{E_L}^2}\frac{T}{\gamma E} \\
\boldsymbol{\gamma = \frac{4A_1A_2}{(A_1+A_2)^2}} \\
E_L = Z_1 Z_2 \frac{e^2}{a}\frac{A_1+A_2}{A_2} \\
\mathrm{f}\left(t^{\frac{1}{2}}\right) = \Lambda t^{\frac{1}{6}}[1+\left(2\Lambda t^{\frac{2}{3}}\right)^{\frac{2}{3}}]^{-\frac{3}{2}}, \quad \Lambda = 1.309
\end{gathered}
\tag{30}
$$

In Eq. (30), *σ(E,T)* is the LNS cross section, a is the universal screening radius used previously, γ is the maximum ratio of the transfer energy transferred from the incident ion to the target atom by collision, and T is the transfer ion from the incident ion to the target atom by collision Energy. The Lindhard unit of energy E_L and the dimensionless value of energy loss ε can be expressed by the following equation [81].

$$
\begin{gathered}
\boldsymbol{E_L = 30.7356 \times \left(1+\frac{A_1}{A_2}\right) Z_1 Z_2 Y^{\frac{1}{3}} \quad [eV]} \\
Y^{\frac{1}{3}} = \left({Z_1}^{\frac{2}{3}} + {Z_2}^{\frac{2}{3}}\right)^{\frac{1}{2}}
\end{gathered}
\tag{31}
$$

$$
\varepsilon(\mathrm{E}) = \frac{E_c}{30.7356 Z_1 Z_2 Y^{\frac{1}{3}}} \tag{32}
$$

The function *f(t)* is the LNS cross section fitting function proposed by Winterbon et al. [82]. The simplification of the above equation by Thomas-Fermi approximation for computational efficiency is as follows.

$$\boldsymbol{\sigma_T(\mathrm{E}) = \frac{9}{2}\pi a^2 (2\lambda)^{\frac{1}{2}} \lambda W(q_1, q_2)}$$
$$W(q_1, q_2) = P(q_1) - P(q_2)$$
$$q_1 = (2\lambda)^{\frac{1}{6}} \left(\frac{ET}{\gamma {E_L}^2}\right)^{\frac{1}{9}} \tag{33}$$
$$q_2 = (2\lambda)^{\frac{1}{6}} \left(\frac{E}{E_L}\right)^{\frac{2}{9}}$$

Here, λ has a value of 1.309, and the following equation is applied according to the value of q.

$$if(q \leq 0.9) \quad \mathrm{P(q)} = P_L(q)$$
$$else \quad \mathrm{P(q)} = P_H(q)$$

$$P_L(q) = -1.6487831 - \sum_{n=0}^{\infty} \frac{(-1)^n (2n+1)!!}{2^n n!\,(4n-3)} q^{4n-3} \tag{34}$$
$$\mathrm{P}_H(q) = -0.10372089 + \sum_{n=0}^{\infty} \left[\frac{(4+3) \times \cdots \times (4n+3)}{4^n n!}\right] \frac{(1+q^4)^{-n-\frac{9}{4}}}{(4n+9)}$$

For reference, if q1 = 0.13165250 and q2 = 1.1917536, W (q1, q2) = 144.7177 [29].

4.3.2.3 Step length of an incident ion

To calculate the step length, the average free path that is expected to move until the next collision occurs after the collision must be calculated [29, 83].

$$\boldsymbol{\lambda = \frac{A_2}{N_A \rho \sigma_T}} \tag{35}$$

Where ρ is the density of the target material, N_A is Avogadro's Number, and A_2 is the molecular weight of a target atom. The step length is determined randomly with λ average. Thus, the probability that the step length becomes the distance δ can be expressed by the following equation.

$$P(s) = e^{-\frac{\delta}{\lambda}} \tag{36}$$

Therefore, the step length uses the randomized value as follows.

$$RND = \frac{\int_0^s e^{-\frac{s}{\lambda}} ds}{\int_0^\infty e^{-\frac{s}{\lambda}} ds} = (1 - e^{-\frac{s}{\lambda}})$$
$$\mathrm{S} = -\lambda \ln(1 - RND) = -\lambda \ln(RND) \tag{37}$$

4.3.2.4 Energy loss of incident ion

When the scattering angle and step length are calculated, the amount of energy that incident ions lose during movement is calculated. During ion movement, energy loss due to scattering and coulomb interference occurs constantly. If the energy of the ion becomes less than the minimum energy that keeps it moving, the trajectory is considered to be terminated. The energy of the incident ion is known to cause energy loss due to two collisions when moving the target material. The first collision defines the energy loss due to the elastic collision between the nuclear of the incident ion and the nuclear of the target atom. The other assumes energy loss due to electronic collision (inelastic collision), independent of energy loss due to nuclear collision. Therefore, the total energy loss can be defined as [28, 84].

$$\frac{dE}{ds} = \left(\frac{dE}{ds}\right)_n + \left(\frac{dE}{ds}\right)_e \tag{38}$$

Here, $\frac{dE}{ds}$ is the total energy loss rate [keV/cm], $\left(\frac{dE}{ds}\right)_n$ is the energy loss rate caused by nuclear collision, and, $\left(\frac{dE}{ds}\right)_e$ is the energy loss rate caused by electronic collision. Stopping cross section, energy loss rate, and energy loss are obtained from the following relationship.

$$\left(\frac{dE}{ds}\right) = NS(E)$$
$$\Delta E = S\left(\frac{dE}{ds}\right) \tag{39}$$

N is the atomic density, and S is the stopping cross section. S_n and S_e denote the stopping cross section of the nuclear collision and the electron cross section, respectively. The energy loss rate is calculated as the stopping cross section multiplied by the atomic density. The energy loss is calculated by multiplying the energy loss rate by the total trajectory S. The Ziegler, Biersack and Kittmark (ZBL) model is the model commonly used in stopping power calculations [31, 85].

$$S_n(E) = \frac{8.462 \times 10^{-15} Z_1 Z_2 A_1 S_n(\varepsilon)}{(A_1 + A_2)({Z_1}^{0.23} + {Z_2}^{0.23})} \quad [\frac{eVcm^2}{atom}] \tag{40}$$

Here,

$$\mathrm{S}_n(\varepsilon) = \begin{cases} \dfrac{0.5\ln(1 + 1.1383\varepsilon)}{(\varepsilon + 0.01321\varepsilon^{0.21226} + 0.1953\varepsilon^{0.5}} & \varepsilon \leq 30 \\ \dfrac{\ln \varepsilon}{2\varepsilon} & \varepsilon > 30 \end{cases} \tag{41}$$

$$\varepsilon(\mathrm{E}) = \frac{32.53 A_2 E}{Z_1 Z_2 (A_1 + A_2)({Z_1}^{0.23} + {Z_2}^{0.23})}$$

For example, for 30 keV Ga+ ion (Z_1=31, A_1=70) on Cu (Z_2=29, A_2=64), ε=0.1185, Sn(ε) =0.3259, thus Sn(E) = 2.96x10^{-13} [eVcm^2/atom], assume atomic density of Cu is 8.5x10^{22} atom/cm^3. Assuming the CM system, the energy loss due to the nuclear collision can be obtained by the following equation [28].

$$\mathbf{T} = (\Delta \mathbf{E})_{\boldsymbol{n}} = \frac{\boldsymbol{4 A_1 A_2}}{\boldsymbol{(A_1 + A_2)^2}} \mathbf{sin^2} \left(\frac{\boldsymbol{\phi}}{\mathbf{2}}\right) \boldsymbol{E} \tag{42}$$

Energy loss due to electronic interaction between the electron and the incident ion of the target atom should also be considered. Theoretical model (LSS model) proposed by Lindhard, Scharff, and Schiott is most often used for energy loss calculation by electronic stopping power [86]. LSS model is described as follows,

$$S_e(E) = kE^P \quad [\frac{eVcm^2}{atom}] \tag{43}$$

Where k is a velocity independent stopping parameter defined as [28].

$$\mathrm{k} = K_L = \frac{1.212 Z_1^{\frac{7}{6}} Z_2 \times 10^{-16}}{\left(Z_1^{\frac{2}{3}} + Z_2^{\frac{2}{3}}\right)^{\frac{3}{2}} A_1^{\frac{1}{2}}} \quad \left[eV^{\frac{1}{2}} cm^2 \right] \qquad (44)$$
$$p = 0.5$$

In the simulation, the energy loss of the primary ion is calculated every time the scattering is processed. And the electronic energy loss according to the path from the previous scattering point to the current scattering point, and the energy loss due to the nuclear collision caused by the scattering. The primary ion trajectory is regarded as being terminated when the energy is below 10 eV [28].

4.3.3 The trajectory of a secondary electron

4.3.3.1 Generation of secondary electron

Some of the energy lost by the collision with the target material is utilized as the excitation energy of the target atoms. Bethe's proposition has been widely used in the study of generation of secondary electron (SE). In Beth's study, the generation rate of the secondary electron was defined to be proportional to the stopping power of the collision moment. In other words,

$$\delta_{SE}(z, E) = -\frac{1}{\varepsilon}\frac{dE}{ds} \quad \left[\frac{\text{electrons}}{\text{ion particle}}\right] \qquad (45)$$

The constant ε is a parameter related to the energy required when secondary electrons are generated from the target atom. However, it has not been clearly defined yet. It is generally used as a tunable value to match simulation and experimental data. In this study, ε is the excitation energy of secondary electrons (SEs), and the values calculated by simulation in Yinghong Lin et al. [87].

Secondary electrons are generated from incident ion-solid scattering. Some of the lost ion energy is transferred to the secondary electron. This relationship is based on conservation of momentum and energy assuming electron-electron collision, but it is known to be reasonable for SE handling by ion scattering [34, 35]. Therefore, the initial energy of SE is calculated as follows.

$$\frac{d\sigma}{d\Omega} = \frac{\pi e^4}{E^2}\left(\frac{1}{\Omega^2} + \frac{1}{(1-\Omega)^2}\right) \tag{46}$$

$$E_{se} = \frac{\Omega E}{\delta_{SE}}$$

Ω is the scaling ratio transferred from the incident electron. If the ratio exceeds 0.5, the energy weight of the primary / secondary will change. Therefore, we apply the range constraint to have a cut off value of 0.001 or more without exceeding 0.5 [26].

$$\Omega = \frac{1}{1000 - 998RND} \tag{47}$$

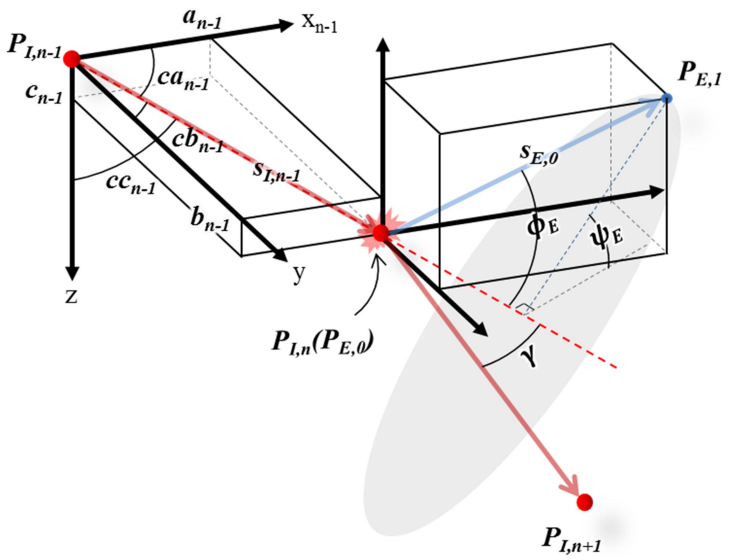

Figure 42 Illustration of the scattering of a generated SE [26]

4.3.3.2 Emission of a secondary electron

Some of the generated SEs dissipates in the bulk material, and some are emitted outside the surface. Scattering is divided into elastic and inelastic collisions. The secondary electrons are assumed to be generated when an elastic collision occurs.

The parameters such as step length, scattering angle and energy loss rate that have been defined to describe the trajectory of ions are used to simulate the trajectory of electrons as well. However, the values of the parameters are determined by other equations. These formulas have been developed on the basis of studies of atomic and electron collisions in the early 20th century. The scattering angle, step length, and energy loss of the SE were studied using the conventional electron beam scattering.

$$\boldsymbol{\lambda_e = \frac{A}{N_A \rho \sigma_E} \quad [cm]} \tag{48}$$

A: atomic weight of the target material

ρ: Density of the target

N_A: Avogadro's number

σ_E: Elastic cross section

The calculation of the elastic cross section of the SE is based on Rutherford's method [24, 76].

$$\sigma_E = 5.21 \times 10^{-21} \frac{Z^2}{E^2} \frac{4\pi}{\alpha(1+\alpha)} \left(\frac{E+511}{E+1024}\right)^2 \quad [cm^2/atom] \tag{49}$$

Z: atomic number of the target material

E: the energy of the incident electron in [KeV]

α: Screening factor

Here, the screening factor α takes into account the cloud of the orbiting electron of the target atom.

$$\alpha = 3.4 \times 10^{-3} \frac{Z^{0.67}}{E} \tag{50}$$

If the mean free path of the SE (λ_e) is calculated from the above equation, the step distance S_e uses a randomized value like the step distance of the ion.

$$S_e = -\lambda_e \ln(1 - RND) = -\lambda_e \ln(RND)$$

The scattering angle, φ, and ψ of SE use the following equations, respectively [26].

$$\cos(\phi) = 1 - \frac{2\alpha RND}{1 + \alpha - RND} \tag{51}$$
$$\psi = 2\pi \times \mathrm{RND}$$

A study on the energy rate lost when a SE goes through the path, in other words, the energy equation called the stopping power, was published by Bethe in 1930. The stopping power used in this study is as follows [88].

$$\frac{dE}{dS} = -78{,}500 \times \frac{Z}{AE} \times \ln\left(\frac{1.166(E + 0.85J)}{J}\right) \tag{52}$$

$$J = \left(9.76Z + \frac{58.5}{Z^{0.19}}\right) \times 10^{-3} \quad [keV]$$

The energy loss ΔE_{loss} of the incident electron via the distance s using the stopping power is calculated by the following equation.

$$\Delta E_{loss} = s\frac{dE}{dS}\rho \times 10^{-8} \quad [keV] \tag{53}$$

Among the SEs, only the SEs emitted from the surface of the substrate affect the deposition yield. Therefore, it determines whether or not the SE is emitted through the trajectory simulation of the SEs. Bruining proposed a method of calculating the emitted SE using a straight line approximation.

$$p(z) = 0.5e^{-\frac{Z}{\lambda_{esc}}} \tag{54}$$

Here *p(z)* is a probability function that calculates the probability that an electron will be emitted at a position z distant from the surface, and λ esc is an effective escape depth value described in Eq. (55).

$$\lambda_{esc} = \frac{750 \times {E_{SE}}^{1.66}}{\rho} \tag{55}$$

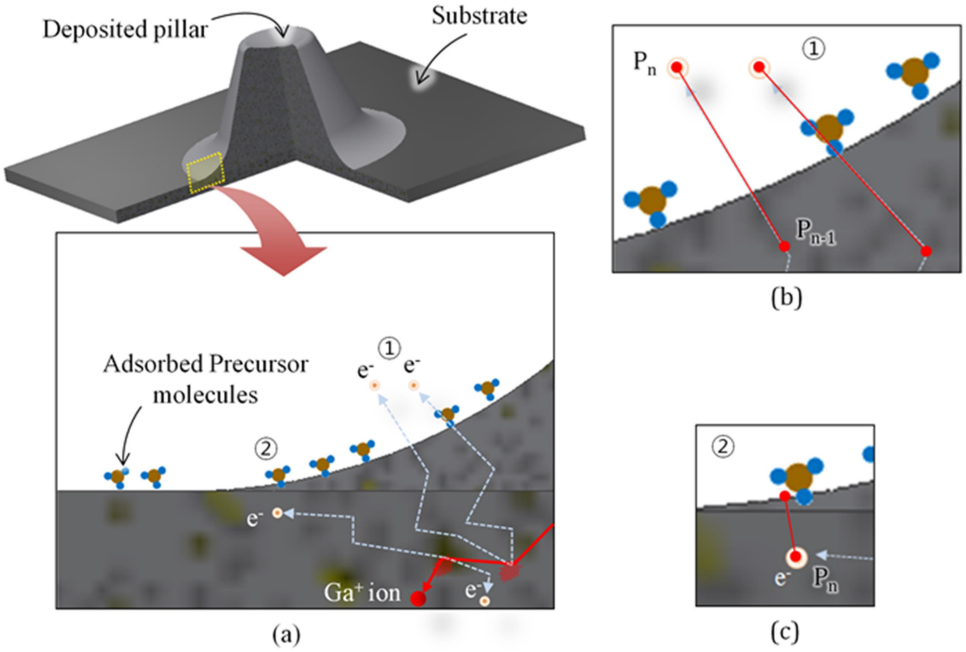

Figure 43 Illustration of (a) molecules adsorbed onto, and (b) electrons emitted from, the surface of the deposit and the substrate and (c) the collision between adsorbed molecule and emitted electron

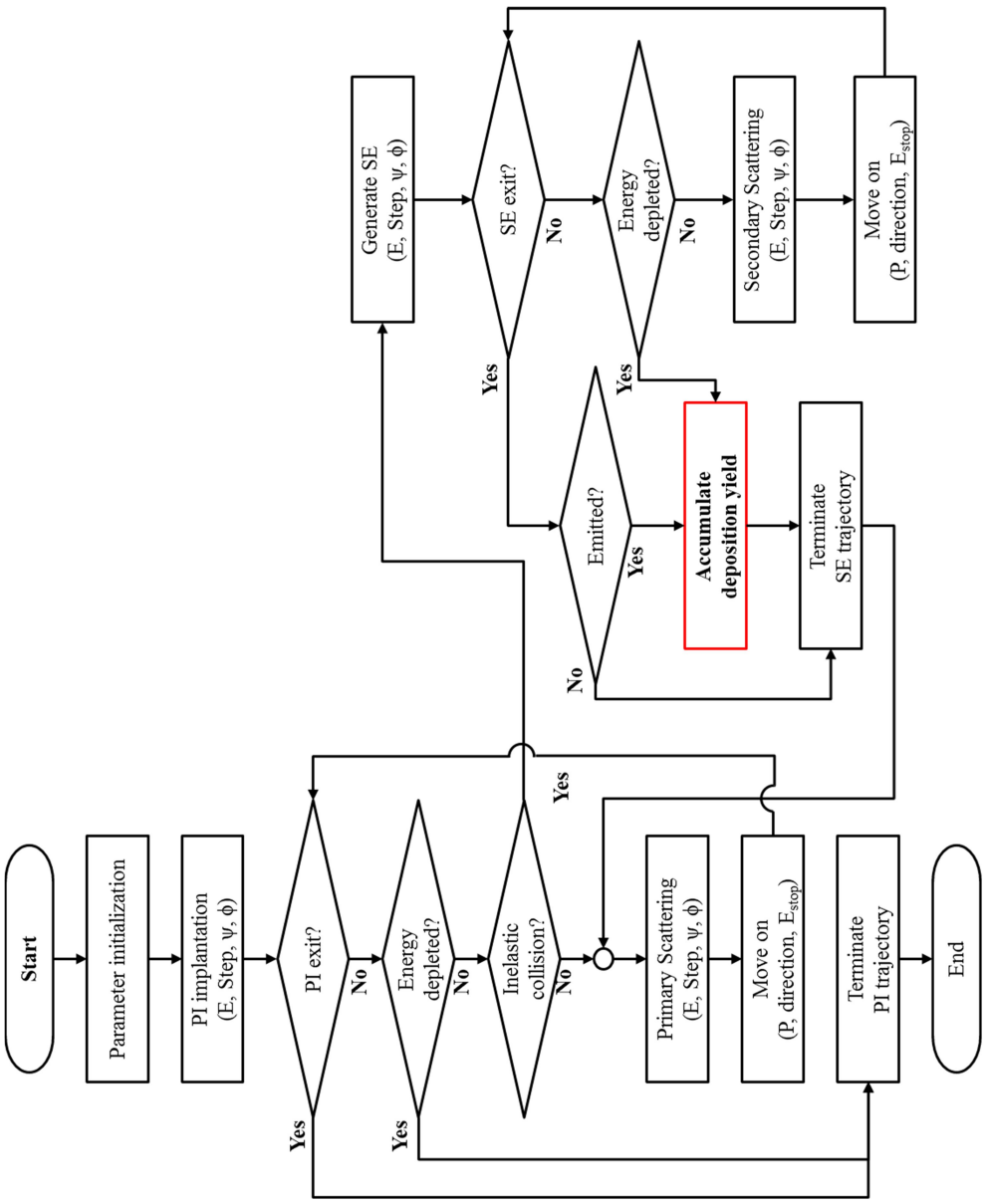

Figure 44 Flowchart for trajectories of single ion and secondary electrons

4.3.4 Dynamics of precursor molecules on the surface of substrate

4.3.4.1 Precursor adsorbate density distribution

Some of the precursor gas molecules from the GIS are absorbed on the target surface. Absorbed molecules move constantly while maintaining dynamic equilibrium state through adsorption, desorption, dissociation, and diffusion. The FIB-CVD undergoes a complex process consisting of interaction between ion-substrate, ion-electron and electron-adsorbate. For the simulation, the number of precursor gas molecules adsorbed on the target surface must first be calculated. We assume Langmuir isotherm for this calculation.

That is, assuming that the density of precursor molecules adsorbed on the surface has the same value in the distributed area at the same pressure and temperature and forms a single layer, the following equation can be obtained based on that assumption.

$$\frac{\Gamma_{gas}}{N_A}(molcm^{-2}s^{-1}) = \frac{P}{\sqrt{2\pi MRT}} \tag{56}$$

Where $\Gamma_{gas}$is the flux of the precursor gas, N_A is the Avogadro's number, M is the molecular weight of the precursor, P is the local pressure, and T is the temperature. Using the classical kinetic theory of a gas, the following equation can be obtained [44].

$$\Gamma_{gas} = \frac{P}{\sqrt{2\pi mkT}} \qquad (\#molecules \times cm^{-2}s^{-1})$$
$$n_{gas} = \Gamma_{gas} \times N_{site} \times \Delta x^2 \times \mathrm{t} \tag{57}$$

Where N_{site} is the number of total available gas surface sites on the surface, and Δx is the size of the cell element. $N_{site} \times \Delta x^2$ is the area of the deposition surface at

the current time. Using the above equation, we can define the molecule coverage, θ [24].

$$\theta(\mathrm{T}) = \frac{n_{gas}}{n_0} = \frac{b\Gamma_{gas}}{1 + b\Gamma_{gas}} = \frac{\frac{s\Gamma_{gas}\tau}{n_0}}{1 + \frac{s\Gamma_{gas}\tau}{n_0}} \tag{58}$$

Where b is the temperature dependent thermodynamic parameter, τ is the residence time, ***s*** is the sticking parameter, and $\boldsymbol{n_0}$ is the maximum number of adsorption sites. Residence time has a temperature dependency and has the following relationship.

$$\tau(\mathrm{T}) = \tau_0 e^{\frac{E_{des}}{kT}} \tag{59}$$

Here E_{des} is activation desorption energy. The higher the temperature, the shorter the time the precursor molecules stay on the surface. However, the values of the residence time (τ) and the sticking coefficient (s) are unknown and have a dependent value depending on the target material and experimental parameters. In the simulation, the molecule is randomly placed on the surface site according to the precursor molecule coverage value.

4.3.4.2 Diffusion model of the adsorbed molecules

Many researchers working on EBID and FIB-CVD have studied the effect of the surface diffusion behavior of the absorbed precursor molecules on the deposition rate. Much research has been done on the deposition topography and growth rate of micro or nanoscale. In general, surface diffusion depends on temperature and can be expressed as.

$$\mathrm{s}_d = (Dt)^{\frac{1}{2}} \tag{60}$$
$$D(T) = D_0 e^{-\frac{E_{diff}}{kT}}$$

Here E_{diff} is activation energy for adsorbate, D_0 is a material-dependent constant,

and generally has a value in the range of 10^{-2} to 10^{-3} cm^2/sec. For reference, Daryl A Smith et al. used a diffusion constant value of 10^{-8} to 10^{-11} cm^2/sec in his study to simulate the effect of diffusion on deposition in EBID [79]. The interaction between the precursor molecule and surface mentioned above changes in real time by adsorption, desorption, dissociation, and diffusion, which is generally defined in Eq. (1).

4.3.4.3 Dissociation model of the adsorbed molecules

Once the precursor molecules were distributed on the surface of the substrate and deposit, the decomposition process with the emitted SE is processed. In the deposition process model, first, the dissociation cross section, in which the single emitted SE affects the deposition, is defined. A dissociation cross-section refers to the effective area where decomposition occurs when emitted SE collides with an adsorbed gas molecule. This region is dependent on the molecule material and the electron energy. It is difficult to find the results of the study on the precursor phenanthrene ($C_{14}H_{10}$) used as a precursor material in this study. However, the Alman summarized empirical formulas through extensive experiments on the dissociation cross section of hydrocarbon [89]. This study, simulation was conducted using the laboratory presented by Alman.

$$\sigma(E) = \begin{cases} 0 & ,for\ E < E_{th} \\ \sigma_{max}\left[1 - \dfrac{(E_{max} - E)^2}{(E_{max} - E_{th})^2}\right] & ,for\ E_{th} < E < E_{max} \\ \sigma_{max} e^{-\frac{(E - E_{max})}{\lambda}} & ,for\ E > E_{max} \end{cases} \quad (61)$$

Where E is the energy of the secondary electron, E_{th} is the threshold energy for dissociation, E_{max} is the maximum energy at which the maximum dissociation cross-section, σ_{max} is the maximum dissociation cross-section, and λ is the constant

that determines the rate of decay of the cross section. In his work he found that the E_{th} value for most hydrocarbons was maintained at 10 eV, but instead the E_{max} value suggested the following relationship:

$$\begin{aligned} \mathrm{E}_{max} &= (7.71\ eV)C + (1.31eV)H + 67.0\ [eV] \\ \sigma_{max} &= (1.89C + 0.33H - 0.505) \times 10^{-16}\ [cm^2] \\ \lambda &= -(64.3739eV)C + (35.3963eV)H + 668.358\ [eV] \end{aligned} \tag{62}$$

Where C is the number of carbon and H is the number of hydrogen. Using Eq. (62), E_{max}, σ_{max} and λ of phenanthrene could be calculated respectively as follows.

$$\begin{aligned} \mathrm{E}_{max} &= 188.04\ eV \\ \sigma_{max} &= 0.293\ nm^2 \\ \lambda &= 122.09\ eV \end{aligned}$$

Once the dissociation cross section ($\sigma(E)$) has been calculated, the value is used to calculate the probability that the adsorbate will decompose by collision of the emitted SE. If the adsorbate is present in the cell of the discretized surface through which the emitted SE passes, the decomposition probability can be calculated as [5].

$$\mathrm{Q} = \frac{\theta S_{\rho}}{n_{PE}} \int_{E_l}^{E_f} n_x(x, E)\sigma(E)dE \tag{63}$$

Where $n_x(x, E)$ is the electron energy distribution, θ is the precursor adsorbate coverage, and $\boldsymbol{s_{\rho}}$ is the atomic surface density. The above equation can be modified briefly as [5].

$$\mathrm{Q}' = \frac{\sigma(E)S_{FCC}}{A_m} \tag{64}$$

S_{FCC} is the face centered cubic (FCC) planar density (2π/8) and $\boldsymbol{A_m}$ is the molecular cross section area. In the simulation, the decomposition event can be randomized into the following equation.

$$\textbf{If } \mathrm{RND} < \mathrm{Q}' \;\&\&\; gas\ present\ \boldsymbol{then}\ deposit\ material$$

4.3.5 Cellular automata model for evolution of deposition

A cellular automata (CA) is a discrete modeling method that enables to analyze the characteristics of the whole system by processing the state transitions in a single cell. A CA method basically operates by states and transition rules. The state of the cell represents the physical characteristics of cell in the simulated system, and transition rule defines the events that result in the change of the state by adjacent cells called neighborhood. The basic process mechanism of FIB-CVD is the process in which the emitted SE deposits the non-volatile component by decomposing the adsorbate precursor molecule on the surface. Simulation using a numerical method for transforming continuous physical space into discretized computational space is suitable for studying the evolution of deposition by applying the cellular automata concept. For the adaptation of CA method in this study, four states were defined by conceptual approach: vacuum, molecule, surface, and solid. Conceptually, vacuum state refers to empty space, which is the state of a cell that has not yet been stacked in system space. The molecule state is the state of the cell that is likely to be adsorbed by the precursor molecule as the state of the cell that contacts the surface cell in the vacuum cell. Therefore, the number of molecule cells is used to calculate the adsorbate density coverage. The surface state is the state of the cell between the molecule cell and the solid cell, which represents the surface of the deposit evolving every hour and is the basis for finding the molecule cell. The solid state is a state in which a surface cell is generated by transitioning to a state that transitions when a deposition event occurs in a

neighboring molecule cell of a surface cell and is no longer adjacent to a vacuum cell.

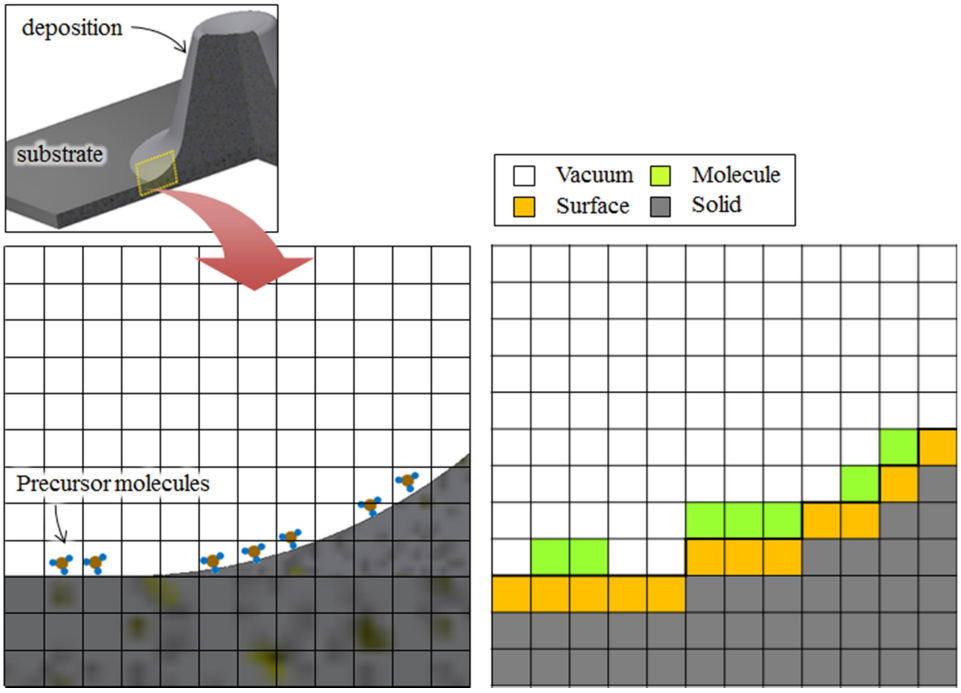

Figure 45 State types of CA model

A vacuum state refers to a vacant space around a substrate in a vacuum chamber. If a vacuum cell adsorbs precursor molecule, then the state transitions to the molecule. A molecule state is the state of the cell that adsorbs a precursor molecule. If a deposition event takes place in a molecule cell, the molecule state of the cell transitions to the surface state. A surface state represents the surface of the substrate and deposition that topography evolves in every step time. The combination of the cells in surface state, therefore, means deposition topography at that moment. A substrate cell is also the reference cell to decide the molecule cell when the distribution of the precursor molecules on the surface is processed. If a molecule cell adjacent to a certain surface cell becomes a surface cell, which the

certain surface cell has no neighborhood in vacuum or molecule cell, then the surface state of the certain cell transitions to the solid state. A solid state means solid material of the substrate and the deposit. A solid state becomes the medium of the scattering of ions and electrons, and does not participate in deposition process.

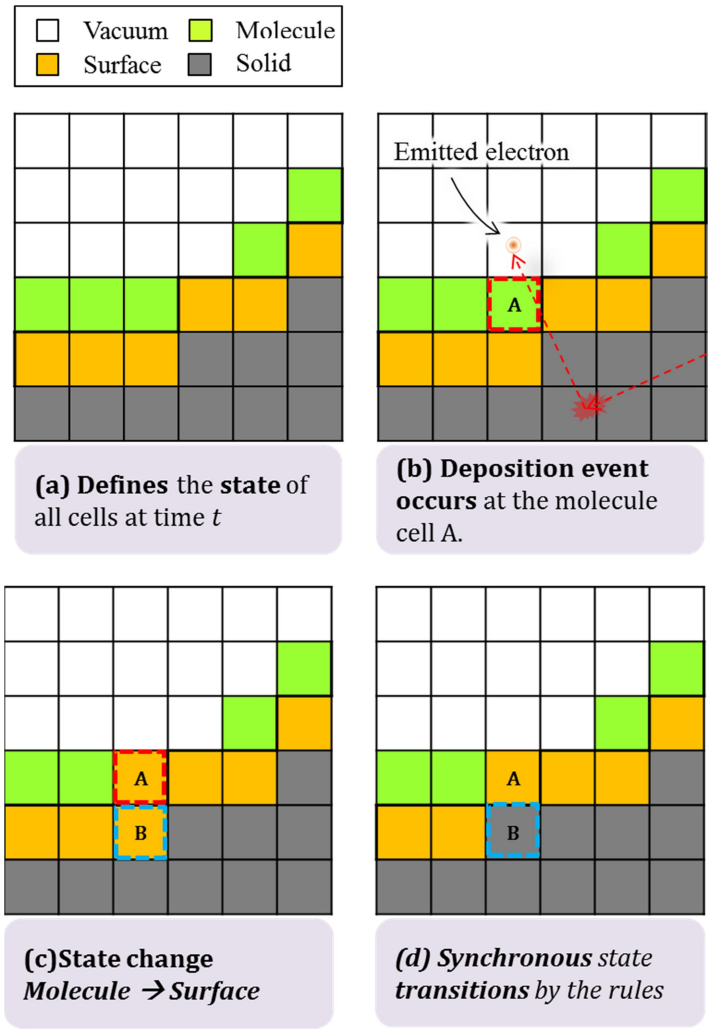

Figure 46 Schematic depiction of state transition

A discretization of space in the simulated region was carried out to adapt the MC method, CA space, and DT-map. In this study, the time dependent dynamic topography of a deposition induced by the spot-radiated ion beam was considered

as the simulation target. The pillar deposited by stationary spot FIB was assumed to be radially symmetric. Based on the assumption 3D physical space in Cartesian coordinate can be transferred to the 2D discretized domain in r, z coordinate. The cell size of the grid was determined based on the atomic surface density [5]. The atomic surface density was derived based on the material density(ρ) of the amorphous carbon pillar that was deposited using FIB-CVD by Igaki et al. [72]. The size of a cell in x, y direction is equivalent to the distance (l_{atom}) between adjacent atoms.

$$l_{atom} = \left(\frac{1}{s_\rho}\right)^{\frac{1}{2}} \tag{65}$$

Where s_ρ is the average atomic surface density of the deposit and the density value of the deposit is the result of Chung-Soo Kim et al. The above equation can be modified as follows [90].

$$l_{atom} = \frac{\rho N_A}{A}^{-\frac{1}{3}} \tag{66}$$

Assuming that the density of the carbon deposit is 3.1 kg/cm^3, the l_{atom} value calculated using the above equation is 0.186 nm. Therefore, the size Δx and Δy of the cell to be used for the simulation are used as these values. Based on the experiment, the size of cell grid was defined as 600x600, which covered about 112nm in vertical direction and 223nm in lateral direction.

4.3.6 Hausdorff distance transformation

The Hausdorff distance transform (HDT) is a numerical method that transforms the distances of two objects lying in the Euclidean space so that they can be quickly

inferred through a numerical approximation [91]. The Hausdorff distance (HD) map has a digitized distance value where each element in the grid domain represents a minimum distance from a particular location. The HDT is mainly used to find similarities in distance or shape between two subsets in applications such as recognition and tracking in image processing. In this paper, we applied the Hausdorff distance transform for fast processing when calculating the emission probability of electrons generated by scattering. IF the surface emission position is sought without a HDT-map, we must find the surface vector normal to the electron position, and calculate the Euclidean distance. Such processing of all electrons on a surface that varies over time is computationally very costly; previous works sought to utilize continuum models to this end or made additional assumptions. However, using a DT-map, such complex computations are simply replaced by the pixel values of the DT-map. However, there is no research result when the method is required to calculate the topography of the surface in real time such as CVD simulation. Figure 47 illustrates the drawing process of the HDT map. First, the edge region is extracted from the image as shown in Fig. 47 (b). In this case, the surface area of the substrate and the deposit is regarded as an edge regime. If the edge image is extracted, the distance value of each pixel is initialized. As shown in Fig. 47 (c), the edge pixel is set to 0, which means the shortest distance to the edge itself, and all other pixels are initialized to the maximum value (M). Finally, HDT is performed on the initialized map using the chamfer matrix shown in Fig. 47 and Eq. (67) and (68). The result is shown in Fig. 47 (d). In the figure, a pixel representing a surface has a distance value of 0, and a pixel farther from the surface has a larger distance value. This value is the numerically quantized value of the

shortest distance to the surface. Using this map, the shortest distance from the specific position to the surface can be calculated without Euclidean distance calculation.

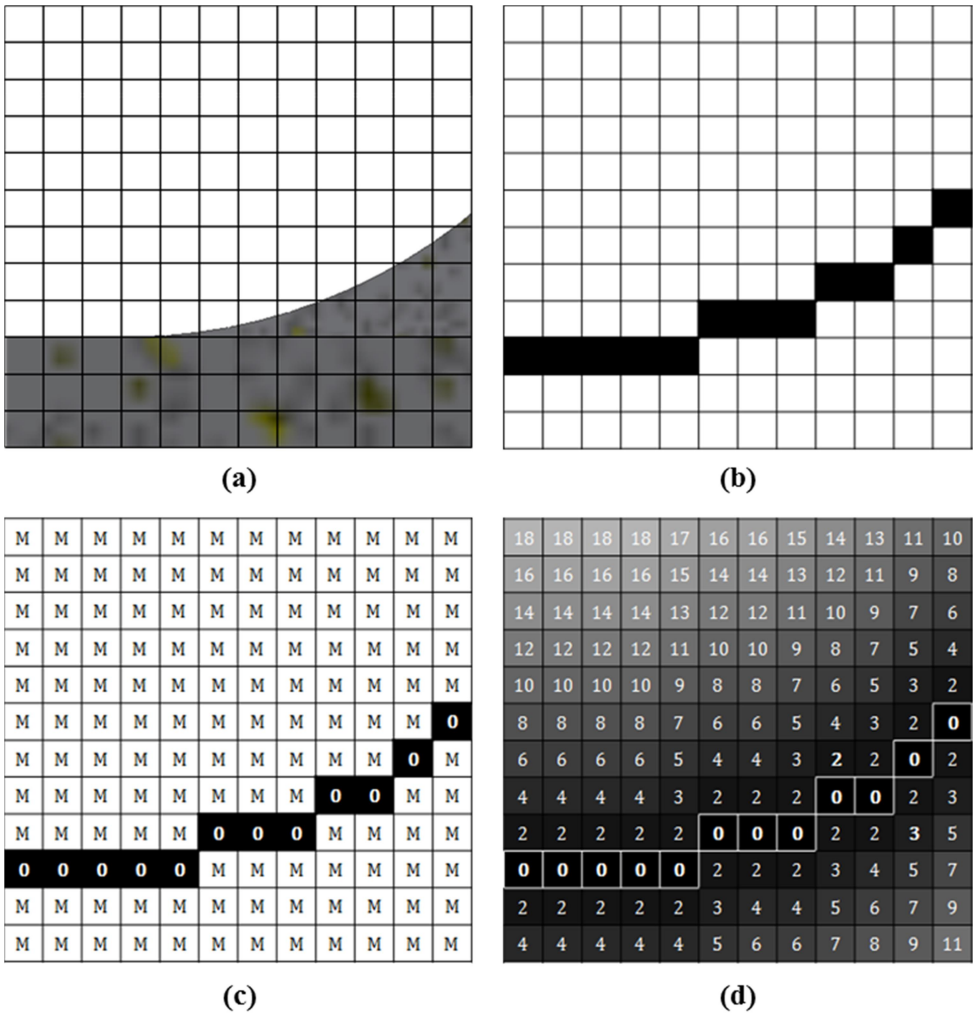

Figure 47 Adaptation of Hausdorff distance (HD) transformation in the simulation area

The calculating the minimum distance from the scattered position where the SE is generated to the shortest molecule cell using the distance transformation map is shown in Figure 48. First, we get simulated instantaneous deposition topography at a specific point in time. If the position of the molecule cell is defined, the

distance value of the position is defined as 0 in the HDT map and the remaining value is assigned as the maximum value (M) shown in Fig. 46 (b). Binary distance map consisting of 0 and M becomes input data for the HDT map. Once the binary distance map is prepared, perform a forward DT transformation and a backward DT transformation. The method of implementation is as follows. A map such as Fig. 46 (d) is created by the HDT using the following equation.

$$D_H(A,B) = max\left\{\underset{a\in A}{max}\left(\underset{b\in B}{min}\, d(a,b)\right), \underset{b\in B}{max}\left(\underset{a\in A}{min}\, d(a,b)\right)\right\} \quad (67)$$

A DT map is a mode of implementation of the HD within a discrete domain. In a DT map, every pixel is associated with a distance from its position to the nearest surface edge. A DT map was calculated using the kernel function of the 2–3-chamfer matrix shown in Fig. 48.

$$d^k_{(i,j)} = min\begin{bmatrix} d^{k-1}_{(i-1,j-1)}+\alpha & d^{k-1}_{(i,j-1)}+\beta & d^{k-1}_{(i+1,j-1)}+\alpha \\ d^{k-1}_{(i-1,j)}+\beta & d^{k-1}_{(i,j)}+0 & d^{k-1}_{(i+1,j)}+\beta \\ d^{k-1}_{(i-1,j+1)}+\alpha & d^{k-1}_{(i,j+1)}+\beta & d^{k-1}_{(i+1,j+1)}+\alpha \end{bmatrix} \quad (68)$$

$$\alpha = 3, \beta = 2$$

Where the superscripts indicate the iteration orders, and the subscripts *i, j* the index of the pixel in the x, y direction, respectively.

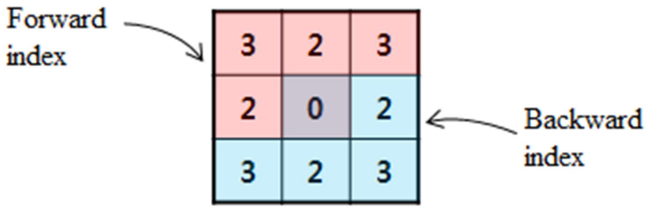

Figure 48 Chamfer matrix for HD transformation

Once the DT map is complete, locate the scattered electrons in the simulation domain and read the pixel value corresponding to that position in the

DT map. For example, in Figure 48, the DT value at the location where the emitted SE is 3. That is, the distance value corresponding to the minimum distance from the position to the molecule cell is 3, and this value can be converted into the distance in the physical domain.

$$s_{(i,j)} = d_{(i,j)} \times \delta \tag{69}$$

Using this method, the position and distance on the surface to which the straight line approximation is applied can be calculated effectively when the emitted SE finishes trajectory inside the substrate material or passes outside the surface. In this example, the shortest distance to the surface from the emitted electron ② positions of P_{n-1} and P_n are 3×δ(0.186 nm) = 0.558 nm, and 0.372 nm, respectively. Thus, the distance calculation process features only multiplication of the map distance value by the scale. The maximum accuracy loss is less than the scale of the pixel, thus almost negligible.

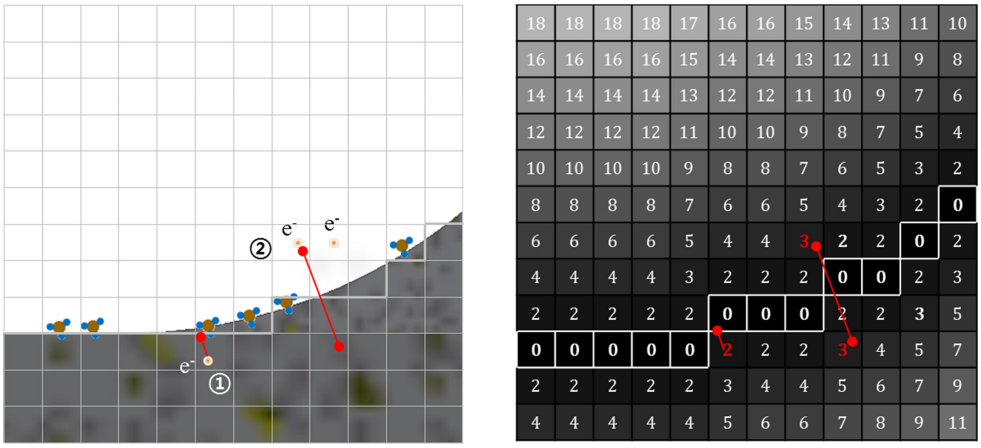

Figure 49 Example of how to get the distance between emitted electrons and the surface

4.3.7 Simulation of FIB-CVD process

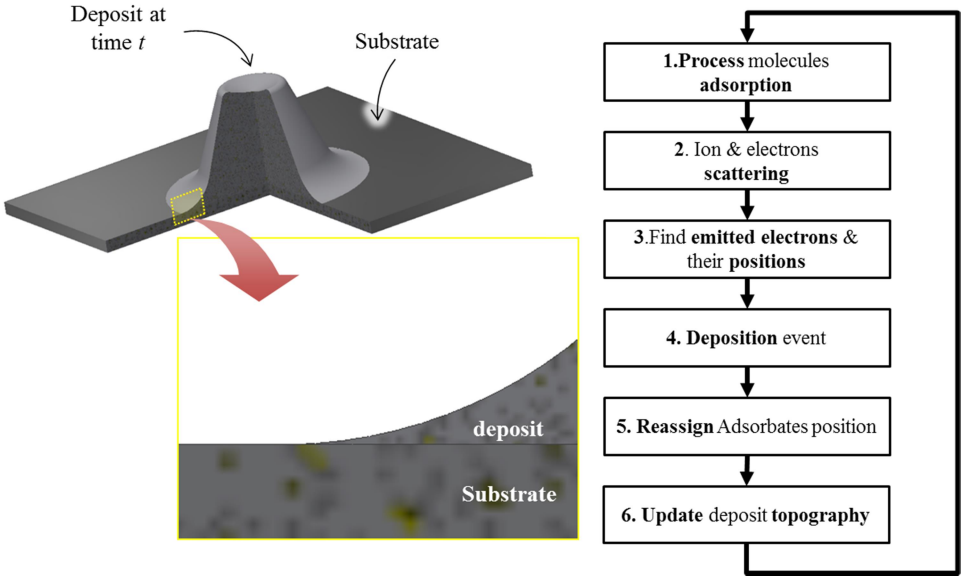

Figure 50 Overall flowchart of simulation for FIB-CVD process

The schematic sequence for the simulation of the FIB-CVD process is shown in Fig. 50. The first step is to distribute the precursor gas molecules on the surface based on the surface-molecule coverage defined in Eq. (21). The next step is to simulate the trajectory of a single primary ion impinging on the target material from the ion gun on the physical domain. When scattering occurs on the move, the location and the number of generated SEs and their respective energies are stored in the data. When the trajectory of the primary ion is terminated, the cell grid for the cellular automata process is generated based on the deposition topography calculated in the previous time step and the state is defined according to the deposition topography and the molecule distribution. Then, prepare a DT map of the same grid size as the CA grid and complete the DT map as described above. The shortest distance between the SE and the surface and the position through

which the SE passes can be obtained using the DT drawn in the previous step. Whether the precursor molecule is dissociated depends on the dissociation probability function. If the molecule is determined to be dissociated, this result is stored and accumulated in the current deposition result. This process is performed on all emitted SEs at that time step to calculate the amount deposited at the current step.

When the precursor molecule adsorbed on the surface is decomposed by the emitted SE, a new molecule is replenished at the position where deposition is carried out. The probability of these two cases is determined by the local pressure and the precursor temperature, respectively. In simulation, deposition evolution is based on every primary ion. One cycle is defined as processing the emitted SE by a single incident ion and processing the deposition process according to the emitted SE. At this time, the adsorption is processed in the unit of primary ion, and the diffusion is processed in the unit of emitted SE. That is, when deposition occurs in the corresponding cell by SE, diffusion is used to reassign the position of the adsorbate. After one cycle of treatment, the adsorbate is assigned to the cell by adsorption again. The displacement of the adsorbate by diffusion is calculated by the following equation, assuming Brownian motion by random work [79].

$$\mathrm{d} = \mathrm{k}\sqrt{4D_{surf}t} \tag{70}$$

Here, D_{surf} is a temperature dependent diffusion constant, which can be described by the following equation [24].

$$\mathrm{D}_{surf} = D_0 e^{-\frac{E_{diff}}{kT}} \tag{71}$$

D_0 is the value in order of about 10^{-2} to 10^{-3} cm^2/sec, and the above two equations

can be defined by the following equation.

$$\mathrm{d} = \mathrm{C}_1 e^{-\frac{C_2}{2T}} \tag{72}$$

That is, the diffusion displacement is proportional to the value of $e^{-\frac{1}{T}}$ of temperature. In the simulation, the constants are defined and used according to the temperature of the precursor temperature. Generally, D_{surf} is a value that varies depending on adsorbate and surface type and temperature, and it is generally known to have a value in the order of 10^{-10} to 10^{-7} cm^2/sec, which is calculated based on empirical values [24, 51]. In this study, the following diffusion coefficient equations were obtained by applying D_0 to 2.0×10^{-2} cm^2/sec and diffusion size d to cell size 0.186 nm

$$\mathrm{d(T)} = 1.0 \times 10^{12} e^{-\frac{10054.37}{T}} \quad [nm] \tag{73}$$

In this study, a focused ion beam of 30 keV, 20 pA was used. Since the charge of a single electron is approximately 1.602×10^{-19}C, the number of Ga^+ ions bombarded on the substrate is approximately 1.250×10^{8}. Ion is assumed to be incident on the surface as a Gaussian distribution, and FWHM is 10 nm. Based on this assumption, the time between ions was calculated to be about 0.8 μsec, and the number of emitted SE was calculated based on the above values.

Figure 51 depicts the steps in which deposition takes place in terms of precursor gas molecules. First, the precursor gas molecules are randomly distributed on the surface based on the surface-molecule coverage (Fig. 51 (a)). Next, the trajectories of the electrons are simulated, the electrons emitted from the entire traveling electrons are selected, and the positions of the emitted electrons are recorded (Fig. 51 (b)). In the CA grid, dissociation events are generated by using

the dissociation probability function to find the molecule state cells where the electrons are emitted (Fig. 51 (c) and (d)). If a dissociation event occurs, the result is stored in the corresponding cell and reflected in the surface calculation at the next time step ((Fig. 51 (e) and (f)).

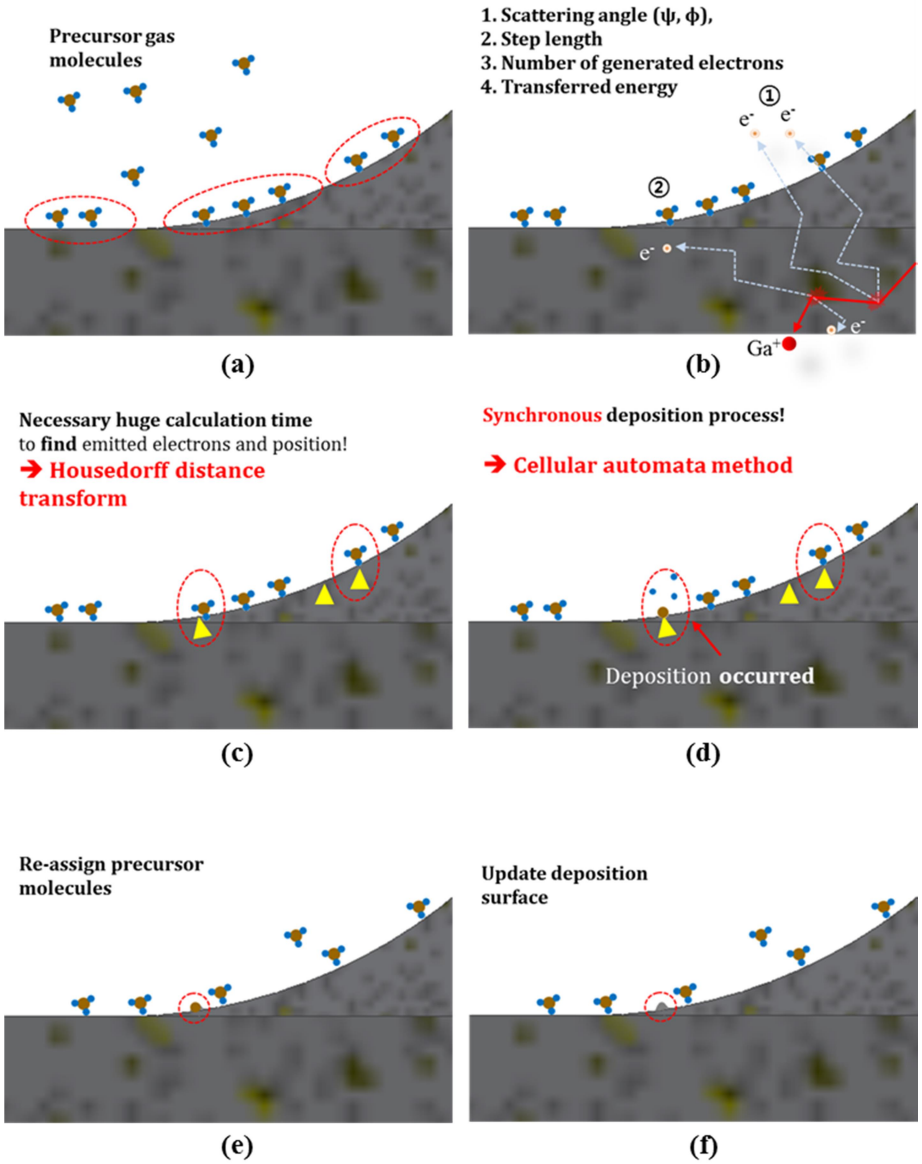

Figure 51 Illustration of the steps of FIB-CVD process from a molecular point of view

4.3.8 Results of the simulation

4.3.8.1 Trajectories of ion and electron

The simulation was implemented in C ++ and simulated. The input parameters are in Table 6.

Table 6 Initial parameter of FIB-CVD simulation

	Parameter	**value**
Z_1	Atomic number of Ga+ ion	31
A_1	Atomic weight of Ga+ ion [g/mol]	70
Z_2	Atomic number of Si substrate	14
A_2	Atomic weight of Si substrate [g/mol]	28
Z_3	Atomic number of C	6
A_3	Atomic weight of C [g/mol]	12
E_0	Beam energy [eV]	30000
I_0	Beam current [pA]	20
FWHM	FWHM of FIB	10
ρ	Material density of Si substrate	2.329
E_c	Cut off energy of ion [eV]	500
T_p	Temperature of precursor gas [°C]	70, 75, 80, 85

Figure 52 show the results of scattering simulation of 1000 ions in Si substrate under given conditions in Table 6. Figure 52 (a) shows the trajectories of the ions and Fig. 52 (b) shows the positions of the ions when their trajectories were terminated. The terminal positions of some ions were observed inside the substrate,

but some were shown outside the substrate by backscattering. SRIM-based Envizion is widely used as a tool for simulating trajectory of ion and electron [78]. In comparison with simulation results of this study and previous research results, it is difficult to directly compare the ion beam condition and substrate material type. However, comparing the range and depth of influence of ion, it could be considered that the trajectory and the scattered range of ions and electrons in this study tend to be similar to other researcher's studies [14, 32, 34]. Figure 53 shows the trajectory of 756 secondary electrons generated by the incident ion. Since the electrons are generated at the position where the substrate material atom and the scattering occur, the starting position differs depending on the electron. And it can be confirmed that it moves to a wider area than ion.

Ga^+ ion beam with 30keV and 20pA was used for the deposition. The FWHM of the beam was about 20nm. As a simulation result, the trajectory of ion was calculated to penetrate to about 50 nm depth in Si substrate. In the case of an electron trajectory, because it is generated inside the substrate and has a large mean free path compared to the ion, the penetration depth and range were observed deeper and wider than those of ion. This in house simulation software were used to simulate the dissociation events of the precursor gas molecules absorbed on the surface and utilized for the FIB-CVD process simulation.

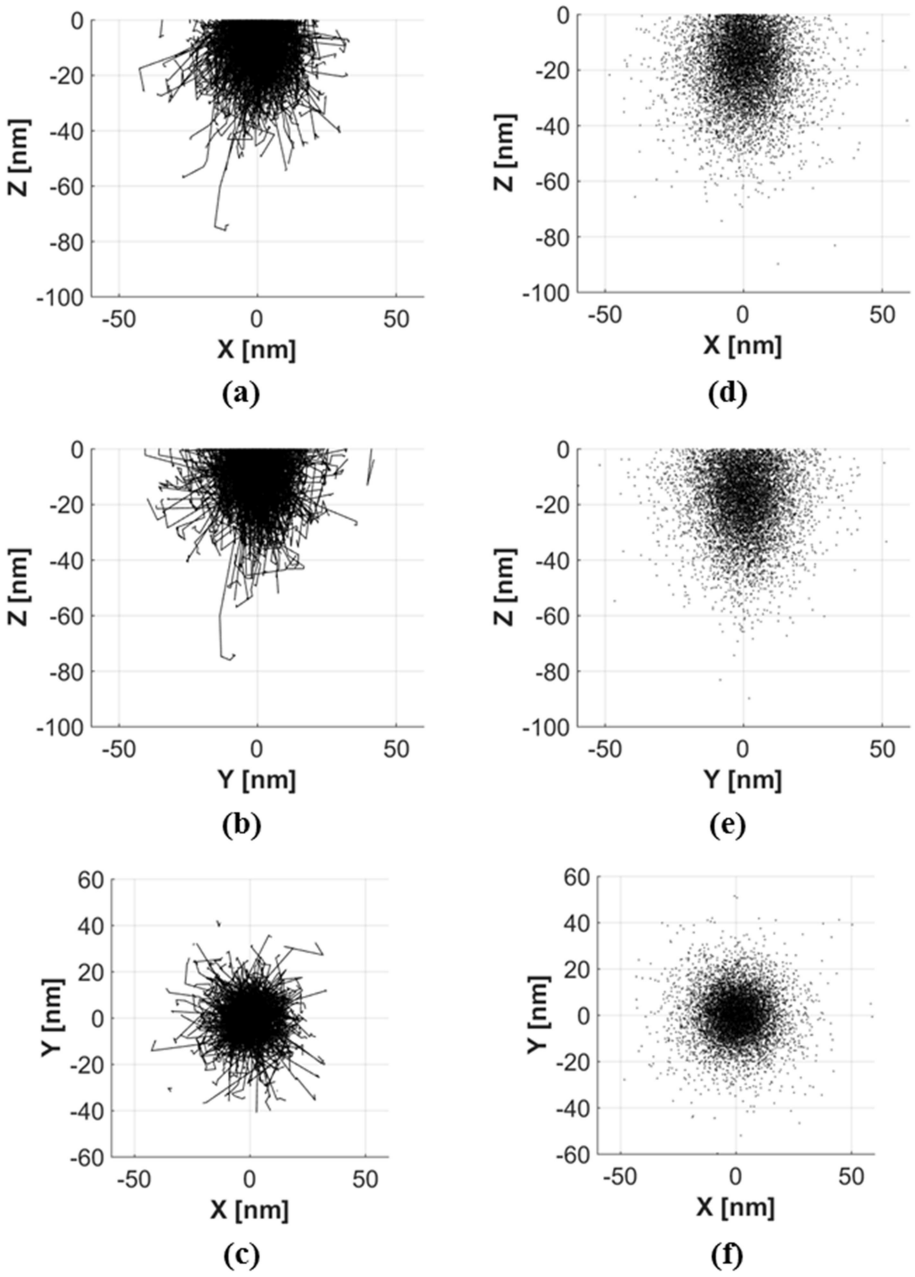

Figure 52 Simulation results of trajectories of 1000 ions in Si substrate

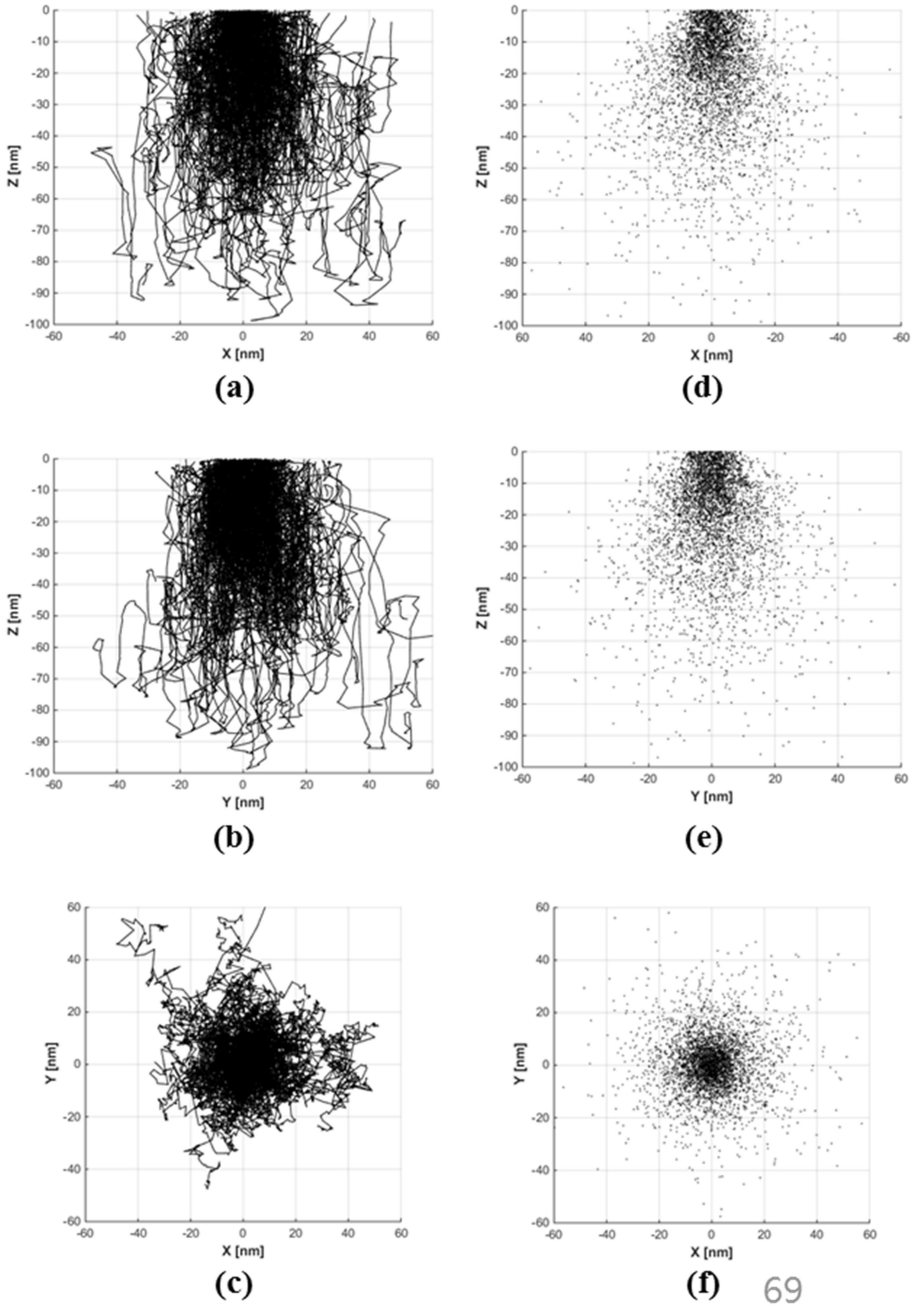

69

Figure 53 Simulation results of trajectories of 776 electrons in Si substrate

4.3.8.2 Timely dependent growth rate at a temperature

We developed a numerical model using the HD to simulate the dynamic deposition profile when increasing numbers of 30 keV, 20 pA gallium ions were used in FIB-CVD. Phenanthrene ($C_{14}H_{10}$) was employed for amorphous carbon deposition on an Si substrate. Although molecular dissociation data, such as the energy-dependent dissociation cross-section and the threshold energy required for simulation of deposition, are required, the phenanthrene data are not yet available. Thus, Smith et al. assumed that the cross-section was 10-fold larger than the electron-based dissociation cross-section when modeling deposition triggered by a helium ion beam [34]. Mitsuishi et al. used an energy-dependent equation based on the first Born approximation to calculate the cross-section [92]. Alman et al. developed a hydrocarbon model based on empirical data [89]. The energy-dependent equation for the dissociation cross-section that we used was based on the Alman empirical model and the first Born approximation. The constants were calculated using a maximum dissociation cross-section (σ_{max}) of 0.293 nm2, dissociation threshold energy (E_{th}) of 10 eV, and a maximum energy at σ_{max} of 188.04 eV.

$$\sigma(\mathrm{E}) = \frac{43.23}{\mathrm{E}} \ln\left(\frac{\mathrm{E}}{10}\right) \tag{74}$$

Figure 54 shows the instantaneous simulated deposition profile and corresponding cross-section at the time when 3.7×10^{8} ions were introduced. We subjected 1 million ion particles to MC simulation, and chose a value of 4000 as the representative particle ratio.

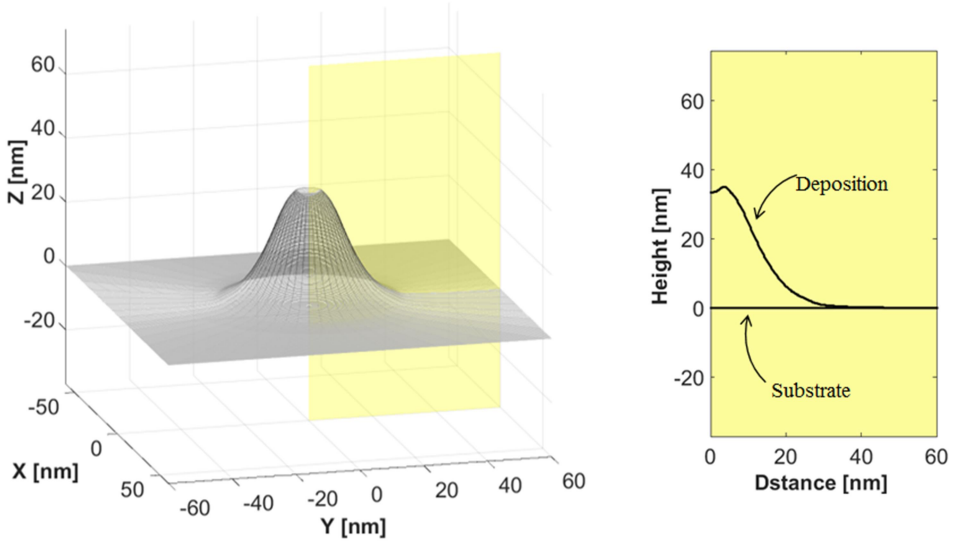

Figure 54 Deposition profile and the corresponding cross-section when 3.7 $\times 10^9$ ions were introduced.

Figure 55 shows the HDT map, the surface edge of the cross-section, and the distance values in the region adjacent to the edge, at a specific time. As described above, identification of the surface edge is critical when seeking to describe electron emission and precursor molecule adsorption during FIB-CVD simulation. In a DT map, the distance value of a pixel corresponding to a surface edge has a value of zero. Each pixel has a distance corresponding to the shortest distance to the nearest surface edge. The maximum distance was 255. Thus, all pixels of the DT map have distance values between 0 and 255. When the DT map is visualized, a distance value 0 is represented by black, and a value of 255 by white, in an 8-bit gray image. As shown in Fig. 55, the surface edges of the deposit and substrate were correctly represented in black, and the pixels became gradually brighter with greater distance from the edge. The DT map was updated after depositional events

caused by emitted electrons generated by a single ion. The region changed by such depositional events is very small compared to the size of the entire simulated region. Therefore, when updating the DT map, it is sufficient to recalculate only in the region in which deposition increased.

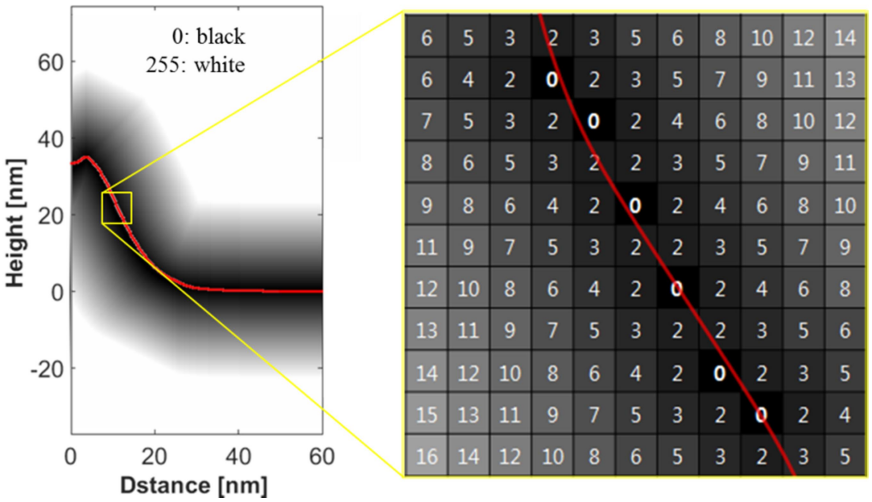

Figure 55 The distance transform (DT) map visualized by creating an 8-bit gray image, and the distance values in the region adjacent to the surface edge.

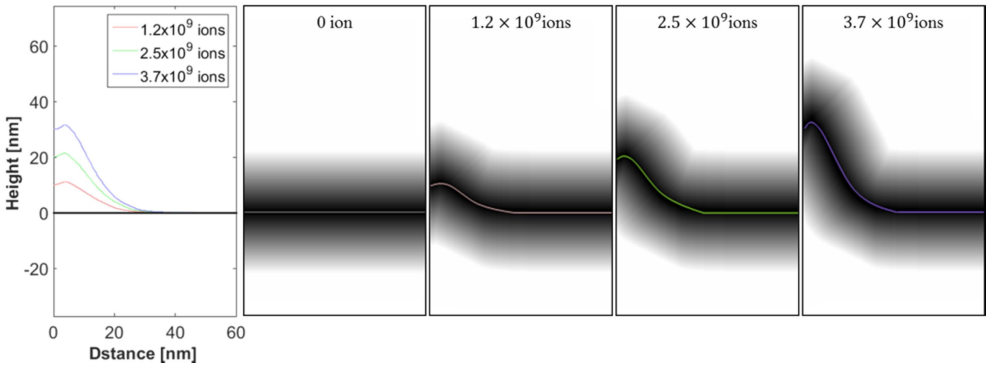

Figure 56 Evolution of the deposition and the corresponding DT map.

Figure 56 shows the evolving surface edges of deposition and the

corresponding DT maps as the number of introduced ions increase. As a DT map processes surface edges (critical in terms of electron emission), the carbon deposit, substrate, and vacuum space area are not described in the map. As mentioned above, the simulated depositional evolution was implemented using a CA model. When a deposition event occurs in a certain “molecule” cell, the state of that cell transitions from molecule to solid, which subsequently increases the state transitions of adjacent cells. After processing all depositional events attributable to the electrons generated by a single introduced ion, the DT map is updated to reflect these results. That updated map is then used to process the ions emitted when the next ion arrives.

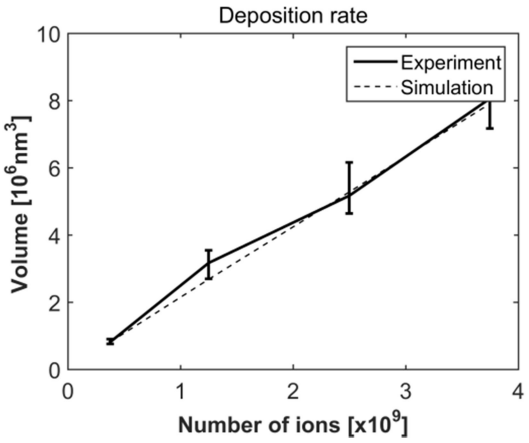

Figure 57 The simulated and experimental deposition rates

The simulated deposition rate was compared with experimental data. To observe the evolution of deposition, the number of introduced ions was set to 0.4×10^9, 1.2×10^9, 2.5×10^9, and 3.7×10^9, respectively. Deposition volumes were calculated using profile data obtained by atomic force microscopy. The simulated deposition and the measured rate are compared in Figure 57. The simulated data were scaled based on the experimental data obtained when 0.4×10^9 ions were

introduced. The error between the simulated deposition rates and the experiment data at other ion numbers were about 15%, 2%, and 2%, respectively. However, it should be noted that our simulation features certain indeterminate factors. First, we do not consider variations in ion and electron scattering attributable to differences between the Si substrate and the carbon deposit. Thus, ion and electron scattering in the interfacial surface between silicon and amorphous carbon are not reflected in the simulation. In addition, as the constants used to describe the distributions of precursor molecules on the surface vary with the process conditions, it is difficult to obtain accurate results. Such uncertainties were also evident in previous works and are under study by many researchers. In addition, our numerical modeling is only 2D in nature; we sought to simulate an axially symmetrical deposition. Therefore, in future, it will be necessary to use a 3D DT map to extend the model to 3D space.

4.3.8.3 Temperature dependent growth rate

In this simulation study, the effect of the precursor gas temperature on the deposition rate in the FIB-CVD process was analyzed for the first time. As mentioned earlier, in this work, we described the FIB-CVD process mechanism as a model based on the emitted SE generated by primary ion scattering. Therefore, since the deposit grows every time step, the topography of the surface must change in real time and the surface condition must be updated accordingly. The results of the FIB-CVD simulation according to the precursor temperature are shown in Fig. 58. It is assumed that the deposited structure has a rotatable structure with respect to the Z axis because the structure was deposited by a fixed spot ion beam. Therefore, the cross section of the structure shown in Fig. 58 was used for

comparison of the deposition shape according to the temperature change. As can be seen from the simulation results, when the temperature of the precursor rises, the vertical, lateral, and volumetric growth rates increase even under the same amount of precursor gas. This tendency shows good agreement with the experiment results.

However, even though the tendency to increase was similar, a significant difference was observed in the magnitude of the growth rate. These differences can be analyzed by several factors. When the ion beam is irradiated, sputtered milling by the FIB proceeds together with CVD. In addition, re-deposition phenomenon occurs in which materials removed by milling are re-deposited in the vicinity. However, these phenomena were not considered in the simulation. Therefore, the difference between the experiment results and simulation results are inevitable. Another reason may be that the simulation does not fully consider changes in phenomena such as adsorption, decomposition, and other physical behaviors that change with the change of the precursor gas temperature. However, unlike the effect of substrate temperature on deposition rate, all the deposition rate, i.e. vertical, lateral, and volumetric deposition growth rate was increased as the temperature of the precursor gas rises. The results of the comparison of experimental data and simulation results for vertical, lateral and volumetric growth rates as precursor gas temperature rises are shown in Fig. 59. The simulation 1 in the chart is the result of a simulation in which the reaction rate of the precursor causing the decomposition is regarded as constant value, and the simulation 2 is the result of simulation in which the reaction rate is changed according to the temperature by applying the Arrhenius equation. As can be seen from the chart, it can be observed that the simulation 2, which takes the reaction rate into

consideration, is closer to the experimental value.

In this study, the effect of precursor gas temperature on the deposition rate in the FIB-CVD process was simulated by developing the theoretical model. As a result, similar tendency as the previous experimental results can be confirmed, but significant difference between two results is still remained. This suggests that further study will be necessary to reduce the gap between the two results through complementation of the process mechanism model.

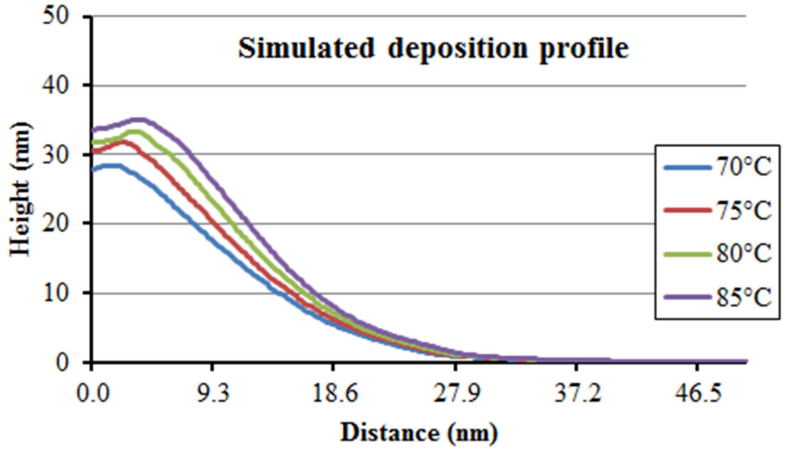

Figure 58 Cross sections of the depositions according to the precursor gas temperature

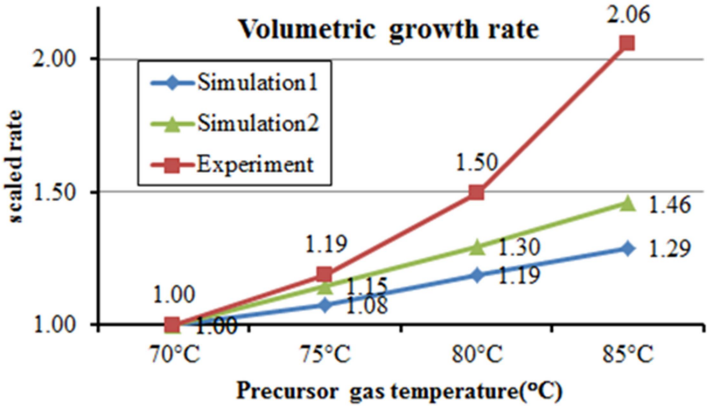

(a)

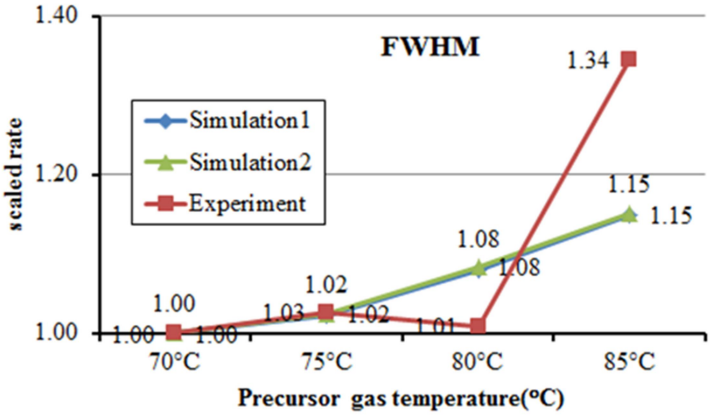

(b)

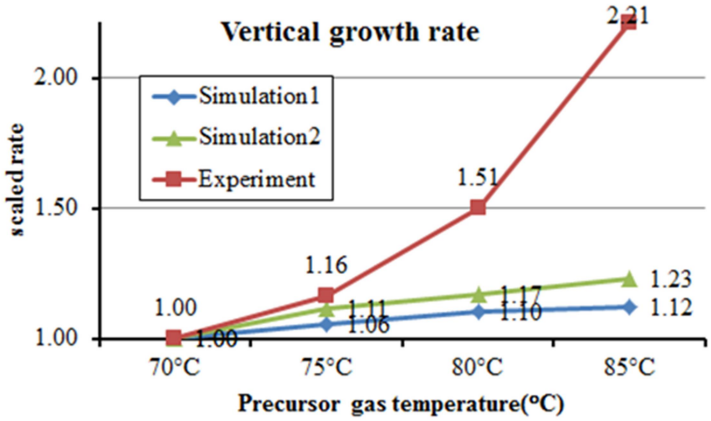

(c)

Figure 59 Comparison of deposition rates between simulation results and experimental data

Chapter 5. Fabrication of micro-actuator

5.1 Introduction

Research on micro-actuator has been widely carried out for various purposes such as biomedical devices, microsensors, and microfluidics. Many types of smart materials including piezoelectric material, shape memory alloy, magnetic materials are used for the materials. Among them, shape memory alloy (SMA) has been regareded as one of the most promising candidate because it can generate significant force and displacement (work density) compared to other actuation sources [93]. Even more, SMA has unique property such as shape memory effect (SME), superelasticity (pseudoelasticity) and high power to weight ratio and good biocompatibility [93-96]. In terms of making micro-/nanoscale actuation, SMA is versatile actuation source because shape memory effect is maintained even in tens of nanometer scale [97]. Including shape memory effect, various types of physics such as electrostatic, electromagnetic or piezoelectric were adopted for microscale actuation. Among them, shape memory alloy possesses uniquely high work density than other methods, so it can give much actuation force than other sources.

Recently, several researchers have been studying microscale actuators that combine the intrinsic properties of SMA and the mechanical properties of other materials. Zakharov et al. developed a cantilever-type micro-actuator using Pt elasticity by layering a thin Pt layer on pseudoplastic strained SMA [60]. In their

study, FIB-CVD was used to deposit the Pt layer. However, the performance characteristics of microscale actuators including SMA are as important as the properties of the material, and also the structure characteristics attributable to the design. Therefore, if FIB-CVD can be adapted in the design of an actuator, more variety of microscale actuators can be manufactured. FIB-CVD processes have been commonly used for deposition where high accuracy of micro/nano scale is required. However, since the scale of features produced by FIB-CVD is generally limited to a scale of several tens to several hundreds of nanometers, there have been limitations in applying the fabrication of a microscale actuator.

In this chapter, the feasibility of FIB-CVD processes on gap-fill processes that extend the traditional use area of FIB-CVD to micro-scale using diffusion-enhanced FIB-CVD processes has been investigated. As a case study, the development of a micro-scale SMA-based composite actuator was attempted.

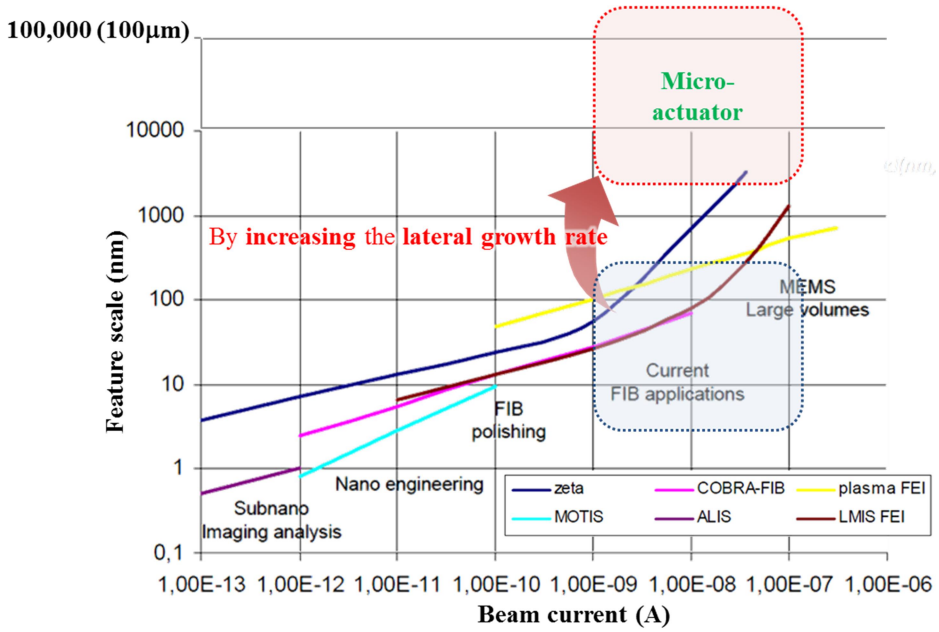

Figure 60 Current and future of FIB technology and the regime of localized FIB-CVD process (Orsay Physics, 2014)

5.2 Fabrication process of a micro-actuator

Nitinol with 50% weight percent of titanium and nickel in each (Flexinol, DYNALLOY, Inc.) was used as a material for the actuator. Figure 61 illustrates a solid-state phase transformation called nitinol-containing martensitic transformation of SMA. SMA has a simple cubic structure called austenite (parent phase) at high temperature. When it comes down to low temperature, it has a crystal structure (daughter phase) called martensite which becomes a little more complicated in crystalline structure. Even if deformation occurs at low temperature, it is restored to original shape by phase change when temperature rises. This phenomenon is called the one way memory effect of SMA. When the deformation called training is repeated, it is recognized that the shape is remembered even at

low temperature due to the internal residual stress. This is called a two-way memory effect. Generally, the maximum elasticity strain of nitinol is known to be about 8%, including the superelasticity regime. However, it is known that the two way memory effect can only use strain of less than 8% [98, 99].

Using SMA's two way memory effect, it is possible to fabricate an actuator that can be driven repeatedly with only thermal energy without the help of external force. However, the use of the two way memory effect has the disadvantage of reducing the deflection range. The method to solve this problem has been studied in two main directions. One is the method of inducing the actuating using the difference of the mechanical property of the two materials by synthesizing the composite material by combining other materials in the SMA. And the other method is a way to extend the deformation range through the geometry design of the actuator.

We fabricated a microscale SMA-based composite actuator with different driving characteristics by modifying the deflection behavior using localized carbon deposition by diffusion enhanced FIB-CVD. The base actuator is a high speed microscale SMA linear actuator. The fabrication process of the actuator is shown in Fig. 62. The base actuator consists of 6 unit cells of diamond pattern to obtain large linear deformation greater than 8%, which is the maximum elastic strain of SMA. In this structure, the deformation in the longitudinal direction is concentrated in the corner area where stress is concentrated. If this part is fixed by carbon deposit, strain is expected to be tilted to one side and modified deformation from linear motion to bending motion. Figure 62 (a) shows the corner area of the diamond pattern, which is the basic cell structure of the base actuator. However, in general FIB-CVD applications, there has not been reported about the attempt to the

deposition on the bottomless space. This process is referred to as a Gap-fill process and is used as a special process for CVD. In this study, we tried to deposit carbon in bottomless space using FIB-CVD process. For this process, it is advantageous that the lateral deposition rate is high; therefore the operating parameter is set with reference to the influence of the deposition rate according to the precursor temperature which was verified in the previous chapter.

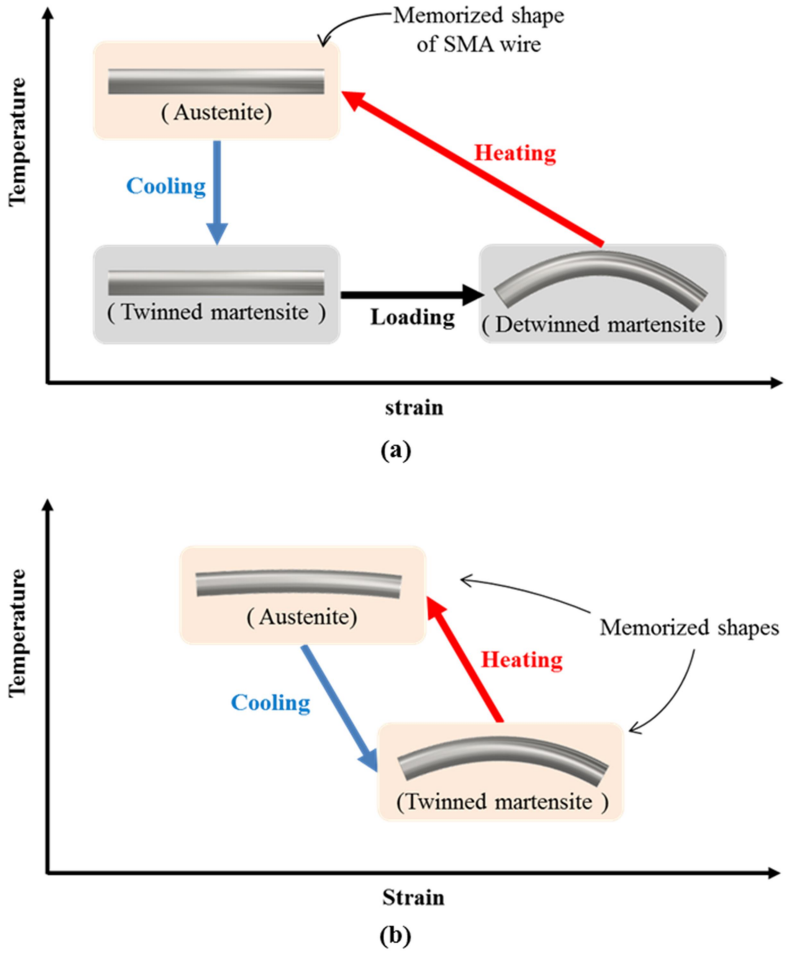

Figure 61 Properties of shape memory alloy (SMA); (a) one-way memory effect (b) two-way memory effect

Figure 63 shows fabrication process of the micro composite bending actuator on the basis of a microscale linear motion actuator used as a base actuator. The dimensions of the base actuator are 31μm in length, 25μm in width, and 1μm in thickness. Before the localized FIB-CVD deposition, the base actuator should be in deformed state. In this state, a deposit block is stacked on one side of the cell and fixed. Using this approach, the actuator is deformed asymmetrically and the bending motion is performed. Figure 64 is an SEM image of a linear actuator wrapped on one side of the actuator with a carbon block using a FIB-CVD process. The fabricated bending actuator is shown in Fig. 63 (c). Fig. 64 is an image in which the carbon deposit evolves in the bottomless space. At the beginning of the deposition, carbon deposit is stacked on the side of the SMA wire and as the process progresses, the deposits in both sides slowly grow and finally they are connected to each other.

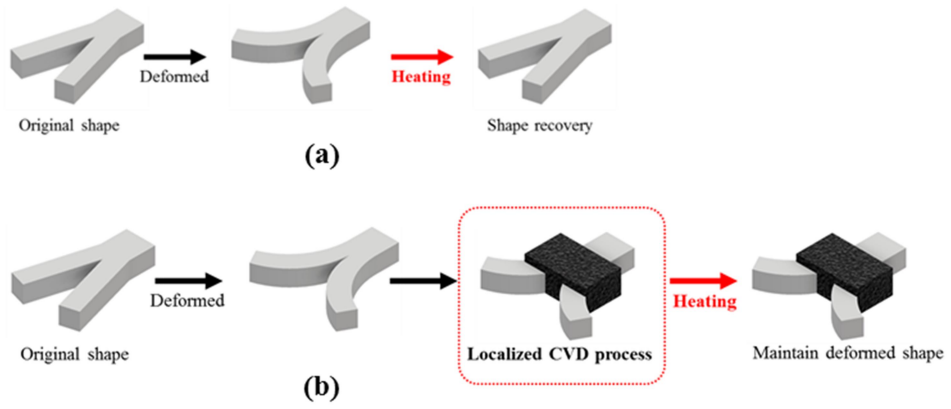

Figure 62 Deposited block that interfere with shape recovery of a SMA (a) Shape recovery of general SMA actuator (b) the deposited block forces the SMA actuator to stay its deformed shape.

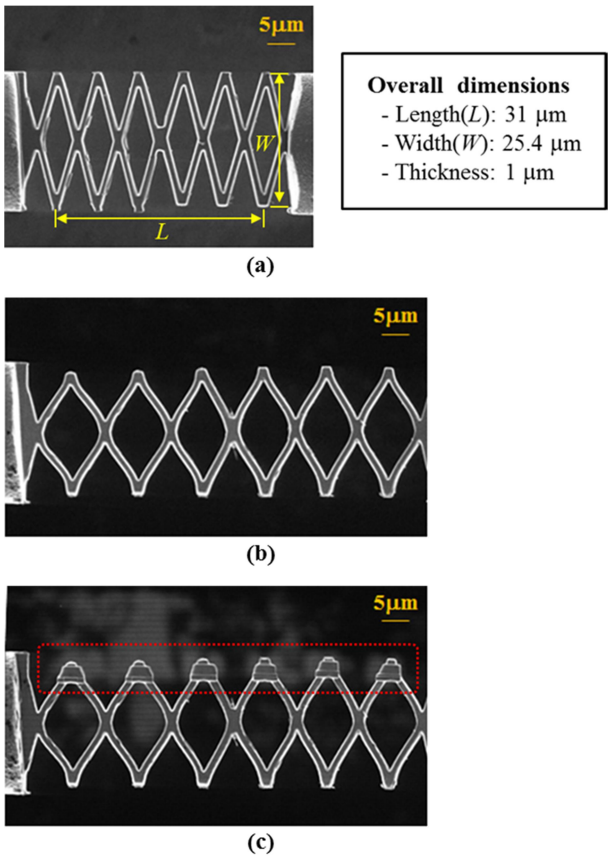

Figure 63 SEM images of (a) memorized shape, (b) stretched shape, and (c) carbon deposited on one side of SMA linear microactuator

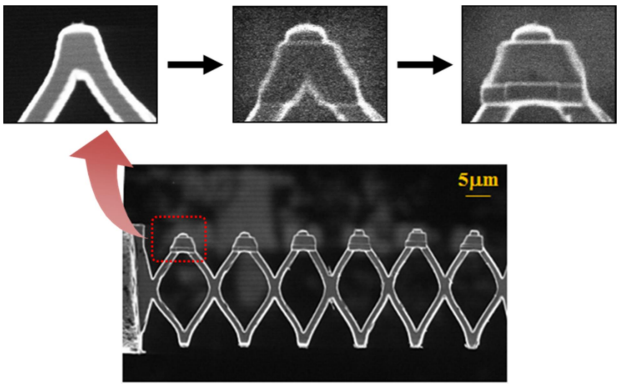

Figure 64 Evolution of depositions via localized FIB-CVD

5.3 Deflection behavior of SMA carbon composite actuator

For the evaluation of the performance, the actuator was operated using an ion beam inside the FIB chamber. The figure is a SEM image showing the linear deformation of the original linear actuator. Figure 66 shows the operation of the bending actuator in which the deformation behavior was modified by the carbon blocks deposited on one edge of the original actuator by the localized FIB-CVD. It can be observed that the actuator which is filled with the carbon block one side deforms the original linear deformation and performs the bending motion. In addition, it can be seen that the deformed state of the deposited surface is maintained even though the opposite side moves according to the original deflection pattern. This is because the elastic modulus of carbon has a larger value than that of SMA and restrains deformation with a force greater than resilience induced by external heat. The modification of deflection by carbon deposit block requires some confirmation. First, it is necessary to confirm the adhesion between carbon deposit and SMA. In order to use the mechanical strength of the amorphous carbon deposit, a sufficient bonding force between the two materials should be assumed. In addition, another thing to consider is checking whether the carbon block is well filled in the empty space. No FIB-CVD process results have yet been reported for empty spaces. Finally, it is necessary to investigate the mechanical strength of the carbon deposit. The exact mechanical properties of the two materials are necessary to define the process parameters of FIB-CVD for the fabrication of SMA-based composite actuators. Figure 67 is the SEM images of the side of the actuator cells filled with carbon deposit. In the figure, the upper surface of the surface is connected to the

carbon deposit, but the lower part is not completely filled. However, when comparing the images before and after deformation, it can be confirmed that they are almost the same shape, and therefore, it can be confirmed that there is a force capable of restraining the resilience of SMA even with the present deposit. For more accurate analysis, experiment on measuring the mechanical strength was performed to analyze the mechanical strength of nitinol and carbon deposited nitinol in the microscale.

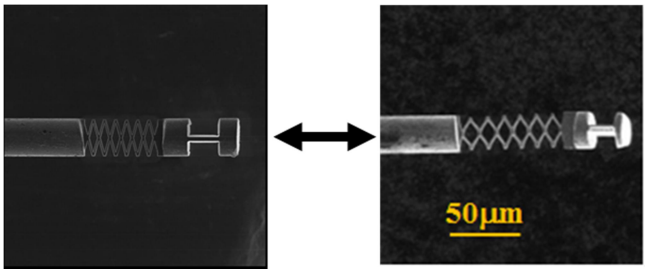

Figure 65 Actuating behavior of original linear actuator

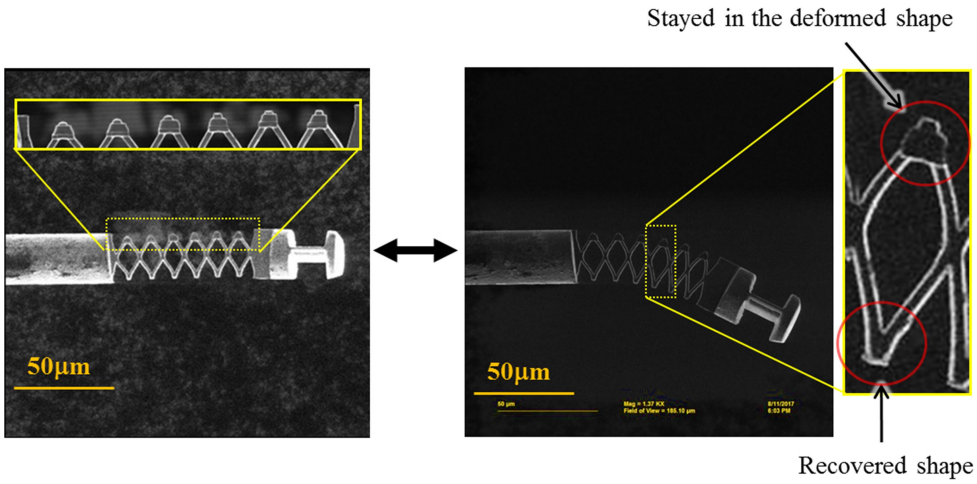

Figure 66 Change of the actuating of SMA microactuator from linear deformation to bending deformation

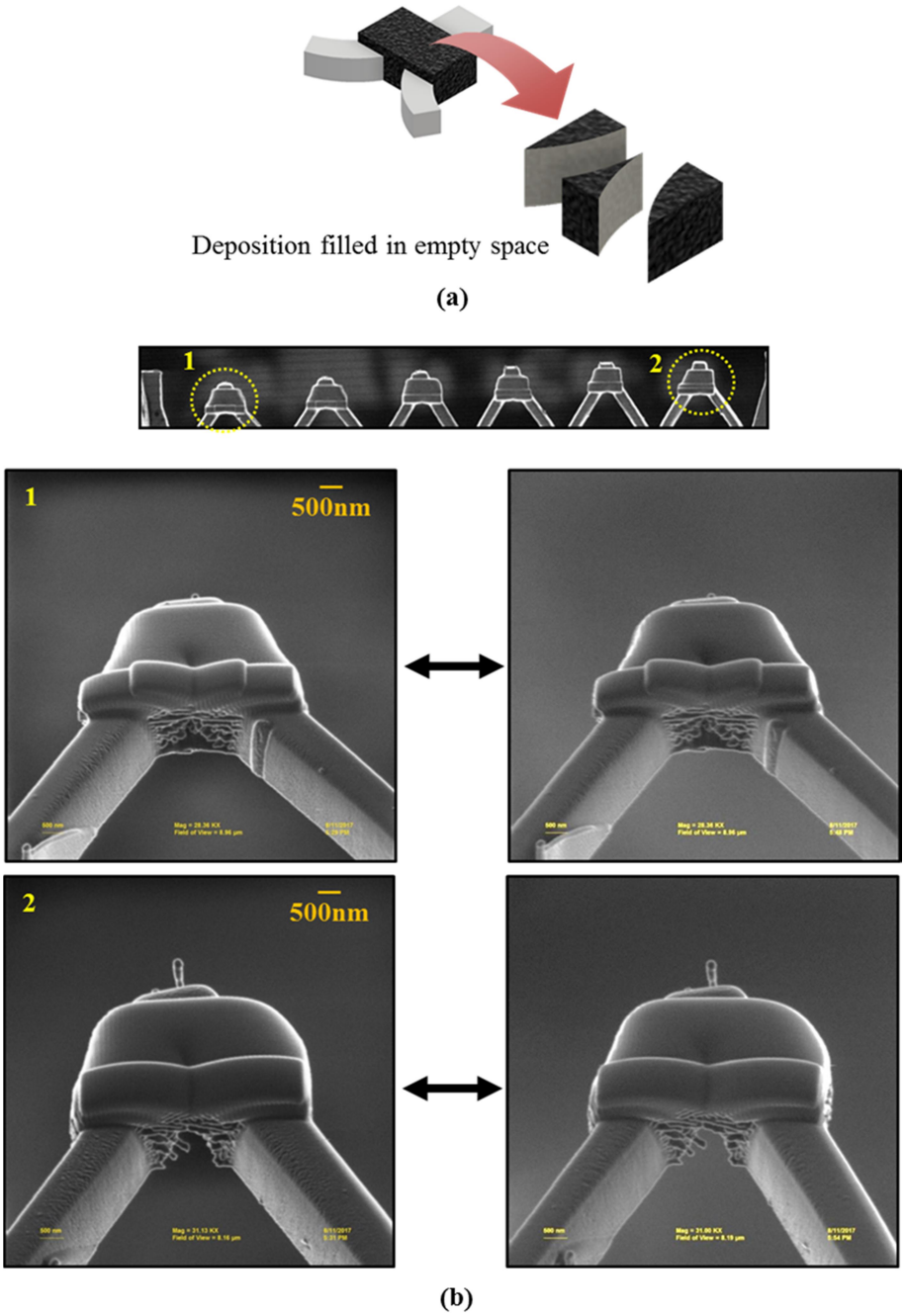

Figure 67 State of the deposited blocks before and after actuating

5.4 Mechanical analysis of the stiffness of the deposited carbon block

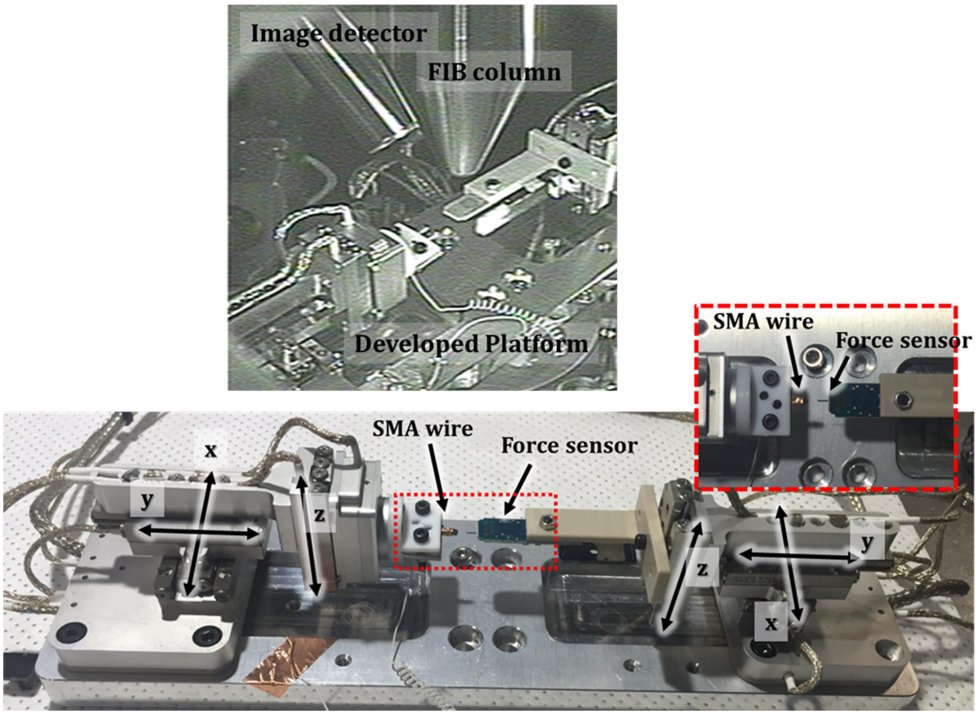

Figure 68 Expermental setup for microscale tensile test

In order to confirm whether the carbon block stacked via the localized FIB-CVD process effectively restrains the resilience of the SMA, an experiment was conducted to measure the mechanical stiffness. Figure 68 shows an experiment setup to perform a tensile test for the microscale specimen. The laboratory made nanostage consists of seven axes with a resolution of 1 nm. Also, a force sensor is connected to one side, so force and velocity can be measured in real time while pulling the specimen. Nano-states were mounted inside the FIB-CVD chamber and

tensile tests for the microscale specimen were performed. Specimens were made using SMA and SMA-carbon composite materials for comparison of stiffness.

The process of preparing the specimen of the SMA material is illustrated in Fig. 69. A nitinol wire with a diameter of 25.4 μm was fabricated by FIB milling process for the SMA specimen. The preparation of the SMA-carbon composite specimen was carried out in the process sequence shown in Fig. 71. A slit was formed on the inside of the SMA specimen via FIB milling and carbon deposit was filled in the slit through a localized FIB-CVD process. Figure 70 is a SEM image of a micro specimen fabricated for tensile testing to analyze the mechanical properties of a microscale SMA based composite actuator. Dimensions of each specimen are shown in Fig. 70 (a) and 73 (a). In order to compare the strength of micro composite, reference specimens were prepared first. Tensile test was performed by using a micro force sensor in the FIB-chamber to measure force and displacement, and strain was calculated using a real-time SEM image and displacement data. The loading rate of the force is 50 nm / sec.

The results of the tensile test on the reference specimen are shown in Fig. 73, and 74, respectively. Figure 73 shows the characteristics of the strain-stress curve of a typical SMA. Unlike ordinary metals, SMA is a material that is deformed by solid phase change and has a curve that is different from the normal stress-strain curve. That is, the elastic section is divided into a linear elastic section and a superelastic section. The inset of Fig. 73 shows that the elastic region is divided into two regions. Xiaojun et al. conducted a tensile test on nitinol wire of 700 μm diameter. In their study, the stress (σ_{ms}) at the start of the martensite phase was measured at 107 MPa and the stress at the end (σ_{mf}) at 118 MPa [100]. This is

because the strain in the superelastic section is due to the phase change and the stress is the same as that known to be fixed. However, in this experiment, the value of σ_{ms} was measured to be 103 MPa, which was similar to that of the literature, but the value of σ_{mf} was 273 MPa, which was measured to have a gentle slope unlike the literature. It can be inferred that the micro specimen slipped due to the load, or that it contained uncertainty of calculation due to the difficulty of accurate section measurement. Also, the points at which the stress rapidly changed in the SS curve were observed. The SEM images of the stretched specimen at the corresponding time were attached in Fig. 73. In the figure, we could observe that some part of the specimen is stretched rapidly. This can be interpreted as a characteristic of the SMA material that the strain may increase sharply without increasing stress due to a phase change in the region where stress is concentrated. As a result of the tensile test data, the elastic modulus of the SMA specimen was calculated to be about 9.97 GPa.

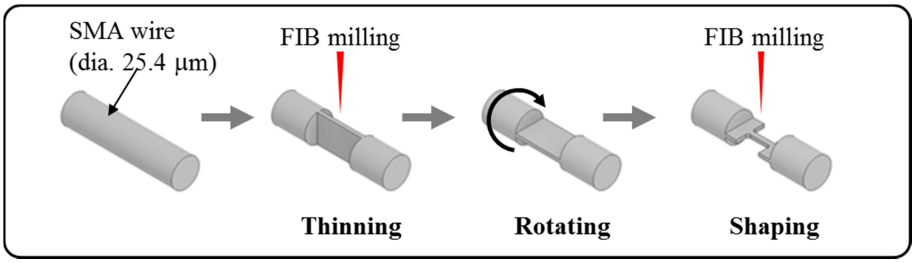

Figure 69 Fabrication process for a micro-specimen of SMA material from SMA wire

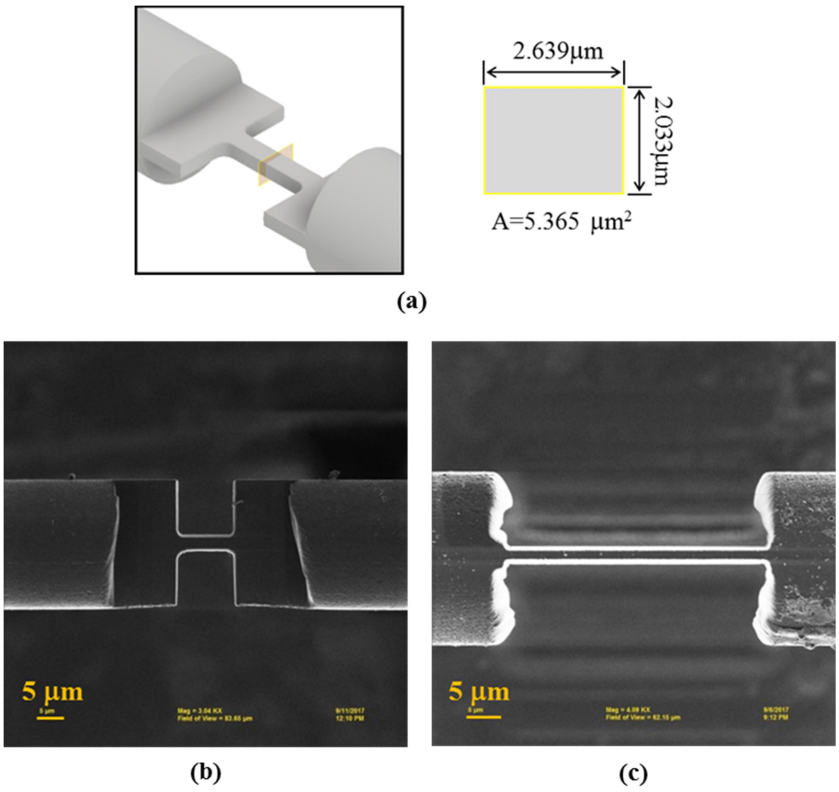

Figure 70 Fabricated micro-specimen of SMA material

Figure 74 shows tensile test results for SMA-carbon composite specimens. These results also show some interesting results, different from the traditional stress-strain curves. First, it can be seen that the elastic modulus is drastically increased compared to the ordinary nitinol material. This can be expected as a result of adding the property of a carbon deposit with a large elastic strength. However, several discontinuities were observed during the course of the strain. Figure 74 shows the time-based matching of the image of the specimen strain and the section where the discontinuity occurred. At the point where the first discontinuity appeared, the crack of the carbon deposit was observed for the first time. After analyzing the image of the specimen at the point where the discontinuity occurs,

we could confirm that a new crack occurs as well. It is analyzed that the strain hardly occurs because the stress is concentrated on the carbon deposit having strong stiffness, and the stress is dispersed to the SMA at the moment of cracking of the carbon deposit. In addition, cracking of the carbon deposit due to stress concentration proves indirectly that the adhesion between carbon deposit and SMA is strong enough to form a composite. If the adhesion between the two materials was weak, the stress would not be concentrated on the carbon deposit and the carbon deposit would have been separated from the SMA. The elastic modulus of the SMA-carbon composite measured by tensile test was about 19.93 GPa, which was about 100% higher than that of SMA only material. The rate of increase can be adjusted by the ratio of SMA to carbon deposit.

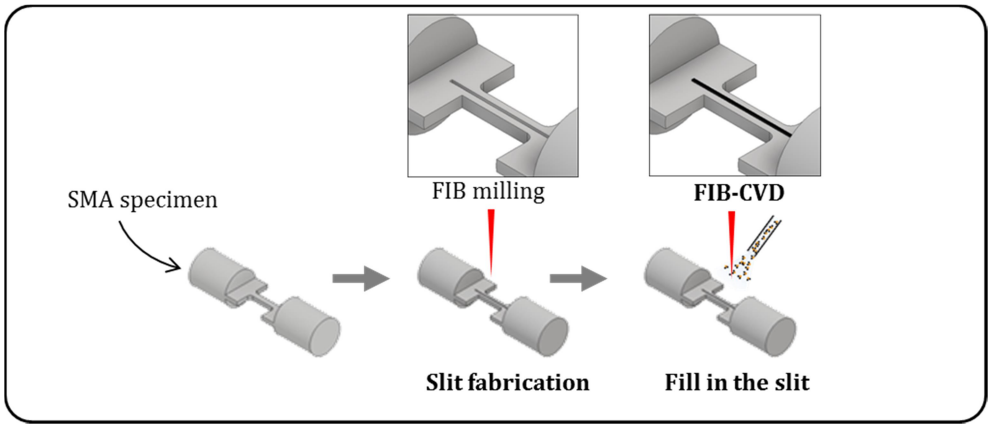

Figure 71 Fabrication process for a micro-specimen of SMA-carbon composite material from SMA specimen

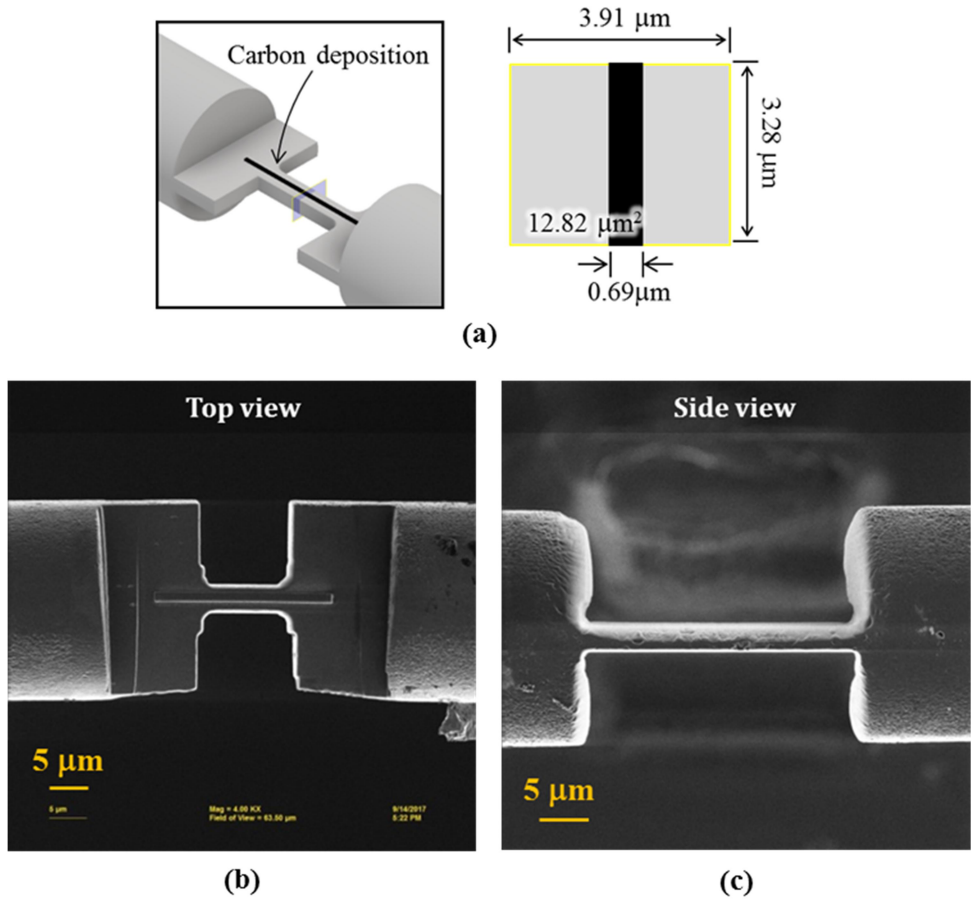

Figure 72 Fabricated micro-specimen of SMA carbon composite material

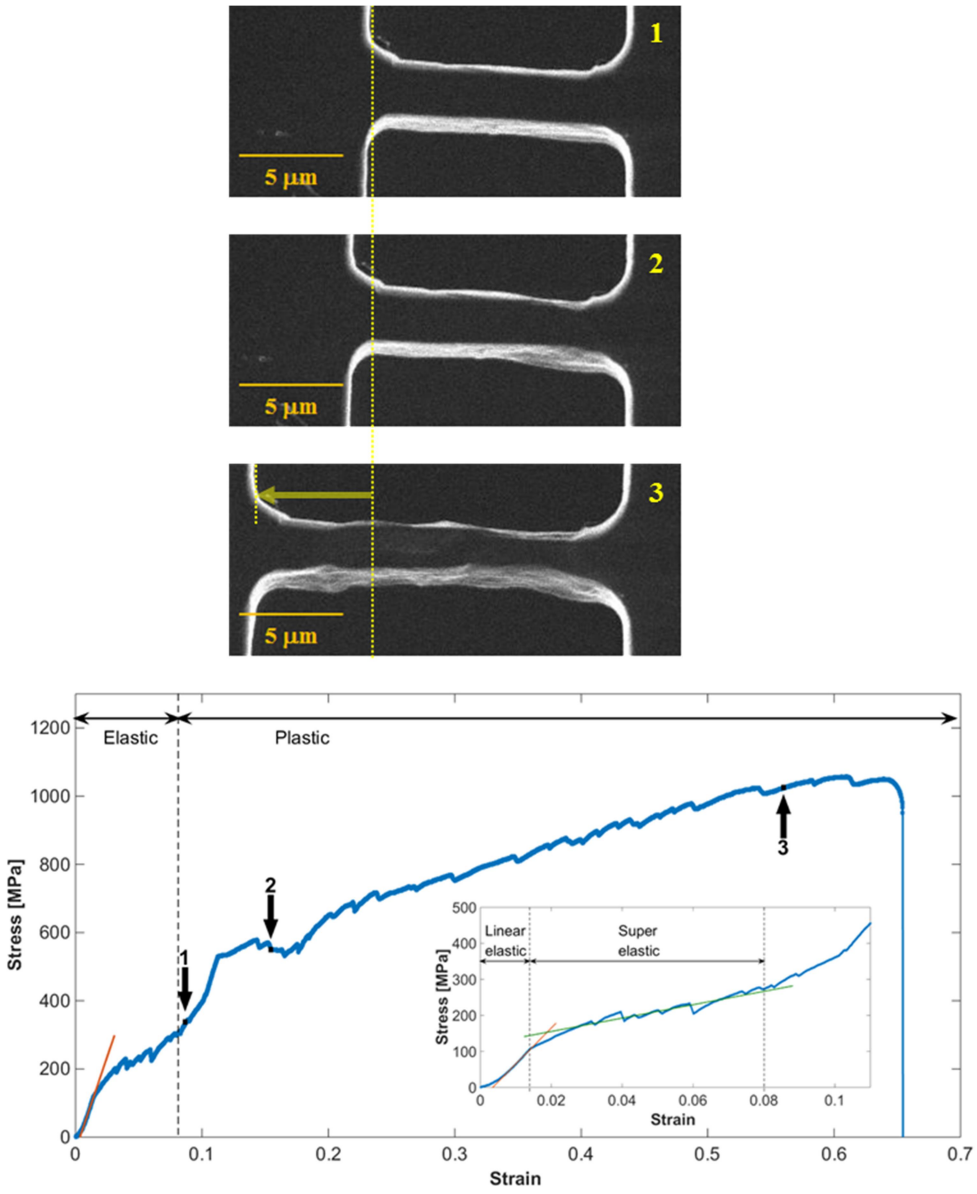

Figure 73 Tensile test results for the micro-specimen of SMA material

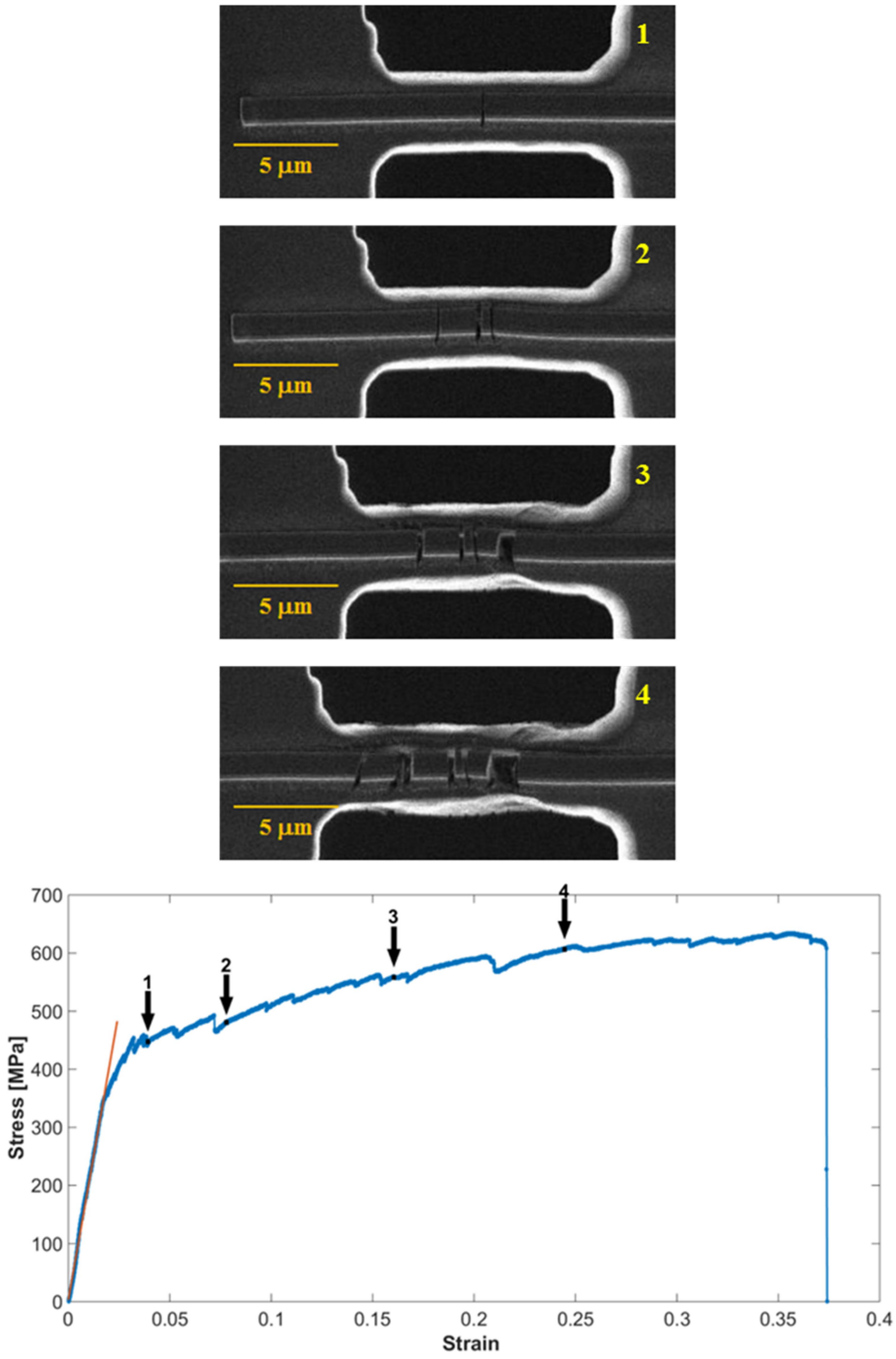

Figure 74 Tensile test results for micro-specimen of SMA carbon composite

The comparison of the stress-strain curves fore two specimens is shown in Fig. 75. As expected, the elastic modulus of the SMA-carbon composite increased in the elastic section. Therefore, this result can be a good evidence for the deformation of the deflection of the microscale SMA-based composite actuator fabricated.

In conclusion, it was confirmed that the elastic stiffness of SMA-carbon composite fabricated by localized carbon block via FIB-CVD process is strong enough to suppress shape recovery by SMA recovery force. In addition, in the tensile test of the SMA-carbon composite, it was indirectly confirmed that the adhesion of the carbon block and SMA is strong enough to form a composite through image analysis of the the discontinuities of the SS curve generated by the carbon block crack.

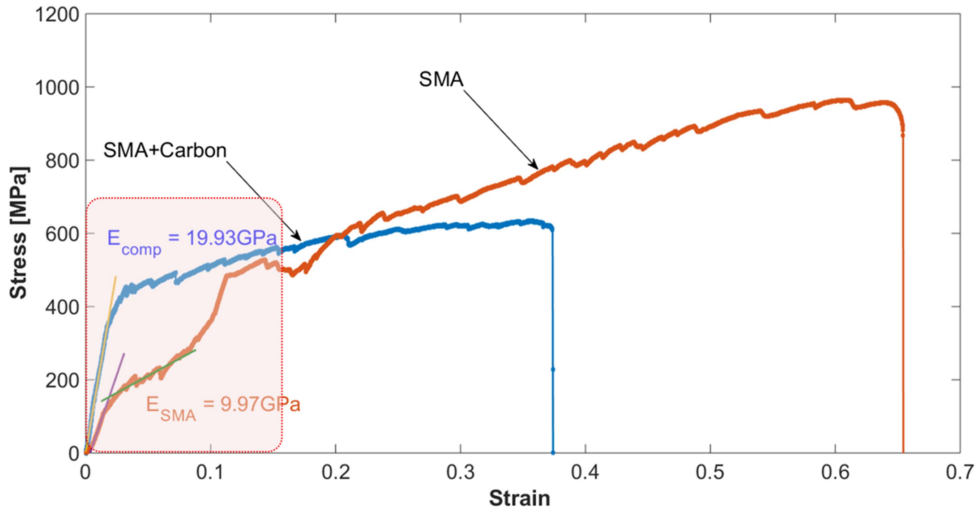

Figure 75 Comparison of stress-strain curves of SMA and SMA-carbon composite specimens

Chapter 6. Conclusions

In this study, the effect of the precursor gas temperature in the FIB-CVD process was investigated in terms of deposition growth rate. The gas injection system (GIS) which can independently control the precursor gas temperature without changing the supply amount of precursor gas was developed for the experiment. The developed GIS was applied to all FIB-CVD processes performed in this study. The effect was investigated by the experiment on phenanthrene deposition via FIB-CVD process. Experimental results are supported theoretically through simulation using proposed process model. Based on the fundamental process study, SMA-carbon composite microactuator was fabricated via localized FIB-CVD

In the simulation study, by applying cellular automata method and the Hausdorff distance transformation concept to the simulation of FIB-CVD process for the first time, a numerical method that can effectively process the distribution of precursor gas molecules and the emission of the secondary electron on an evolving surface in real time.

Through the experiment and the simulation, it was confirmed that the vertical, lateral, and volumetric growth rate were all increased while the temperature of the phenanthrene precursor gas rose from 70 °C to 85 °C

SMA-carbon composite microactuator was fabricated via localized FIB-CVD. In order to understand the actuating behavior, tensile tests on the microscale specimens made of SMA and SMA-carbon composite were performed. The test

results showed that the strengthened stiffness of a SMA-carbon composite is sufficiently stronger than the resilience of the SMA so that the shape recovery can be restrained. With this result, the deflection behavior of the SMA-carbon composited microactuator could be understood

Bibliography

1. Levi-Setti, R., *Proton scanning microscopy: feasibility and promise.* Scanning Electron Microscopy, 1974. **125**.
2. Utke, I., S. Moshkalev, and P. Russell, *Nanofabrication using focused ion and electron beams: principles and applications*. 2012: Oxford University Press.
3. Lipp, S., et al., *A comparison of focused ion beam and electron beam induced deposition processes.* Microelectronics Reliability, 1996. **36**(11-12): p. 1779-1782.
4. Ro, J., C. Thompson, and J. Melngailis, *Mechanism of ion beam induced deposition of gold.* Journal of Vacuum Science & Technology B: Microelectronics and Nanometer Structures Processing, Measurement, and Phenomena, 1994. **12**(1): p. 73-77.
5. Smith, D., J. Fowlkes, and P. Rack, *A nanoscale three-dimensional Monte Carlo simulation of electron-beam-induced deposition with gas dynamics.* Nanotechnology, 2007. **18**(26): p. 265308.
6. Volkert, C.A. and A.M. Minor, *Focused ion beam microscopy and micromachining.* MRS bulletin, 2007. **32**(05): p. 389-399.
7. Hoeflich, K., et al., *Direct Electron Beam Writing of Silver-based Nanostructures.* ACS Applied Materials & Interfaces, 2017.
8. Winkler, R., et al., *Toward ultraflat surface morphologies during focused electron beam induced nanosynthesis: disruption origins and compensation.* ACS applied materials & interfaces, 2015. **7**(5): p. 3289-3297.
9. Friedli, V., et al., *Dose and energy dependence of mechanical properties of focused electron-beam-induced pillar deposits from Cu (C5HF6O2) 2.* Nanotechnology, 2009. **20**(38): p. 385304.
10. Utke, I., et al., *Measurement and simulation of impinging precursor molecule distribution in focused particle beam deposition/etch systems.* Microelectronic engineering, 2006. **83**(4): p. 1499-1502.
11. Winkler, R., et al., *The nanoscale implications of a molecular gas beam during electron beam induced deposition.* ACS applied materials & interfaces, 2014. **6**(4): p. 2987-2995.

12. Kim, C.-S., S.-H. Ahn, and D.-Y. Jang, *Nanoscale effects in carbon structures fabricated using focused ion beam-chemical vapor deposition.* Thin Solid Films, 2010. **518**(18): p. 5177-5182.
13. Fu, Y., N.K.A. Bryan, and O.N. Shing, *Characterization of focused ion beam induced deposition process and parameters calibration.* Sensors and Actuators A: Physical, 2001. **88**(1): p. 58-66.
14. Bassim, N., K. Scott, and L.A. Giannuzzi, *Recent advances in focused ion beam technology and applications.* MRS Bulletin, 2014. **39**(04): p. 317-325.
15. Kim, C.-S., S.-H. Ahn, and D.-Y. Jang, *Review: developments in micro/nanoscale fabrication by focused ion beams.* Vacuum, 2012. **86**(8): p. 1014-1035.
16. Ali, M.Y., W. Hung, and F. Yongqi, *A review of focused ion beam sputtering.* International journal of precision engineering and manufacturing, 2010. **11**(1): p. 157-170.
17. Sim, J., J. Choi, and J. Kim, *Humidity sensing characteristics of focused ion beam-induced suspended single tungsten nanowire.* Sensors and Actuators B: Chemical, 2014. **194**: p. 38-44.
18. Chang, J., et al., *Bimorph nano actuators synthesized by focused ion beam chemical vapor deposition.* Microelectronic Engineering, 2009. **86**(11): p. 2364-2368.
19. Guo, D., et al., *Fabrication of micro/nanoelectrode using focused-ion-beam chemical vapor deposition, and its application to micro-ECDM.* Procedia CIRP, 2016. **42**: p. 733-736.
20. Toth, M., et al., *Continuum models of focused electron beam induced processing.* Beilstein journal of nanotechnology, 2015. **6**: p. 1518.
21. Fowlkes, J.D. and P.D. Rack, *Fundamental electron-precursor-solid interactions derived from time-dependent electron-beam-induced deposition simulations and experiments.* ACS nano, 2010. **4**(3): p. 1619-1629.
22. Lobo, C.J., et al., *High resolution radially symmetric nanostructures from simultaneous electron beam induced etching and deposition.* Nanotechnology, 2007. **19**(2): p. 025303.
23. Fowlkes, J.D., et al., *Simulation-Guided 3D nanomanufacturing via focused electron beam induced deposition.* ACS nano, 2016. **10**(6): p. 6163-6172.
24. Utke, I., P. Hoffmann, and J. Melngailis, *Gas-assisted focused electron beam and ion beam processing and fabrication.* Journal of Vacuum Science & Technology B, 2008. **26**(4): p. 1197-1276.
25. Schmied, R., et al., *Fundamental edge broadening effects during focused electron*

beam induced nanosynthesis. Beilstein journal of nanotechnology, 2015. **6**: p. 462.

26. Joy, D.C., *Monte Carlo modeling for electron microscopy and microanalysis*. Vol. 9. 1995: Oxford University Press.
27. Joy, D.C., *A model for calculating secondary and backscattered electron yields.* Journal of Microscopy, 1987. **147**(1): p. 51-64.
28. Biersack, J.P. and L. Haggmark, *A Monte Carlo computer program for the transport of energetic ions in amorphous targets.* Nuclear Instruments and Methods, 1980. **174**(1-2): p. 257-269.
29. Mueller, G.P., *Total cross-section corresponding to the differential cross-section of lindhard, nielsen and scharff.* Radiation Effects, 1974. **21**(4): p. 253-254.
30. J. F. Ziegler, M.D.Z., and J. P. Biersack, *SRIM software, the stopping and range of ions in matter.* 2008.
31. Ziegler, J.F., J. Biersack, and U. Littmark, *The stopping and range of ions in matter, Vol. 1.* 1, Pergamon Press, New York, 1985.
32. Stanford, M.G., et al., *Review Article: Advanced nanoscale patterning and material synthesis with gas field helium and neon ion beams.* Journal of Vacuum Science & Technology B, Nanotechnology and Microelectronics: Materials, Processing, Measurement, and Phenomena, 2017. **35**(3): p. 030802.
33. Timilsina, R. and P.D. Rack, *Monte Carlo simulations of nanoscale focused neon ion beam sputtering.* Nanotechnology, 2013. **24**(49): p. 495303.
34. Smith, D.A., D.C. Joy, and P.D. Rack, *Monte Carlo simulation of focused helium ion beam induced deposition.* Nanotechnology, 2010. **21**(17): p. 175302.
35. Ramachandra, R., B. Griffin, and D. Joy, *A model of secondary electron imaging in the helium ion scanning microscope.* Ultramicroscopy, 2009. **109**(6): p. 748-757.
36. Fu, Y., N.K.A. Bryan, and O.N. Shing, *Investigation of submicron linewidth direct deposition for high-density IC chip modification by focused ion beam.* The International Journal of Advanced Manufacturing Technology, 2001. **17**(11): p. 835-839.
37. Shawrav, M.M., et al., *Mask-free prototyping of metal-oxide-semiconductor devices utilizing focused electron beam induced deposition.* physica status solidi (a), 2014. **211**(2): p. 375-381.
38. Friedli, V. and I. Utke, *Optimized molecule supply from nozzle-based gas injection systems for focused electron-and ion-beam induced deposition and etching: simulation and experiment.* Journal of Physics D: Applied Physics, 2009. **42**(12): p. 125305.

39. Van Dorp, W. and C. Hagen, *A critical literature review of focused electron beam induced deposition.* Journal of Applied Physics, 2008. **104**(8): p. 081301.
40. Córdoba, R., et al., *High-purity cobalt nanostructures grown by focused-electron-beam-induced deposition at low current.* Microelectronic Engineering, 2010. **87**(5): p. 1550-1553.
41. Riazanova, A., *Direct Nanoprototyping of Functional Materials via Focused Electron Beam*. 2013, PhD thesis, School of Industrial Engineering and Management, KTH.
42. Garetto, A., *Electron Beam Induced Chemistry.* 2007.
43. Thiel, P.A. and T.E. Madey, *The interaction of water with solid surfaces: fundamental aspects.* Surface Science Reports, 1987. **7**(6-8): p. 211-385.
44. Ditizio, R.A., T. Nguyen, and T.D. Nguyen, *Nanolayer deposition using bias power treatment*. 2017, Google Patents.
45. Heard, P. and P. Prewett, *Focused ion beam deposition of carbon for photomask repair.* Microelectronic engineering, 1990. **11**(1-4): p. 421-425.
46. Dai, J., et al., *Direct fabrication of a WC SNS Josephson junction using focused-ion-beam chemical vapour deposition.* Journal of Micromechanics and Microengineering, 2014. **24**(5): p. 055015.
47. Ishida, M., J.-i. Fujita, and Y. Ochiai, *Density estimation for amorphous carbon nanopillars grown by focused ion beam assisted chemical vapor deposition.* Journal of Vacuum Science & Technology B, 2002. **20**(6): p. 2784-2787.
48. Fujita, J.-i., et al., *Structure and resonant characteristics of amorphous carbon pillars grown by focused-ion-beam-induced chemical vapor deposition.* Japanese journal of applied physics, 2002. **41**(6S): p. 4423.
49. Arnold, G., et al., *Fundamental resolution limits during electron-induced direct-write synthesis.* ACS applied materials & interfaces, 2014. **6**(10): p. 7380-7387.
50. Prestigiacomo, M., et al., *Studies of structures elaborated by focused ion beam induced deposition.* Microelectronic Engineering, 2004. **76**(1): p. 175-181.
51. Smith, D.A., J.D. Fowlkes, and P.D. Rack, *Understanding the Kinetics and Nanoscale Morphology of Electron-Beam-Induced Deposition via a Three-Dimensional Monte Carlo Simulation: The Effects of the Precursor Molecule and the Deposited Material.* Small, 2008. **4**(9): p. 1382-1389.
52. Plank, H., et al., *Fundamental proximity effects in focused electron beam induced deposition.* ACS nano, 2011. **6**(1): p. 286-294.
53. Tseng, A.A., *Recent developments in nanofabrication using focused ion beams.*

Small, 2005. **1**(10): p. 924-939.

54. Dubner, A., et al., *The role of the ion-solid interaction in ion-beam-induced deposition of gold.* Journal of applied physics, 1991. **70**(2): p. 665-673.
55. Melngailis, J., *Focused ion beam technology and applications.* Journal of Vacuum Science & Technology B, 1987. **5**(2): p. 469-495.
56. Reyntjens, S. and R. Puers, *A review of focused ion beam applications in microsystem technology.* Journal of Micromechanics and Microengineering, 2001. **11**(4): p. 287.
57. MoberlyChan, W.J., et al., *Fundamentals of focused ion beam nanostructural processing: Below, at, and above the surface.* MRS bulletin, 2007. **32**(05): p. 424-432.
58. Nguyen-Tran, H.-D., et al., *A review of electrically-assisted manufacturing.* International Journal of Precision Engineering and Manufacturing-Green Technology, 2015. **2**(4): p. 365-376.
59. Park, S.-I., et al., *A review on fabrication processes for electrochromic devices.* International Journal of Precision Engineering and Manufacturing-Green Technology, 2016. **3**(4): p. 397-421.
60. Zakharov, D., et al., *Submicron-sized actuators based on enhanced shape memory composite material fabricated by FIB-CVD.* Smart Materials and Structures, 2012. **21**(5): p. 052001.
61. Nakamatsu, K.-i., et al., *Nanostructure Analysis of Nanosprings Fabricated by Focused-Ion-Beam Chemical Vapor Deposition.* Japanese Journal of Applied Physics, 2009. **48**(10R): p. 105001.
62. Matsui, S., *Focused-ion-beam deposition for 3-D nanostructure fabrication.* Nuclear Instruments and Methods in Physics Research Section B: Beam Interactions with Materials and Atoms, 2007. **257**(1): p. 758-764.
63. Igaki, J.-y., et al., *Mechanical characteristics and applications of diamondlike-carbon cantilevers fabricated by focused-ion-beam chemical vapor deposition.* Journal of Vacuum Science & Technology B: Microelectronics and Nanometer Structures Processing, Measurement, and Phenomena, 2006. **24**(6): p. 2911-2914.
64. Puers, R. and S. Reyntjens, *Fabrication and testing of custom vacuum encapsulations deposited by focused ion beam direct-write CVD.* Sensors and Actuators A: Physical, 2001. **92**(1): p. 249-256.
65. Zhang, Y., et al., *A large-area 15 nm graphene nanoribbon array patterned by a focused ion beam.* Nanotechnology, 2014. **25**(13): p. 135301.

66. Schmidt, M.E., et al., *Focused ion beam milling of exfoliated graphene for prototyping of electronic devices.* Microelectronic Engineering, 2012. **98**: p. 313-316.
67. Shao, Q., et al., *High-temperature quenching of electrical resistance in graphene interconnects.* Applied Physics Letters, 2008. **92**(20): p. 202108.
68. Watanabe, K., et al., *Brilliant blue observation from a Morpho-butterfly-scale quasi-structure.* Japanese journal of applied physics, 2005. **44**(1L): p. L48.
69. Shukla, N., et al., *Study of temperature rise during focused Ga ion beam irradiation using nanothermo-probe.* Applied Surface Science, 2009. **256**(2): p. 475-479.
70. Kometani, R., et al., *In-situ Observation of the Three-Dimensional Nano-Structure Growth on Focused-Ion-Beam Chemical Vapor Deposition by Scanning Electron Microscope.* Applied physics express, 2008. **1**(5): p. 055001.
71. Friedli, V., et al., *Mass sensor for in situ monitoring of focused ion and electron beam induced processes.* Applied physics letters, 2007. **90**(5): p. 053106.
72. Igaki, J.-y., et al., *Comparison of FIB-CVD and EB-CVD growth characteristics.* Microelectronic engineering, 2006. **83**(4): p. 1225-1228.
73. Szkudlarek, A., M. Gabureac, and I. Utke, *Determination of the surface diffusion coefficient and the residence time of adsorbates via local focused electron beam induced chemical vapour deposition.* Journal of nanoscience and nanotechnology, 2011. **11**(9): p. 8074-8078.
74. Rucklidge, W., *Efficient visual recognition using the Hausdorff distance*. Vol. 1173. 1996: Springer Berlin.
75. Rubinstein, R.Y. and D.P. Kroese, *Simulation and the Monte Carlo method*. Vol. 10. 2016: John Wiley & Sons.
76. Rykaczewski, K., W.B. White, and A.G. Fedorov, *Analysis of electron beam induced deposition (EBID) of residual hydrocarbons in electron microscopy.* Journal of Applied Physics, 2007. **101**(5): p. 054307.
77. Mulders, J., *Practical precursor aspects for electron beam induced deposition.* Nanofabrication, 2014. **1**(1).
78. Gonzalez, C.M., *Elucidating Fundamental Mechanisms in Focused Electron-and Ion-Beam Induced Synthesis.* 2014.
79. Smith, D.A., J.D. Fowlkes, and P.D. Rack, *Simulating the effects of surface diffusion on electron beam induced deposition via a three-dimensional Monte Carlo simulation.* Nanotechnology, 2008. **19**(41): p. 415704.
80. Nastasi, M., J. Mayer, and J.K. Hirvonen, *Ion-solid interactions: fundamentals and applications*. 1996: Cambridge University Press.

81. Bendel, W.L., *Displacement and Ionization Fractions of Fast Neutron Kerma in TLDs and Si.* IEEE Transactions on Nuclear Science, 1977. **24**(6): p. 2516-2520.
82. Winterbon, K.B., P. Sigmund, and J. Sanders, *Spatial distribution of energy deposited by atomic particles in elastic collisions.* Kgl. Dan. Vidensk. Selsk., Mat.-Fys. Medd. 37: 14-(1970). 1970.
83. Ramachandra, R., *A Study of Helium Ion Induced Secondary Electron Production.* Doctoral Dissertations, 2009: p. 103.
84. Fu, J., *Process modeling and simulation of focused ion beam milling of water ice in a cryogenic environment*. 2008, The Pennsylvania State University.
85. Ziegler, J.F., M.D. Ziegler, and J.P. Biersack, *SRIM–The stopping and range of ions in matter (2010).* Nuclear Instruments and Methods in Physics Research Section B: Beam Interactions with Materials and Atoms, 2010. **268**(11): p. 1818-1823.
86. Lindhard, J., M. Scharff, and H.E. Schiøtt, *Range concepts and heavy ion ranges*. 1963: Munksgaard Copenhagen.
87. Lin, Y. and D.C. Joy, *A new examination of secondary electron yield data.* Surface and Interface Analysis, 2005. **37**(11): p. 895-900.
88. Joy, D. and S. Luo, *An empirical stopping power relationship for low-energy electrons.* Scanning, 1989. **11**(4): p. 176-180.
89. Alman, D., D. Ruzic, and J. Brooks, *A hydrocarbon reaction model for low temperature hydrogen plasmas and an application to the Joint European Torus.* Physics of plasmas, 2000. **7**(5): p. 1421-1432.
90. Kim, C.-S. and S.-H. Ahn, *Mechanical behavior of microscale carbon pillar fabricated by focused ion beam induced deposition.* International journal of precision engineering and manufacturing, 2014. **15**(7): p. 1485-1488.
91. Hausdorff, F., *Bemerkung über den Inhalt von Punktmengen.* Mathematische Annalen, 1914. **75**(3): p. 428-433.
92. Mitsuishi, K., et al., *Dynamic profile calculation of deposition resolution by high-energy electrons in electron-beam-induced deposition.* Ultramicroscopy, 2005. **103**(1): p. 17-22.
93. Jani, J.M., et al., *A review of shape memory alloy research, applications and opportunities.* Materials & Design, 2014. **56**: p. 1078-1113.
94. Choudhary, N. and D. Kaur, *Shape memory alloy thin films and heterostructures for MEMS applications: a review.* Sensors and Actuators A: Physical, 2016. **242**: p. 162-181.
95. Otsuka, K. and X. Ren, *Physical metallurgy of Ti–Ni-based shape memory alloys.*

Progress in materials science, 2005. **50**(5): p. 511-678.

96. Hodgson, D.E., W. Ming, and R.J. Biermann, *Shape memory alloys.* ASM International, Metals Handbook, Tenth Edition., 1990. **2**: p. 897-902.
97. Clark, B.G., et al., *Size independent shape memory behavior of nickel–titanium.* Advanced Engineering Materials, 2010. **12**(8): p. 808-815.
98. Case, L., et al., *Shape Memory Alloy Shape Training Tutorial.* University of Michigan, 2004.
99. Ma, J., I. Karaman, and R.D. Noebe, *High temperature shape memory alloys.* International Materials Reviews, 2010. **55**(5): p. 257-315.
100. Xiaojun, Y., et al., *A one-stage, high-load capacity separation actuator using anti-friction rollers and redundant shape memory alloy wires.* Review of Scientific Instruments, 2015. **86**(12): p. 125005.

국문 초록

국소영역 집속이온빔 화학기상증착을 이용한 나노구조물 제작

이 강 인

서울대학교 공과대학원

기계항공공학부 기계공학전공

집속이온빔 화학기상증착(FIB-CVD) 공정은 1980 년대에 최초로 개발된 이래 반도체 공정 분야에서 주로 사용하였으나, 근래에는 마이크로/나노 스케일의 전자 소자, 센서/구동기 제작 및 나노물질, 바이오, 광학 분야의 응용에까지 폭넓게 활용되고 있다. 공정의 활용성이 확대됨에 따라, 정밀도, 효율, 적층물의 순도 등 공정의 성능을 개선하기 위한 기초 연구가 활발하게 진행되고 있다. 그러나 이러한 연구에도 불구하고 진공 환경, 이온 조건, 전구체 (precursor material) 및 시편 재료의 특성과 같은 파라미터의 연관성, 그리고 이온, 전자, 전구체 가스, 그리고 고체 기판의 표면과 상호 작용하는 적층 메커니즘의 복잡성 때문에 아직까지도 공정 메커니즘은 명확하게 규명되지 못하고 있다.

FIB-CVD 공정은 전구체 기체의 화학 반응에 의해서 전구체 화합물의 일부 구성 요소가 기판의 표면에 적층되는 공정이다. 일반적으로 온도 조건은 화학 반응 율을 결정하는 중요한 요인이 되기 때문에 온도는 이 공정에서 중요한 공정 변수가 된다. 온도가 공정에 미치는 영향을 분석한 이전의 연구 결과들을 보면, 전구체 보관 용기의 온도, 기판 표면 온도에 따른 적층 특성에 관한 연구들이 보고되었다. 그러나 전구체 가스의 온도는 화학반응에 직접적인 연관성이 있음에도 불구하고 이에 관해서는 아직까지 명확한 연구결과를 찾는 것은 대단히 어렵다. 이것은 전구체 기체를 공급하는 공급기에서 유량을 고정시킨 채 온도만을 변수로 하는 실험 구성을 하기 어려운 점에 주로 기인한다.

본 연구에서는 집속이온빔 화학기상증착 공정에서 전구체 기체의 온도가 공정 특성에 미치는 영향도를 적층률의 관점에서 분석하였다. 실험적 접근을 위해서 전구체 가스의 온도만을 개별 제어할 수 있도록 가스 공급 장치를 개발하였다. 개발된 가스 공급장치를 활용하여 $C_{14}H_{10}$ 전구체 가스의 온도를 변화시키면서 적층률에 미치는 영향도를 분석하였다. 또한, 실험 결과를 이론적으로 해석하기 위해서 적층 메커니즘에 관한 수치해석 기반의 공정 모델을 개발하였다. 시뮬레이션에서는 기존의 수치해석 연구에서는 고려하기 어려웠던 실시간 증가하는 적층면과 전자간의 거리계산의 복잡성을 해결하기 위해서 처음으로 영상처리에서 물체인식에 활용되는 하우스도르프 거리(Hausdorff distance) 개념을 적용하여 적층 메커니즘을 충실하게

반영할 수 있도록 하였다. 마지막으로, 공정에 관한 기초 연구를 근거로 수평방향 적층률을 강화시킨 집속이온빔 화학기상증착 공정을 활용하여 형상기억합금-탄소블록 복합재 마이크로구동기를 제작하였다. 또한, 형상기억합금과 복합재의 기계적 물성 차이에 기인한 구동 특성을 분석하기 위하여 마이크로 인장 시험을 실시하였다.

주요어 : 집속이온빔, 전구체 온도, 마이크로 구동기, 형상기억 합금, 화학 기상증착, 하우스도르프 거리 (Hausdorff distance)

학 번 : 2014-31040